SILVER-SODIUM ION-EXCHANGED WAVEGUIDES AND DEVICES: A TREATISE

By

HSING CHIEN CHENG

A DISSERTATION PRESENTED TO THE GRADUATE SCHOOL
OF THE UNIVERSITY OF FLORIDA IN PARTIAL FULFILLMENT
OF THE REQUIREMENTS FOR THE DEGREE OF
DOCTOR OF PHILOSOPHY

UNIVERSITY OF FLORIDA

1991

ACKNOWLEDGEMENTS

I would like to express my deep gratitude to my advisor Dr. Ramu V. Ramaswamy for his constant encouragement and guidance throughout my study and for providing an atmosphere conducive for research and a well-equipped Photonics Research Laboratory. His dedication to the integrated optics field, hard work and professional attitude really inspired me and helped me towards the successful completion of this research work. In addition, through his academic leadership, I greatly enhanced the knowledge required in the integrated optics field.

Invaluable suggestions and critical discussions were frequently provided by Dr. Ramakant Srivastava who also helped me with the experimental procedures and the optical characterization setups in the laboratory. I sincerely thank him for promptly providing me all the assistance as often as it was needed.

Appreciations are also extended to my fellow graduate students: particularly Dr. Song Jae Lee, Dr. Young Soon Kim, Dr. Sang Sun Lee, Chris Hussell, Amalia Miliou, Hyoun S. Kim, Sang K. Han, Jamal Natour, Tim Horton, Ron Slocumb, and Kirk Lewis, and fellow researchers: Huo Zhenguang and Dr. Simon Xiaofan Cao, for creative presentations and informative discussions in our weekly group meetings. Many members of this department have provided assistance; without their efforts, it would have been difficult to accomplish my

goals; I thank each of them: Allan Herlinger for machining sample holders used in the diffusion process and components used in the optical measurement setup, Mike Lewis for providing necessary information on the Harris computer H800, James Chamblee and Jim Hales for maintaining the E-beam evaporation system and providing assistance on various processing procedures as well as operation of the equipment in the Microelectronics Laboratory.

I am grateful to my fellow members of the Gainesville Chinese Christian Fellowship for their faithful prayers. Last but not least, I want to extend my special thanks and appreciation to the three most important persons in my life: my wife May, my father and my mother for their endless love and constant support.

TABLE OF CONTENTS

Page

ACKNOWLEDGEMENTS ii

ABSTRACT vii

CHAPTERS

1. INTRODUCTION 1

2. ION-EXCHANGE IN GLASS 13

2.1. Introduction 13
2.2. Kinetics of Ion Exchange 14
2.2.1. Basic Equations for Binary Exchange 14
2.2.2. Diffusion Equation: Small Space-Charge Density Approximation 19
2.2.3. Diffusion without Applied Field 22
2.2.4. Field Assisted Diffusion 28
2.3. Silver-Sodium Ion Exchange 33
2.3.1. The Equilibrium Condition and the Index Change 35
2.3.2. Space Charge Effect and Multi-Alkali Effect 38
Space Charge Effect 38
Multi-Alkali Effect 39
2.3.3. Temperature Dependence of the Self-Diffusion Coefficient 40
2.4. Summary 41

3. NUMERICAL MODELING OF PLANAR AND CHANNEL WAVEGUIDES 42

3.1. Introduction 42
3.2. Graded-Index Profile 45
3.2.1. Green's Function: One Dimensional Case 45
Impluse Response 45
Surface Waveguides with Inifite Source—One-Step Process 48
Buried Waveguides—Two-Step Process 50
3.2.2. Green's Function: 2 and 3 Dimensional Cases 52
3.2.3. Finite Difference Method (FDM) 53
1-D Linear Diffusion Equation, without Field 54

1-D Linear Diffusion Equation, with Field 57
2-D Linear Diffusion Equation 58
1-D and 2-D Nonlinear Diffusion Equation 59
3.3. Guided Wave—Helmholtz Equation 64
3.3.1. Vector and Scalar Helmholtz Equation 65
3.3.2. One-Dimensional Waveguides 67
WKB Method 68
Matrix Method 71
Finite Difference Method 77
3.3.2. Two-Dimensional Numerical Method 80
Effective Index Method 81
Finite Difference Method 84
3.4. Propagating Wave—Beam Propagation Method 86
3.4.1. BPM Formulation 87
3.4.2. Numerical Implementation 92
3.4.3. Simulation of Cross Coupler by BPM 93
3.5. Summary of Numerical Methods 95

4. FABRICATION AND CHARACTERIZATION 98

4.1. Fabrication 98
4.1.1. One-Dimensional Waveguides 99
Melt Preparation 100
Sample Preparation 101
Prebaking and Diffusion 101
Waveguide Cleaning and Polishing 104
4.1.2. Two-Dimensional Waveguides 108
Choice and Evaporation of the Mask Material 108
Photolithography 111
Etching 114
Prebaking, Diffusion and Polishing 115
Removal of Mask 115
4.2. Characterization 116
4.2.1. Mode Index of Planar Waveguides 116
Prism Coupler 117
Experiment and Measurement 120
Inverse WKB method 124
4.2.2. Experimental Procedure to Determine the Diffusion Coefficient 128
4.2.3. 2-D Mode Field and Loss Measurement 133
4.3. Summary 140

5. MODELING OF TAPERED WAVEGUIDES 141

5.1. Introduction 141
5.2. Modeling 144
5.2.1. Planar Waveguides 144
5.2.2. Channel Waveguides 148
5.2.3. Tapered Waveguides 150
5.2.4. Results and Comparison with Experiment 151

5.3. Simulation of Propagation 163
5.3.1. Beam Propagation Analysis 163
5.3.2. Simulation Results 167
5.4. Summary 172

6. DIRECTIONAL COUPLERS AS WAVELENGTH MULTIPLEXERS/DEMULTIPLEXERS 174

6.1. Introduction 174
6.2. Coupled-Mode Theory 175
6.2.1. Coupled-Mode Theory 176
6.2.2. Relation between Normal-Modes and Coupled-Modes 179
6.3. Modeling 185
6.3.1. Index Profile 185
6.3.2. Numerical Method 187
6.3.3. Directional Coupler 188
6.3.4. Design of Dual-Wavelength Demultiplexers 190
6.3.5. Numerical Results 196
6.4. Fabrication 203
6.5. Characterization 207
6.5.1. Measurement of Spectral Response 207
6.5.2. Determination of the Coupling Length 210
6.6. Experimental Results and Comparison with Modeling 215
6.7. Summary 223

7. CONCLUSIONS AND FUTURE WORK 227

7.1. Conclusions 227
7.2. Advanced Study on Ion Exchange 229
7.2.1. Other Cation Pairs 229
7.2.2. Space Charge, Local Field, and Side Diffusion 231
7.2.3. 2-D Buried Waveguides 232
7.3. Functional Devices and Integrated System 232
7.3.1. Waveguide Bends 232
7.3.2. Asymmetric Y-Branch 233
7.3.3. Asymmetric Directional Coupler 236
7.3.4. Glass Waveguide Laser and Integrated System 237

REFERENCES 238

BIOGRAPHICAL SKETCH 257

Abstract of Dissertation Presented to the Graduate School
of the University of Florida in Partial Fulfillment of the
Requirements for the Degree of Doctor of Philosophy

SILVER-SODIUM ION-EXCHANGED WAVEGUIDES AND DEVICES: A TREATISE

By

Hsing Chien Cheng

May, 1991

Chairman: Ramu V. Ramaswamy
Cochairman: Ramakant Srivastava
Major Department: Electrical Engineering

A general, systematic, theoretical and experimental study of the ion-exchange process (IEP) in glass is presented. The study encompasses characterization of the graded-index (GRIN) waveguides fabricated using the Ag^+-Na^+ IEP, as well as the application of these waveguides to practical devices such as tapered waveguide transitions and multiplexers / demultiplexers (MUX / DEMUX) using symmetric directional couplers. The IEP as well as GRIN waveguides and the devices have been modeled and excellent agreement has been obtained with the experimental results.

The modeling starts with the simulation of the IEP in glass. The 1-D and 2-D nonlinear diffusion equations are solved by a finite difference method (FDM) to obtain the index profile for both the single-step and two-step diffusion processes with and without an external electrical field. The modal characteristics of the waveguides

are attained by solving the Helmholtz equation by FDM. The beam propagation method (BPM), used to simulate the wave propagation in devices, is also illustrated.

The fabrication and characterization of low-loss, single-mode planar and channel waveguides are described in detail. The waveguides are obtained by exchanging Na^+ in the BK7 glass substrate with Ag^+ in a molten salt bath consisting of $NaNO_3$, KNO_3 and $AgNO_3$. The resulting guides are characterized in terms of the mode indices, modal fields and attenuations at 1.3 μm wavelength.

The results are correlated with the theory and are further used to predict the index profile and the modal field distribution of tapered waveguides obtained by postbaking surface channel waveguides under a thermal gradient. The radiation losses in tapered transitions with various taper profiles and lengths are simulated by BPM. Lossless transitions are attained for 5 mm long tapers.

Symmetric directional couplers as wavelength MUX/DEMUX are modeled, fabricated, and tested. The coupling length of the couplers as a function of wavelength is determined by a novel technique employing the spectral response of the normalized, measured power outputs of the two guides. MUX/DEMUX operating at 1.315 and 1.561 μm with crosstalk and cross power ratio of at least -40 dB are demonstrated. A total insertion loss of 1.25 dB for a 14.5 mm long device and propagation loss as low as 0.15 dB/cm have been achieved.

CHAPTER 1
INTRODUCTION

A new era of optical communication systems was started in 1970s by the achievement of low propagation loss in optical fibers. Optical communication has grown from its infant stage in the early 70s into one of the major industries today, thanks to a parallel development in the associated technologies such as reliable semiconductor lasers, high speed modulators, high efficiency detectors and monolithic integration of the above devices. As the systems become more and more sophisticated, the criteria for cost, fiber compatibility and performance are becoming more important. Therefore, extensive research and development efforts in this field have continued to meet the stiff requirement. The future of the optical communication indeed is extremely bright.

Optical communication system consists of active components, *e.g.*, laser, modulator, *etc.* as well as passive components, *e.g.*, filter, power divider, *etc.* To realize these passive devices and satisfy the criteria mentioned above, glass waveguides fabricated by ion exchange technique have recently received considerable attention. This well-known ion-exchange technique was used in early days to strengthen the glasses and produce tinted glasses. It has been used to change the refractive index, color, strength [Ohta75, Fine88, see ref. list in Kara79] *etc.* in glass. Ion-exchanged glass waveguides and integrated optical devices on glass substrates are one of the best choices since 1)

optical-quality substrate material is generally inexpensive compared to its competing crystal substrates such as $LiNbO_3$ or III-V compound semiconductors; 2) fabrication is quite simple and can be carried out at a relatively low temperature and, thus, the cost is reduced; 3) refractive index of host glass is compatible to that of the optical fibers and the reflection loss at the fiber-device interface is minimal; and 4) high-performance devices with low propagation loss are easily attainable.

Optical waveguides, in most of the applications in communication systems, are two-dimensional (2-D) structures that are characterized by a region of higher index in the transverse dimensions, capable of confining the light energy within this region while guiding it along the longitudinal direction. In the case of waveguide fabrication in glass by ion exchange, the refractive index is increased by exchanging the monovalent network modifiers in the glass *e.g.*, Na^+ in soda-lime or BK7 glass, with larger polarizability cations in the molten salt, *e.g.*, K^+, Ag^+ or Tl^+. The compositions of a typical soda-lime [Rama88d] and BK7 glasses [Gort86b] in weight percentages are given in Table 1. The densities of the soda-lime and BK7 glasses are 2.50 g/cm^3 and 2.51 g/cm^3, respectively.

Several monovalent cation pairs are available for the exchange *e.g.*, Ag^+-Na^+, K^+-Na^+, Cs^+-K^+ and Tl^+-K^+ *etc.* Among these pairs, Ag^+-Na^+ and Tl^+-K^+ are attractive since they yield large index changes (~0.1) [Find85, Rama88b]. The index change can be lowered by diluting the melt with the exchanged ions. Thus, with the above two cation pairs, the maximum index change in the waveguide is adjustable in a wider range. However, it is well known that thallium ions are toxic

Table 1

Glass composition in weight percentages

Oxide	Soda-lime	BK7
SiO_2	72.25	69.6
Na_2O	14.31	8.4
K_2O	1.20	8.4
CaO	6.40	-
MgO	4.30	-
B_2O_3	-	9.9
BaO	-	2.5
Al_2O_3	1.20	-
SO_3	0.30	-
Fe_2O_3	0.03	-
Others	-	1.2

and, therefore, great care must be exercised in the fabrication. Silver ions are easily reduced into metallic form in glass via reaction with the additives in the glass refining process, resulting in higher losses. Nevertheless, the problem of silver-ion reduction is eliminated when high-quality optical glasses and/or lower silver concentration (smaller index change) are used.

The first reported low-loss ion-exchanged glass waveguides were fabricated by Izawa and Nakagome [Izaw72] using thallium ions in a borosilicate glass under applied field. They also reported the first buried planar waveguides (maximum index change occurring not at the glass surface but below the surface) fabricated by using a two-step process. The channel waveguides were realized in 70s by ion-exchange technique [Gede75b, Gall76, Wils76]. To date, several passive components *e.g.*, power dividers or couplers [Cull84, Yip84, Maha88b], multiplexers [Walk83b, Mcco87], filters [Walk83a, Hond84, Conn87, Naja88a], polarizers [Find83], and sensors [Honk87a], have been reported using ion-exchanged glass waveguides. Furthermore, ion-exchanged waveguides have been fabricated in the nonlinear semiconductor-doped glasses [Cull86], which increases the possibility of integrating optical switching devices in glass. Recently, thermo-optic phase modulator has been demonstrated in ion exchanged glass waveguides [Jest90] and rare-earth doped glass waveguide lasers [Sanf90, Aoki90] and SiGe:H photodetectors on glass waveguides [Deim90] have been demonstrated using the ion-exchange technique. In addition, feasibility of "transplanting" III-V opto-electronic devices on glass substrates [Yabl86] and incorporation of highly nonlinear polymer films on glass waveguides [Schl90] suggests that opportunities

to integrate active devices with passive components on glass substrates may soon become a reality.

In this dissertation, a general, systematic, theoretical and experimental study of the ion-exchange process in glass is presented. The study encompasses characterization of the graded-index waveguides fabricated using the Ag^+-Na^+ ion-exchange process, as well as the application of these waveguides to practical devices such as tapered waveguide transitions and multiplexers/demultiplexers (MUX/DEMUX) using symmetric directional couplers. The ion-exchange process as well as graded-index waveguides and the devices have been modeled and excellent agreement has been obtained with the experimental results.

In chapter 2, the binary ion exchange and cation diffusion in glass are discussed along with the ion-exchange equilibrium, space-charge effect, multialkali effect and temperature dependence of the ion exchange process. The nonlinear diffusion equation for the incoming cations is derived from the Fick's law with the approximation of small space-charge density. It is shown that the equation can be linearized if the concentration of the incoming ions is low or the mobilities of the two species of exchanging ions are equal. Under these conditions, analytical solutions are available for one-dimensional (1-D) cases if the diffusion coefficient and mobility are constant. However, in general, a closed-form solution is not available.

Since the closed form solution of the nonlinear diffusion equation is not always attainable, chapter 3 deals with several numerical methods to solve the equation and predict the resulting waveguide propagation characteristics. Numerical solutions give very

accurate results since high speed computers for numerical intensive calculations and library programs for solving difficult problems are readily available, evoking the numerical analysis to play a major role in the modeling of the complicated, practical cases. Three numerical techniques including Green's function approach, implicit finite difference method (FDM) and explicit FDM will be presented for solving the diffusion equation. The concentration profile is assumed to be proportional to the profile of the index change. Next, the index profile is used in the scalar Helmholtz equation to solve for the mode-field profiles as well as the corresponding propagation constants. The WKB method, the matrix method and FDM for the 1-D cases are introduced along with the effective index method and FDM for the 2-D case. The beam propagation method (BPM) is also discussed in this chapter. The propagation of the wave in various waveguide structures, with index varying in the longitudinal direction, can be solved by this method.

In chapter 4, 1-D (planar) and 2-D (channel) waveguide fabrication technique is described in detail. In the fabrication process for practical applications, single-mode waveguide, supporting only one mode, is emphasized since most applications entail this requirement. One-dimensional multimode waveguides are fabricated only for the purpose of determining diffusion characteristics. The fabrication procedure for 1-D waveguides includes melt preparation, sample preparation, prebaking, diffusion, cleaning and polishing. Similar procedures are applied to fabricate 2-D waveguides except that extra steps, namely, mask preparation, photolithography, etching, *etc.*, are needed before prebaking in the 2-D case. Procedures to measure the

mode indices of planar waveguides and the mode field of channel waveguides are also illustrated in chapter 4. The index profiles are reconstructed from the measured mode indices by the inverse WKB method where from the diffusion coefficient is determined. The knowledge of the diffusion coefficient and the corresponding diffusion parameters is very helpful in the modeling of the waveguide devices. The mode fields and losses of the channel waveguides are measured by the near-field measurement setup, also described in this chapter.

A systematic modeling of the tapered waveguides is presented in chapter 5. As shown in Fig. 1-1, a tapered waveguide has small dimension at one end and large dimension at the other end so that it may provide a smooth transition between two devices with different sizes. Smooth transitions usually have lower radiation loss than abrupt junction since the index profiles are continuous in the propagation direction. As the density of devices on the same substrate becomes higher, the device dimension becomes smaller. In connecting small-size devices with fiber, tapers can also help reduce the mismatched loss at the interface. Thus, the realization and analysis of the tapered waveguides are important steps before high-density integrated optics come true. Taper modeling requires simulation of 1-D and 2-D waveguides. One-dimensional simulation provides the necessary information, such as the diffusion coefficient as a function of temperature, for the successive modeling of the 2-D waveguides and tapers. Since the tapered guides are fabricated by a two-step process, the simulation is divided into two steps. The first step is the simulation of straight channel waveguides, *i.e.*, solving the 2-D

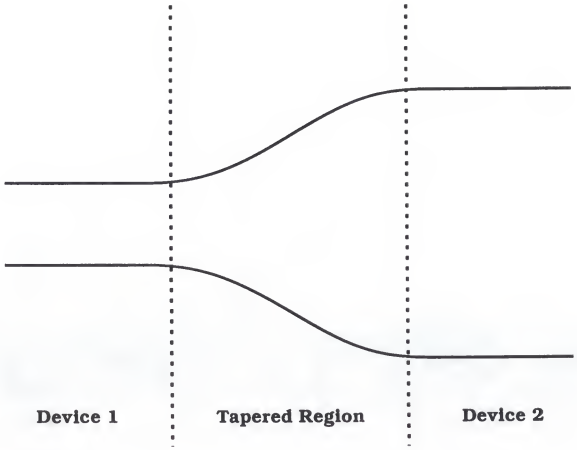

Fig. 1-1. Schematic of a tapered waveguide used as an optical interconnect between two devices.

diffusion and Helmholtz equations with index profile invariant in the propagation direction. The resulting index profile from the first step is fed into the second step simulation. The tapers are fabricated with a thermal gradient and, therefore, the temperature-dependent diffusion coefficient is considered in the second step simulation. Furthermore, the radiation loss of tapered waveguides with different taper profiles is simulated by BPM.

Chapter 6 consists of the modeling, fabrication, and characterization of the directional couplers as wavelength MUX/DEMUX. Wavelength MUX/DEMUX are necessary devices to utilize the advantage of the high bandwidth of optical fibers. Figures 1-2 (a) and (b) illustrate two signals combined by a MUX and splitting by a DEMUX, respectively. Note that DEMUX plays a function reverse to that of MUX. They are fundamental building blocks toward high-capacity optical communication system. Wavelength MUX/DEMUX can be realized by a symmetric directional coupler constructed by two identical waveguides, as shown in Figs. 1-3 (a) and (b). The design considerations of MUX/DEMUX, based on spectral bandwidth, crosstalk and cross power ratio and their dependence on the fabrication errors, are presented in this chapter. The characterization setup for measuring the spectral response is discussed and the experimental results are used to estimate the coupling length as a function of wavelength and the results are compared to the predictions of the modeling.

The last chapter (chapter 7) concludes by summarizing the results, while illustrating other applications of the modeling. It

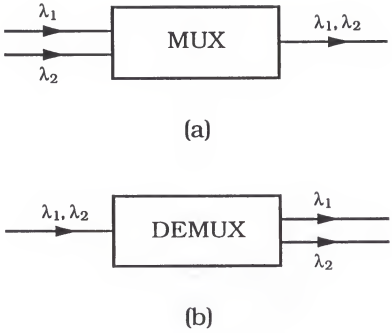

Fig. 1-2. Block diagram of the dual-wavelength MUX/DEMUX. (a) Two input signals of wavelengths λ_1 and λ_2 are combined at the output. (b) Mixed wavelengths λ_1 and λ_2 are split at the output.

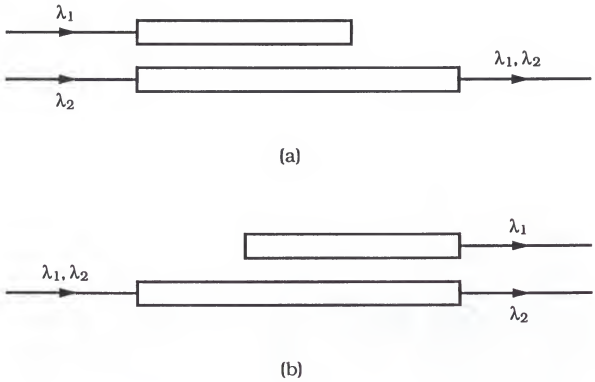

Fig. 1-3. Symmetric direction coupler as a wavelength MUX/DEMUX. (a) The energy of the signal λ_1 transfers to the other channel and mixed with the signal λ_2 at the output. (b) Mixed signals λ_1 and λ_2 are separated at the output.

also describes the future research work utilizing the well-developed ion-exchange technique to fabricate other practical devices useful in optical communication systems.

CHAPTER 2
ION-EXCHANGE IN GLASS

2.1. Introduction

The study of the ion-exchange process is important since the concentration profile of the diffused ions in the ion-exchange process determines the index-change profile in the glass and therefore, the characteristics of the waveguide. As a result, a knowledge of the theory of ion exchange as well as the quantitative analysis of the profile of the exchanged ions is essential for successful design and development of passive integrated optical components.

Extensive research on ion exchanged waveguides and devices has been performed over the past two decades and several excellent review papers [Dore69, Kara79, Find85, Rama88b, Rama88c, Ross89] are readily available. This chapter presents the theory of ion-exchange kinetics and its application to the silver-sodium cation system. Portions of this chapter have been extracted from previously published results [Dore64, Rama88b]. The governing equation in the ion exchange namely, the nonlinear diffusion equation, is derived from first principles using the diffusion of the ionic flux according to the Nernst-Planck equation. The inter-diffusion coefficient resulting in the equilibrium condition of the diffusing ions — one ion in, one ion out — will also be discussed in this chapter. Moreover, several cases will be considered so that analytical results for the concentration profile of

the specific diffusing ion can be obtained. The numerical methods to solve the diffusion equation and the associated results will be described in the next chapter.

2.2. Kinetics of Ion Exchange

2.2.1. Basic Equations for Binary Exchange

The basic theory of ion exchange has been discussed and solved numerically by Helfferich et al. [Helf58, Ples58, Helf62] in spherical coordinates; it has been applied to glasses and compared with the experimental results by Doremus [Dore64]. In this chapter, only two ions (species A and B) are considered in the formulation. We assume that the fluxes of exchanging ions A and B are coupled solely by the electrochemical potential and no chemical reaction and/or bonding is assumed during ion exchange. The ionic fluxes of A and B in glass are given [Helf58] by the Nernst-Planck equation:

$$\vec{\phi_i} = \mu_i z_i C_i \vec{\mathcal{E}} - D_i \nabla C_i \frac{\partial \ln a_i}{\partial \ln C_i}, \qquad (2.1)$$

where i represents ion A or ion B, $\vec{\phi_i}$ is the ionic flux $\{m^{-2}sec^{-1}\}$, μ_i is the mobility $\{m^2V^{-1}sec^{-1}\}$, z_i is the electrochemical valence, C_i is the concentration $\{m^{-3}\}$ of either exchanging ion in glass, $\vec{\mathcal{E}}$ is the local electric field {V/m} consisting of the space-charge induced field $\vec{\mathcal{E}_s}$ and the applied field $\vec{\mathcal{E}_a}$, D_i is the self-diffusion coefficient $\{m^2sec^{-1}\}$, and a_i is the thermodynamic activity. The units are shown in the brackets. The first term represents the ions driven under the electric potential difference or the drift term, while the second term is the

diffusion term and represents the ions diffused under the chemical potential difference resulting from the concentration gradient.

In the above equation, we have neglected the deformation or the strain induced by the swelling or shrinkage of the glass network due to the exchange with larger or smaller ions in the melt [Sane78, Bran86]. If the deformation is considered, one more term proportional to $\vec{v_D}$ representing the velocity of the ions moving under the strain must be added. $\vec{v_D}$ is proportional to the time derivative of $r_A^3 C_A + r_B^3 (C_B - C_0)$ in the direction normal to the glass surface, where the r_i is the radius of the ion i and C_0 is the concentration of the ion B before ion exchange. In the case of K^+-Na^+ exchange system, this term cannot be omitted since the swelling produced by the larger potassium ions is significant [Tsut86]. Researchers often include the strain effects in the diffusion term by defining a polarization-dependent and/or anisotropic self-diffusion coefficient as is the case with potassium exchanged glass waveguides [Yip85]. This approach is unrealistic since the strain induced term is not proportional to the gradient of the ionic concentration. However, the index change is polarization-dependent due to the anisotropic stress [Tsut88].

The activity can be written as $a_i = C_i^m$ where m is a constant representative of the ions in silicate glasses [Lait57, Karr62][1]. Thus, $\partial \ln a_i / \partial \ln C_i = m$ and Eq. (2.1) becomes

$$\vec{\phi_i} = \mu_i C_i \vec{\mathcal{E}} - m D_i \nabla C_i . \qquad (2.2)$$

[1] m is denoted as n in the references.

Only monovalent ions are considered in Eq. (2.1) *i.e.*, z_i=1. Note that the flux $\vec{\phi}_i$ in Eq. (2.2) is a function of time and position, so are C_i and $\vec{\varepsilon}$. D_i and μ_i are temperature-dependent [Dore64] and are assumed not to be functions of concentration C_i and therefore position and time during the diffusion; however, this oversimplification is not justifiable in the case of strong multi-alkali effect [Isar69, Day76, Char82b] which will be addressed in section 2.3.2.

The total charge in the system must remain constant (Fig. 2-1). The relation between the incoming ion concentration C_A and the out-diffusing ion concentration C_B in glass is obtained as follows:

$$C_A + C_B + C_S = C_0 \,, \tag{2.3}$$

where C_0 equals the concentration of the ion B in glass before diffusion; in other words, prior to diffusion, as shown in Fig. 2-1(a), $C_0 = C_{B0}$, the value of C_B at time t=0. C_S is the concentration of the net depleted mobile ions at a given time giving rise to space charge. From Fig. 2-1(b), it follows that $C_S = C_0 - C_A - C_B$. C_S is zero only when the exchange is strictly one-to-one at all times. It exists whenever two dissimilar species of unequal mobilities are involved in the exchange. For example, when Na^+ in glass and Ag^+ in the melt exchange with each other, Na^+ ions diffuse out of the glass at a faster rate which causes negative space charge to build up. This induces a local field which slows down the depletion of Na^+ and accelerates the in-diffusion of Ag^+ until such time the equilibrium condition is reached and one-to-one exchange takes place. Besides, the application of an external field could also be responsible for the creation of space

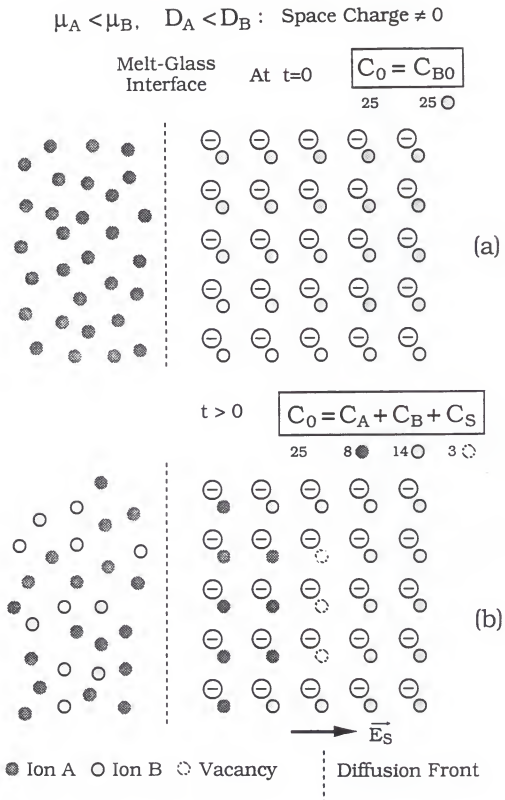

Fig. 2-1. Correlation of the ionic concentrations in ion exchange process for $\mu_A < \mu_B$ and $D_A < D_B$. (a) At t=0, $C_0 = C_{B0}$; (b) At t>0, $C_0 = C_A + C_B + C_S$. The numbers listed illustrate the relation of the ionic concentration to the space-charge density.

charge, especially when the mobilities of the exchanging ions are unequal. The space charge is related to the electric field by Poisson's equation namely,

$$\nabla \cdot (\varepsilon_r \vec{\mathcal{E}}) = \frac{- q C_S}{\varepsilon_o} , \qquad (2.4)$$

where ε_r is the low frequency relative permitivity (dielectric constant) of the isotropic substrate, q is the monovalent cation charge (equal, in magnitude, to the electronic charge) and ε_o is the permitivity in vacuum. ε_r in Eq. (2.4) does not represent the dielectric constant at optical frequencies, which determines the refractive index of medium and depends on the glass composition. The negative sign on the right hand side of Eq. (2.4) indicates that the total charge is negative in the region depleted of positive ions; in this case $C_S > 0$. When the ions diffuse into the glass, the composition of glass as well as its dielectric constant changes. Therefore, ε_r is a function of C_A and can be empirically expressed as [Volf88]

$$\varepsilon_r = g C_A + \varepsilon_{ro} , \qquad (2.5)$$

where g is an empirical coefficient assuming $gC_A << \varepsilon_{ro}$ and ε_{ro} is the dielectric constant before diffusion.

Since the numbers of ion A and ion B are conserved, the continuity equation

$$\nabla \cdot \vec{\phi_i} = - \frac{\partial C_i}{\partial t} , \qquad (2.6)$$

is applicable. Equations (2.2)-(2.6) are the fundamental equations governing the ion exchange process between two monovalent ions in glass:

$$\vec{\phi_i} = \mu_i C_i \vec{\mathcal{E}} - m D_i \nabla C_i$$

$$\nabla \cdot \vec{\phi_i} = - \frac{\partial C_i}{\partial t}$$

$$\nabla \cdot (\varepsilon_r \vec{\mathcal{E}}) = \frac{- q C_S}{\varepsilon_o}$$

$$\varepsilon_r = g C_A + \varepsilon_{ro}$$

$$C_A + C_B + C_S = C_0$$

i=A or B

Although the unknowns C_A, C_B, and C_S are functions of position and time, we are interested in finding the solution for C_A. There are no simple analytical solutions for the Eqs. (2.2)-(2.6). However, with some assumptions, these equations can be rewritten and combined into one differential equation with only one unknown, C_A, which is assumed to be proportional to the refractive index change in the glass.

2.2.2. Diffusion Equation: Small Space-Charge Density Approximation

Since only network modifiers in glass are involved in the exchange, the total concentration C_0 of the mobile ions is a constant. By substituting Eq. (2.3) into Eq. (2.6), we obtain

$$\nabla \cdot (\vec{\phi_A} + \vec{\phi_B}) = - \frac{\partial}{\partial t}(C_A+C_B) = - \frac{\partial}{\partial t}(C_0-C_S) = \frac{\partial C_S}{\partial t} . \qquad (2.7)$$

The above equation describes the continuity of the space charge. In the case of one-to-one exchange, the space charge density

corresponding to the local induced field is usually eight orders of magnitude smaller than the mobile charge density [Walk83c]; C_S can be assumed to be quite small compared to C_A and C_B, so that

$$\nabla \cdot (\vec{\phi_A} + \vec{\phi_B}) \equiv 0 . \tag{2.8}$$

Substituting Eq. (2.2) into Eq. (2.8) and assuming constant self-diffusion coefficients and mobilities, after some algebraic manipulations, the divergence of the field $\vec{\mathcal{E}}$ is expressed as

$$\nabla \cdot \vec{\mathcal{E}} = \frac{m (D_A \nabla^2 C_A + D_B \nabla^2 C_B) - \vec{\mathcal{E}} \cdot (\mu_A \nabla C_A + \mu_B \nabla C_B)}{\mu_A C_A + \mu_B C_B} . \tag{2.9}$$

Since the change in the dielectric constant is negligible, we can conclude by comparing Eqs. (2.4) and (2.9) that $\nabla \cdot \vec{\mathcal{E}}$ is nonzero with the result that the space charge C_S is non-zero. The rate of change of the concentration of ion A can be derived from Eq. (2.6) by substituting into Eqs. (2.2) and (2.9):

$$\begin{aligned} \frac{\partial C_A}{\partial t} &= m D_A \nabla^2 C_A - \mu_A \vec{\mathcal{E}} \cdot \nabla C_A - \mu_A C_A \nabla \cdot \vec{\mathcal{E}} \\ &= m D_A \nabla^2 C_A \frac{(D_B/D_A)\mu_A C_A + \mu_B C_B}{\mu_A C_A + \mu_B C_B} \\ &\quad - \mu_A \vec{\mathcal{E}} \cdot \nabla C_A \frac{\mu_B (C_A + C_B)}{\mu_A C_A + \mu_B C_B} . \end{aligned} \tag{2.10}$$

The normalized concentrations (or the mole fractions) N_A and N_B are defined as $C_A/(C_A+C_B)$ and $C_B/(C_A+C_B)$, respectively. Equation (2.10) can then be rewritten in terms of the inter-diffusion and inter-mobility coefficients as

$$\frac{\partial C_A}{\partial t} = mD_A\nabla^2 C_A \frac{(D_B/D_A)\mu_A N_A + \mu_B N_B}{\mu_A N_A + \mu_B N_B}$$
$$- \vec{\mathcal{E}}\cdot\nabla C_A \frac{\mu_A\mu_B}{\mu_A N_A + \mu_B N_B}$$
$$= \tilde{D}\,\nabla^2 C_A - \tilde{\mu}\,\vec{\mathcal{E}}\cdot\nabla C_A\,, \qquad (2.11)$$

or
$$\frac{\partial N_A}{\partial t} = \tilde{D}\,\nabla^2 N_A - \tilde{\mu}\,\vec{\mathcal{E}}\cdot\nabla N_A\,, \qquad (2.12)$$

where $\tilde{D}$ is the inter-diffusion coefficient defined by Doremus [Dore64, Dore69].

$$\tilde{D} = mD_A \frac{(D_B/D_A)\,\mu_A N_A + \mu_B N_B}{\mu_A N_A + \mu_B N_B}. \qquad (2.13)$$

Similarly, we can also define inter-mobility coefficient $\tilde{\mu}$ as

$$\tilde{\mu} = \frac{\mu_A\ \mu_B}{\mu_A N_A + \mu_B N_B} = \frac{\mu_A}{1 - (1 - \frac{\mu_A}{\mu_B})N_A} = \frac{\mu_A}{1\ -\ \alpha N_A}. \qquad (2.14)$$

α equals $1-\mu_A/\mu_B$. By applying the Einstein relation $D_A = \frac{kT}{q}\mu_A$, where k is the Boltzmann constant and T is the absolute temperature, we see that $D_A/\mu_A = D_B/\mu_B$ [Dore64]. $\tilde{D}$, in this case, has the same form as $\tilde{\mu}$, except for the factor m. Equation (2.13) then becomes

$$\tilde{D} = \frac{mD_AD_B}{D_AN_A + D_BN_B} = \frac{mD_A}{1 - (1 - \frac{\mu_A}{\mu_B})N_A} = \frac{mD_A}{1\ -\ \alpha N_A}. \qquad (2.15)$$

However, it is well known that the Einstein relation often does not hold in glasses due to several mechanisms [Beie85] and therefore, requires modification. The modified Einstein relation $D_A = f\,\frac{kT}{q}\mu_A$ includes a correction factor f which is usually less than one [Dore64,

Dore69, Rama88b]. Inspection of Eq. (2.15) reveals that $\tilde{D}$ and $\tilde{\mu}$ are concentration dependent for $\alpha N_A \neq 0$. Hence, Eq. (2.12) is a nonlinear diffusion equation and no closed form solution for N_A is possible. However, explicit analytical solutions can be obtained under certain conditions which are described below.

2.2.3. Diffusion without Applied Field

Under equilibrium, the sum of the two ionic fluxes is assumed to be always zero, resulting in one-to-one exchange between the monovalent ions:

$$\vec{\phi}_A + \vec{\phi}_B = 0 . \tag{2.16}$$

Thus, in the case of zero external field ($\vec{\mathcal{E}}_a = 0$), the local field $\vec{\mathcal{E}}_s$ due to space charge is given by

$$\vec{\mathcal{E}}_s = \frac{D_A - D_B}{\mu_A N_A + \mu_B N_B} \nabla N_A = \left(\frac{D_A}{\mu_A}\right) \frac{-\alpha \nabla N_A}{1 - \alpha N_A} . \tag{2.17}$$

If α is zero, *i.e.*, in the case of equal-mobility diffusion, the field is zero. Note that the field increases as the gradient of N_A increases, indicating that the space-charge-induced field is stronger at the diffusion front. Equation (2.12) can be simplified by substituting the field $\vec{\mathcal{E}}_s$ in Eq. (2.17) as

$$\frac{\partial N_A}{\partial t} = \nabla \cdot (\tilde{D} \nabla N_A) . \tag{2.18}$$

Further simplifications of the 3-D nonlinear equation — Eq. (2.18) — is possible in the following cases.

a) $\mu_A=\mu_B$ *($\alpha=0$).* In this case, Eq. (2.18) becomes a linear equation:

$$\frac{\partial N_A}{\partial t} = \nabla \cdot (\widetilde{D}\, \nabla N_A) = m D_A \nabla^2 N_A . \qquad (2.19)$$

b) $N_A<<1$. The concentration of ion A in glass is very small so that the denominator of Eq. (2.15) equals one. In this case, the equation is the same as Eq. (2.19).

c) $D_A<<D_B$ *($\mu_A<<\mu_B$ or $\alpha\equiv 1$).* In this case, the inter-diffusion coefficient can be approximated as

$$\widetilde{D} \cong \frac{m\, D_A}{1 - N_A} .$$

Equation (2.18) becomes

$$\frac{\partial N_A}{\partial t} = \frac{m D_A}{1-N_A}\left[\nabla^2 N_A + \frac{1}{1-N_A}(\nabla N_A \cdot \nabla N_A)\right] . \qquad (2.20)$$

Equation (2.20) can be reduced to Eq. (2.19) in the special case $N_A<<1$ and $|\nabla N_A|^2<<\nabla^2 N_A$.

d) *Two-dimensional (2-D) case.* In the 2-D case, Eq. (2.18) can be reduced to

$$\frac{\partial N_A}{\partial t} = \frac{\partial}{\partial x}\left(\frac{m D_A}{1-\alpha N_A}\frac{\partial N_A}{\partial x}\right) + \frac{\partial}{\partial y}\left(\frac{m D_A}{1-\alpha N_A}\frac{\partial N_A}{\partial y}\right) . \qquad (2.21)$$

The 2-D modeling by the finite difference method was first presented by Wilkinson and Walker [Wilk78]. We will discuss the solution for the above case in the next chapter.

e) *One-dimensional (1-D) case.* The further reduction of Eq. (2.21) to one-dimension yields

$$\frac{\partial N_A}{\partial t} = \frac{\partial}{\partial x}\left(\frac{mD_A}{1-\alpha N_A}\frac{\partial N_A}{\partial x}\right). \qquad (2.22)$$

If $\alpha N_A << 1$, Eq. (2.22) becomes

$$\frac{\partial N_A}{\partial t} = mD_A \frac{\partial^2 N_A}{\partial x^2}. \qquad (2.23)$$

Thus, the above 1-D diffusion is valid in the case of ion exchange without applied field for 1) equal mobility ions *i.e.*, no space charge; 2) unequal mobilities but low concentration of diffusants, *i.e.*, small space charge effect.

Analytical solutions are available for Eq. (2.23) in the following two cases of ion exchange in glass provided D_A is both position and time independent. As described earlier, this is valid as long as we do not consider the multi-alkali effect.

a) *Infinite diffusion source.* Concentration N_A at the glass surface (x=0) is kept constant during diffusion. Therefore, the initial and boundary conditions are

$$N_A(x,t=0) = 0, \qquad \text{for } x > 0, \quad (2.24a)$$

and at the surface,

$$N_A(x=0,t) = N_{A0}, \qquad \text{for } t \geq 0. \quad (2.24b)$$

At the other boundary for infinite glass thickness,

$$N_A(\infty,t)=0, \qquad \text{for } t \geq 0. \quad (2.24c)$$

The solution [Dore64, Cran75] of Eq.(2.23) is

$$N_A(x,t) = N_{A0}\ \mathrm{erfc}\left(\frac{x}{W_{eff}}\right), \qquad (2.25)$$

where erfc(u) is the complementary error function defined as

$$\mathrm{erfc}(u) \equiv 1 - \frac{2}{\sqrt{\pi}}\int_0^u \exp(-t^2)dt\ .$$

and is shown in Fig. 2-2, where $u = \frac{x}{W_{eff}}$ is the normalized distance. At a given time t, the effective width of the profile at u=1, is

$$W_{eff} = 2\sqrt{mD_At}\ , \qquad (2.26)$$

corresponding to the distance from the surface (x=0) to the position where N_A/N_{A0}=erfc(1)=0.1573. Note that the effective width W_{eff} of the waveguide is proportional to the square root of the diffusion time and the self-diffusion coefficient. The 1/e width of this profile is defined as [Rama86] $W_{1/e}$=0.6367·W_{eff}. Figure 2-2 also illustrates the normalized plots of both Gaussian and exponential profiles along with the normalized erfc(0.6367 u) curve for comparison purposes. All of the solid-line profiles are normalized so that the effective width now corresponds to $N_A(u=1)=N_{A0}/e$. The area under the normalized, dashed (complemetary error function) curve $N_A(u)$ is proportional to the total number of ions diffusing into the glass and is given by

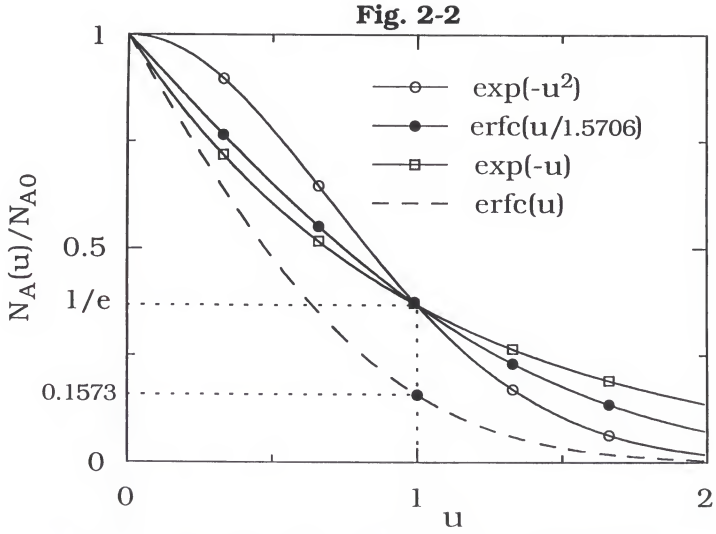

Fig. 2-2. Comparison between the normalized erfc function at 1/e point, Gaussian and exponential functions. The dashed curve is erfc(u).

$$A_1 = \int_0^{\infty} N_A(x,t)dx = \frac{N_{A0}W_{eff}}{\sqrt{\pi}}$$
$$= 2N_{A0}\sqrt{\frac{mD_At}{\pi}} \quad . \qquad (2.27)$$

Note that the area is proportional to the square root of the diffusion time implying that $\frac{dA_1}{dt}$ slows down with increasing time. It is clear that control of the total number of ions diffused improves with longer diffusion time.

b) *Finite diffusion source.* The concentration N_A of the diffusing ion A at the surface (x=0) decreases whenever these ions are not replenished during diffusion. As the diffusant is exhausted, the profile became closer to a Gaussian. Due to the difficulty in terminating the diffusion exactly at the point of exhaustion of the diffusion and the ambiguity involved in the profile, the problem is difficult to analyze. In addition, with the erfc function as the initial profile, it is rather difficult to solve the problem analytically. However, it becomes easier if we consider a delta function source as the initial condition for the diffusion process. This can be illustrated by considering a two-step process. To achieve a delta function profile in the first step, an extremely small amount of diffusion time is required. In the second step, annealing these samples permits the diffusion of the ions present just under the surface, further into the substrate. However, the area under the curve A_2 for several diffusion conditions (Fig. 2-3) and hence, also, the total

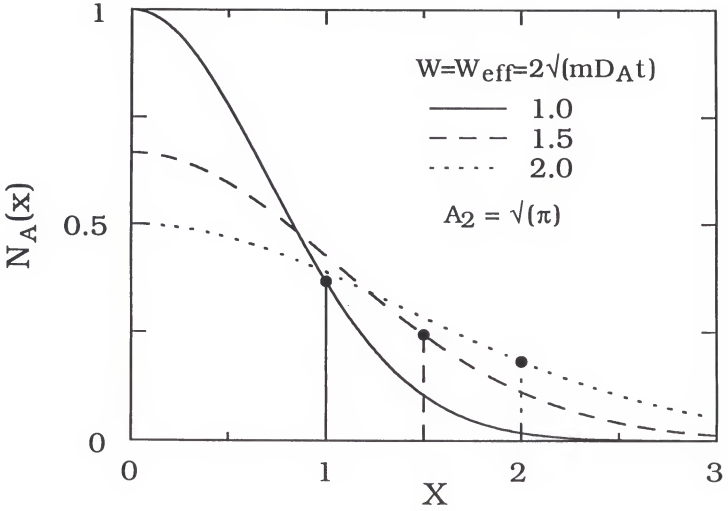

Fig. 2-3. The concentration profiles of finite diffusion source for W = 1.0, 1.5, and 2.0.

number of ions A in the glass remain constant. The conditions for the second step, which we term as postbaking, are

$$N_A(x,t=0) = 0 , \qquad \text{for } x > 0 ,$$
$$\text{and} \qquad \int_0^\infty N_A(x,t)dx = A_2 , \qquad \text{for } t \geq 0 . \tag{2.28}$$

Since the initial (first step) concentration profile is a delta function, the solution is a gaussian [Cran75], given by

$$N_A(x,t) = \frac{2A_2}{W\sqrt{\pi}} \exp\left[-\left(\frac{x}{W}\right)^2\right] , \tag{2.29}$$

where $W=W_{eff}=2\sqrt{mD_At}$ is now the depth at the 1/e point. The maximum concentration position always remains at x=0 and the maximum value decreases with increasing diffusion time and is inversely proportional to W, the 1/e width of the profile. Further diffusion, as shown in Fig. 2-3, does not alter the gaussian nature of the profile. The time t in this case represents the postbaking time.

2.2.4. Field Assisted Diffusion

An external field can assist the diffusion and, therefore, either the diffusion time or the diffusion temperature can be reduced to fabricate waveguides [Char78]. Furthermore, the field can drive the dopants deeper into the glass resulting in a buried waveguide, which is immune to surface scattering, in a two-step diffusion process, as described in chapter 3. Buried waveguides exhibit lower losses [Chen88].

Since an ionic current flows when an external field is applied, Eq. (2.16) is not valid in the case of an applied field. According to Eq. (2.2), the total flux of both ions normalized to the total mobile charges is expressed as

$$\frac{\vec{\phi}_A+\vec{\phi}_B}{C_0} = \mu_B(1-\alpha N_A)\vec{\mathcal{E}} + mD_B\alpha\nabla N_A , \qquad (2.30)$$

where we assume that the value of m is the same for the two cations. Using Eq. (2.17) and (2.30), the total field can be written as

$$\vec{\mathcal{E}} = \vec{\mathcal{E}_s} + \vec{\mathcal{E}_a} = -\frac{D_A}{\mu_A}\frac{\alpha\nabla N_A}{1-\alpha N_A} + \frac{\vec{\phi}_A+\vec{\phi}_B}{\mu_B(1-\alpha N_A)C_0} , \qquad (2.31)$$

$\vec{\mathcal{E}_a}$ is related to the current density $\vec{J}$ as

$$\vec{\mathcal{E}_a} = \frac{\vec{J}}{\mu_B(1-\alpha N_A)\left(\frac{C_0 F}{N_o}\right)} . \qquad (2.32)$$

where F is Faraday's constant (=96485 Coul/mole) and N_o is the Avogadro's number (=6.022X10^{23} $mole^{-1}$). In the case of no applied field ($\vec{\mathcal{E}_a}$=0), the current density $\vec{J}$ is zero. The space charge C_S is generally nonzero in the case of field-assisted diffusion if α is not zero. However, if N_A is much less than unity or the mobilities of ions A and B are equal, then Eq. (2.12) is still valid. The equation is also applicable in the case of small applied fields with a negligible space charge density. In these cases Eq. (2.12) can be rewritten as

$$\frac{\partial N_A}{\partial t} = mD_A\nabla^2 N_A - \mu_A\vec{\mathcal{E}}\cdot\nabla N_A , \qquad (2.33)$$

where the field is approximated by the applied field $\vec{\mathcal{E}}_a$. For one-dimensional diffusion, Eq. (2.33) is reduced to

$$\frac{\partial N_A}{\partial t} = mD_A \frac{\partial^2 N_A}{\partial x^2} - \mu_A \mathcal{E} \frac{\partial N_A}{\partial x} . \qquad (2.34)$$

For the conditions given by Eq. (2.24), an analytical solution is obtained [Malk61, Cuch61, Lili82] as

$$N_A = \frac{N_{A0}}{2} \{ \text{erfc}(u-u') + \exp(4uu') \, \text{erfc}(u+u') \} , \qquad (2.35)$$

where $u \equiv \frac{x}{W_{eff}}$, $u' \equiv \frac{\mu_A \mathcal{E} t}{W_{eff}}$, and W_{eff} is given by Eq. (2.26). Equation (2.35) is plotted in Fig. 2-4 as a function of u for various values of u'. u'=0, corresponds to the case with no applied field and the profile is an erfc function. For u' > 3 *i.e.*, in the case of large fields, the second term on the right hand side of the above equation is negligible [Rama86]. Thus,

$$N_A = \frac{N_{A0}}{2} \, \text{erfc}(u-u') . \qquad (2.36)$$

The width of the waveguide at the half-maximum approximately equals $\mu_A \mathcal{E} t$ for u' > 3. This depth of diffusion at the half maximum due to the diffusion of the ions into the substrate under applied field is clearly different from that in the case with no applied field, where the depth W_{eff} is proportioal to the square root of the diffusion time. The area under the steplike curve for u' > 3 approximately equals $u'N_{A0}$ and corresponds to a value of $\mu_A \mathcal{E} t N_{A0}$ ions.

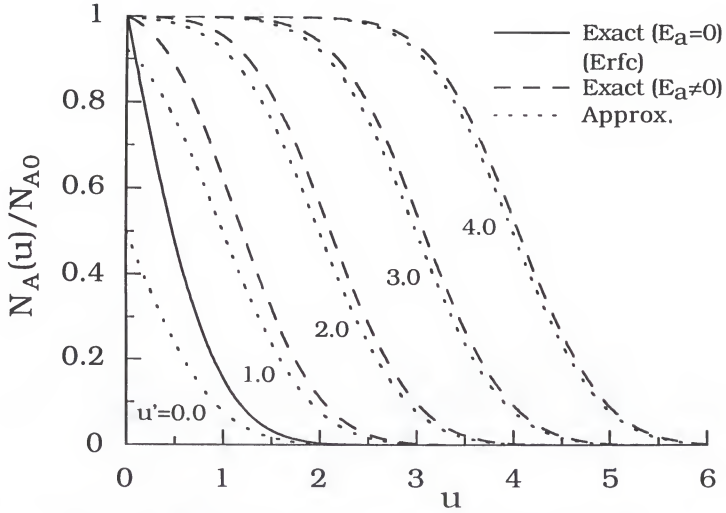

Fig. 2-4. The concentration profiles with and without the applied filed for u'=0.0, 1.0, 2.0, 3.0, and 4.0. The solid line (u'=0.0) is for E_a=0; the dashed lines are for E_a≠0 and the dotted lines are the approximation.

2.3. Silver-Sodium Ion Exchange

There are many ways to fabricate glass waveguides. The requirements of fabrication techniques or material systems to obtain high performance waveguide has been reviewed in detail in Ref. [Pitt81, Pitt82]. As discussed earlier, ion exchanges with different exchanging ion pairs have been used to fabricate optical waveguides in glass; for example, Ag^+-Na^+ [Gial73, Gede75a, Sava76, Gall76, Stew77, Walk83c, Lagu84b], K^+-Na^+ [Gial73, Yip84, Gort86a, Naja88b, Mili89], Tl^+-K^+ [Izaw72, Land85], Cs^+-Na^+ [Neum79], Cs^+-K^+ [Ross86], Li^+-Na^+ [Char80], *etc.* The index changes for the above cation pairs are listed in Ref. [Char82a, Find85, Rama88b]. Among them, the silver-sodium ion exchange is one of the most attractive ion pairs since 1) it is much less toxic compared to Tl^+, 2) the diffusion can be carried out at relatively low temperatures due to the relatively large diffusion coefficient of the silver ions, 3) a broad range of index changes (up to 0.1) is achievable in soda-lime glass simply by changing the concentration of the silver ions in the glass [Stew78, Houd86], and 4) the ionic size of Ag^+ (1.26Å) is close to that of Na^+ (0.95Å) resulting in negligible birefringence [Honk87b]. Single-mode waveguides (with smaller index change) can be fabricated by lowering the concentration of the silver ions in the glass. The propagation loss in the silver-sodium ion-exchanged waveguides is primarily caused by the absorption of the reduced silver ions in the glass [Gial73, Walk83c] and partially due to the scattering caused by the surface imperfections and inhomogeneities in the glass. The absorption occurs at 495 nm in the soda-lime glass [Faik83] due to the incorporation of the impurities

introduced in the glass during fabrication. The propagation loss can be decreased by using high quality optical glass as substrates with considerably lower impurity concentrations. Ag^+-Na^+ channel waveguides with an attentuation of less than 0.068 dB/cm at 0.633 μm in BK7 were first demonstrated by Eguchi *et al.* [Eguc83]. However, the loss (≈2 dB/cm at 0.633 μm) is higher in pyrex glass [Imai83]. By carefully choosing of the glass substrate and fabricating the waveguide, a propagation loss below 0.1 dB/cm is attainable for Ag^+-Na^+ exchanged single-mode channel waveguides [Rama88b].

The Ag^+-Na^+ exchanged glass waveguides can be fabricated by immersing the substrate into a molten salt bath or by the deposition of a metallic silver film and diffusion under an external electric field [Vilj80, Naja86, Terv87, Honk88, Zeng88]. In the latter technique a silver stripe is first deposited on the glass. Diffusion is then carried out at an elevated temperature with the aid of an electric field. The index change can be adjusted by varying the applied field [Naja86]. However, the propagation loss is somewhat higher than that of waveguides fabricated by the ion exchange process using the molten salt bath. The ion exchange process using the salt bath will be described in detail in chapter 4.

2.3.1. The Equilibrium Condition and the Index Change

When a glass substrate is immersed into a molten salt bath, ion exchange occurs across the interface when no external field is applied. The glass-melt interactions were first described in detail by Stern [Ster66]; this was followed by a theoretical study of the exchange and a

comparison to experimental results by Garfinkel [Garf68]. The exchange process reaches an equilibrium at the glass-melt interface and can be described as follows

$$A^{+}_{melt} + B^{+}_{glass} \rightleftharpoons A^{+}_{glass} + B^{+}_{melt} , \qquad (2.37)$$

where A and B represent silver and sodium ions, respectively. The exchange process is governed by the regular solution theory [Kirk61] in the melt and an m-type behavior in the glass [Karr62]. The relationship between the concentration N_A in the glass and $\overline{N_A}$ in the melt is given by [Garf68]

$$\ln\left(\frac{\overline{N_A}}{1-\overline{N_A}}\right) - \frac{H}{RT}\left(1 - 2\overline{N_A}\right) = m \ln\left(\frac{N_A}{1-N_A}\right) - \ln K , \qquad (2.38)$$

where H is the interaction energy of the two cations in the melt, R is the gas constant, T is the absolute temperature, and K is the equilibrium constant, given by [Karr62]

$$K = \frac{a_A \overline{a_B}}{a_B \overline{a_A}} . \qquad (2.39)$$

and a's without the bars represent the thermodynamic activities of the ions in the glass and those with bars represent the activities in the melt. Notice that a bar over the letter is used for the liquid phase, contrary to the notation in Refs. [Garf68, Chlu87, Rama88d]. $K > 1$ indicates the affinity of the glass for ion A *i.e.*, the glass prefers the intake of ion A and the equilibrium in Eq. (2.37) tends to move to the right hand side [Garf68]. In this case, the concentration of ion A in the glass is higher than that in the melt at equilibrium [Chlu87, Rama88d].

On the other hand, for $K < 1$, the glass prefers to retain ion B instead. The equilibrium constant depends on the diffusion temperature and the ion pair involved as well as the composition of the host glass. The experimental method to determine K is described in detail elsewhere [Rama88d]. In the case of Ag^+-Na^+ in soda-lime silicate glasses, K is much larger than unity, usually in the range of 75 to 120 [Rama88d]. Therefore, the exchange equilibrium tends to shift to the right hand side of Eq. (2.37) resulting in a much larger normalized concentration of the silver ions in the glass than in the melt. For example, N_{Ag} in soda-lime glass is known to be as large as 0.1 for 10^{-4} MF of the silver ion concentration in the melt [Chlu87, Rama88d]. Since the silver ion concentration in the glass is proportional to the index change, the control of the silver concentration in the melt is of paramount importance. In the case of the Ag^+-Na^+ exchange, Δn can be expressed empirically as $\Delta n \cong 0.1 \cdot N_{Ag}$ [Rama88d]. The concentration of the silver ions in the melt can be monitored using a concentration cell technique [Lagu84a] using an electrolytic technique to release the silver ions through a silver electrode [Lagu84b, Naja85], and feeding back the measured signal to control the electric current, thus, keeping the concentration of the silver ions constant in the melt. The electrolytic release is one of the advantages of the exchange with silver ions since high purity silver is available in electrode form and is a non-reactive metal. The index change can be controlled to an accuracy of 10^{-4} by this technique. This accuracy, as shown by Millar and Hutchins [Mill78], is required in fabricating passive waveguide devices with high performance.

The refractive index of glass depends on the glass composition [Hugg40, Hugg43, Abou88, Volf88]. Since only network modifiers in glass are involved in the exchange process, the glass structure is basically unchanged. Therefore, the index change of the glass is determined by the concentration of the exchanging ions in the glass. In the case of Ag^+-Na^+ exchanged waveguides fabricated using low melt concentrations, the index change is primarily due to the difference in the electronic polarizability of the ions. Silver ions have a larger polarizability (2.4 $Å^3$) than sodium ions (0.43 $Å^3$) [Find85], which results in an increase of the index upon exchange. The waveguide region is usually a few to a few tens of micrometers deep and has its maximum index at the surface. However, as has been pointed out earlier, the concentration of the silver ion in glass is not a linear function of that in the melt [Garf68]; especially at very low melt concentrations (10^{-4} MF) [Chlu87]. For single-mode waveguides with fiber-compatible mode sizes, an index change of 0.01 or less is required which corresponds to $N_{Ag} \cong 0.1$ in the glass or $\overline{N_{Ag}} \cong 2x10^{-4}$ MF in the melt [Chen87, Rama88a].

2.3.2. Space Charge Effect and Multi-Alkali Effect

Space Charge Effect

As discussed previously, the space charge is usually non-zero even when no external field is applied during the exchange. The space charge density primarily depends on the mobility ratio between the two exchanging ions, no space charge is created if the ratio is one. In the case of Ag^+-Na^+ exchange in BK7 glass, the mobility of the sodium

ions is about 80 times larger than that of the silver ions [Chen90a]. Since the sodium ions have higher mobility, under the chemical potential difference during the diffusion process, the movement of the sodium ions from the glass into the melt is easily accomplished leaving vacancies with net negative charges. An electric potential, therefore, develops balancing the diffusion process. The induced field affects the movement of both the silver and sodium ions. The electric potential corresponding to the induced field opposes the chemical potential driving the Na^+ ions whereas it aids that of the Ag^+ ions. As a result, the out-diffusion of the sodium ions is slowed down and the movement of the silver ions into the glass is accelerated. The ion-exchange process is affected by both the diffusion under the chemical potential and the drift by the induced electric field. This effect is reflected in the inter-diffusion coefficient, shown in Eq. (2.15). If the denominator of the right hand side of Eq. (2.15) approaches zero *viz.*, $\alpha N_A \rightarrow 1$, in other words, both $D_A << D_B$ and $N_A \rightarrow 1$ must be satisfied. In this case, the inter-diffusion coefficient $\widetilde{D}$ is much larger than the self-diffusion coefficient D_A. This effect is especially profound at the surface of the waveguide since the concentration of silver ions is maximum at the surface. The diffusion is faster at the surface than it is deeper into the substrate. Hence, a large concentration gradient is formed between the region with $\alpha N_A \rightarrow 1$ (at surface) and $\alpha N_A << 1$ (near the tail of the index profile) and this gradient gradually moves into the substrate during the diffusion process. The index profile, in this case, is no longer a complementary error function as is expected for the infinite source diffusion; instead it may become a Gaussian-like ($\alpha N_A \lesssim 1$) [Chen90a] or a step function (*e.g.*, $\alpha N_A \approx 0.999$ for Cs^+-Na^+ in soda-

lime glass) [Neum79] because of the larger inter-diffusion coefficient at the surface. It is clear that as αN_A approaches unity, the diffusion profile is essentially similar to that of the linear cases with the applied external field as seen later in the numerical simulation.

Multi-Alkali Effect

The inter-diffusion coefficient is concentration-dependent as shown in Eq. (2.15) where a constant self-diffusion coefficient was used in the derivation since the interactions between the exchanging ions in glass is negligible. However, the self-diffusion coefficients are often functions of concentrations if the two exchanging ions interact during the diffusion process. The inter-dependence results in the correlation of the diffusion coefficients of the two exchanging alkali ions [Isar69, Day76], known as the multi-alkali effect. Jain *et al.* [Jain83] have studied this effect rigorously in the case of sodium-cesium silicate glass. Although silver does not belong to the alkali group (Group IA), it is known to affect the interaction energy of the sodium ions in the glass, as reported in Ref. [Neum79]. The self-diffusion coefficient of the silver ions increases as the concentration of the silver ions N_{Ag} increases as demonstrated in the Ag^+-Na^+ exchanged soda-lime glass [Rama86]. However, the self-diffusion coeffient of the sodium ions decreases as N_{Ag} increases. This results in a space-charge behavior and causes the concentration profile of the silver ion in glass to be closer to a Gaussian function even at low concentrations *e.g.*, 0.5 MF [Chen90a].

2.3.3. Temperature Dependence of the Self-Diffusion Coefficient

Both the self-diffusion coefficient and the mobility of the exchanging ions in glass depend on temperature. It is well known that glass exhibits different diffusion characteristics above and below the glass transition temperature [Ster66, Dore69]. Kaps and Völksch [Kaps82] experimentally demonstrated this temperature dependency in the case of Ag^+-Na^+ in $Na_2O \bullet 2SiO_2$ glass; they also measured the sodium self-diffusion coefficient by isotope substitution in the same glass [Kaps84]. However, we are only interested in diffusion below the glass transition temperature. The temperature dependence of the self-diffusion coefficient below the glass transition temperature follows the well-known Arrhenius relation [Dore64, Ster66]

$$D_A = D_{Ao} \exp(-\frac{\Delta H}{RT}) , \qquad (2.40)$$

where ΔH is the activiation energy, R is the gas constant, T is the absolute temperature, and D_{Ao} is a constant. In general, both D_{Ao} and ΔH depend on the glass composition and concentration of the diffused ions as well as the ion pair involved in the exchange. For Ag^+-Na^+ exchange in BK7 glass, D_{Ao} and ΔH in the above equation are found to be 3.71×10^6 μm^2/min and 105.1 KJ/mole, respectively, with a melt composition of 10^{-3} MF of silver ions, 0.33 MF of potassium ions, and 0.67 MF of sodium ions [Chen90a], where m is assumed to be unity. The activiation energy ΔH is 98.7 KJ/mole as reported by Eguchi *et al.* [Eguc83]. The technique to determine D_{Ao} and ΔH will be presented in chapter 4.

2.4. Summary

We have theoretically discussed the concentration profiles of ion exchanged waveguides in glass with or without an externally the applied electric field in glass. The nonlinear diffusion equation is derived from fundamental principles such as Fick's law, continuity equation and Gauss's laws. That equation can be linearized if the product αN_A is close to zero, *i.e.*, equal mobilities of both ions and/or low concentration of ion A in glass. Analytical, closed form solutions are possible for the one-dimensional case with or without an applied field in glass. However, in the two-dimensional case, the equation must be solved by numerical techniques, as will be presented in the next chapter.

CHAPTER 3
NUMERICAL MODELING OF PLANAR AND CHANNEL WAVEGUIDES

3.1. Introduction

Planar waveguides confine the light in one of the transverse directions, namely the thickness direction, whereas channel waveguides confine the light in both transverse directions. These waveguides, channel waveguides in paricular, are the basic building blocks of sophisticated guided-wave, integrated optical devices for applications in optical communication and signal processing systems. The understanding of the waveguiding characteristics of both the planar and channel waveguides is essential in the design of high performance devices.

Prior to solving the problem of wave propagation in waveguides, we must first solve the nonlinear diffusion equation discussed in the previous chapter to determine the index profiles of both the 1-D and 2-D cases. The diffusion profile depends upon the cation pairs, the characteristics of the host glass and the fabrication conditions; analytical solutions applicable to planar waveguides in certain cases were presented in the previous chapter.

The first part of this chapter deals with numerical solutions for the diffusion equation where closed form solutions are not available. Nowadays, exact solutions of the nonlinear diffusion equation are possible using numerical techniques due to the availability of high

speed computers at low cost. The modeling allows us to optimize the process, tailor the index profile and attain optimal mode size to match other optical devices. Besides, it is quite helpful in the design of complex devices. In the later part of this chapter, several numerical methods are presented for solving the Helmholtz wave equation for both the 1-D and 2-D cases.

Under certain conditions outlined in the last chapter, the nonlinear equation can be linearlized; often, depending upon the characteristics of the cation pairs in the host glass and their concentrations, the exchange process can be treated as a single species diffusion. Closed form solutions are not always available even for the linear case depending on the initial and boundary conditions. The resulting diffusion equation Eq. (2.19) in such cases as well as the nonlinear equation Eq. (2.18) can be solved numerically by using a number of approaches. One such appproach that is quite useful is Green's function method illustrated in the subsequent section. This method is especially useful in the numerical solutions of 1-D surface and buried waveguides as well as 2-D surface waveguides. However, in general, the Green's function approach is not applicable to the nonlinear equation. In that case, the well known finite difference method (FDM) may be employed. In the following subsection, both approaches, *viz.*, the Green's function and FDM are discussed.

The concentration profile of the diffused ions is assumed to approximate the index profile of the waveguide. Once the index profile is known, the fields in the waveguide can be found by solving the Helmholtz wave equation. The Helmholtz equation can be solved numerically by a number of well known methods: the WKB method,

the matrix method, 1-D FDM, a variational approach using finite element method (FEM), perturbation techniques, *etc.* for the one-dimensional case and the effective-index method (EIM) [Rama74, Hock77, Chia86, Veld88], 2-D FDM [Ster88a, Ster88b], again variational approach [Mats73, Mish86, Haus87b] with FEM [Yeh79, Maba81, Kosh85a, Kosh85b, Lagu86b], perturbation technique [Kuma83], spectral index method [Mcil89, Mcil90, Ster90], *etc.* for the two-dimensional case. A comprehensive review of some of the above techniques is presented by Kogelnik [Koge88]. In this chapter numerical approaches applicable to one-dimensional waveguides by using WKB, matrix, and FDM methods are illustrated. This is followed by a discussion of EIM and FDM techniques, as applied to 2-D waveguides.

In all of the above techniques, we assume a z-invariant (*i.e.*, invariant in the direction of propagation) index profile. Some integrated optical devices involve tapered waveguides, cross-couplers, Y-junctions, *etc.* In these cases, the index profile is z-dependent and a number of numerical techniques that simulate the evolution of the propagating wave such as the step transition method [Marc70], the local normal mode approach [Marc74] and the beam propagation method (BPM) [Flec76, Feit78, Feit79, Feit80] are applicable. We discuss, in particular, the BPM technique which is becoming increasingly popular for characterizing these waveguide devices.

3.2. Graded-Index Profile

In this section, we first solve the linear diffusion equation in the one-dimensional case, with (Eq. (2.34)) and without (Eq. (2.23)) an applied field, for the index profile using both the Green's function and FDM approaches. The techniques are, then, extended to solve the nonlinear diffusion equation for the 2-D profiles.

3.2.1. Green's Function: One Dimensional Case

For the one-dimensional case, the linear equation Eq. (2.34) is considered in this subsection. For the diffusion without a field, $\mathcal{E}$ is set to zero and Eq. (2.34) reduces to Eq. (2.23). Green's functions are used to solve Eq. (2.34) by considering an impulse input function at an arbitrary position at time t=0 [Chen87, Rama88a].

Impluse Response

Consider an arbitrary concentration profile as the initial condition $N_A^0(x) \equiv N_A(x,t=0)$; For computational purposes, we can discretize the initial index profile and sum the values of N_A at discrete points located at $x = x_i$, i=0, ±1, ±2, *etc.*

$$N_A^0(x) = \sum_i N_A^0(x_i)\cdot\delta(x-x_i) \ , \qquad (3.1)$$

where $\delta(x-x_i)$ is the delta function. Each delta function $\delta(x-x_i)$ can be treated as a finite source at $x=x_i$, infinite in extent in both y and z directions and $N_A^0(x_i)$ represents the normalized concentration of the diffusant at $x = x_i$. Figure 3-1(a) shows the initial concentration profile represented by the delta functions at $x=...,x_{-1},x_0,x_{+1},...$, *etc.* For each

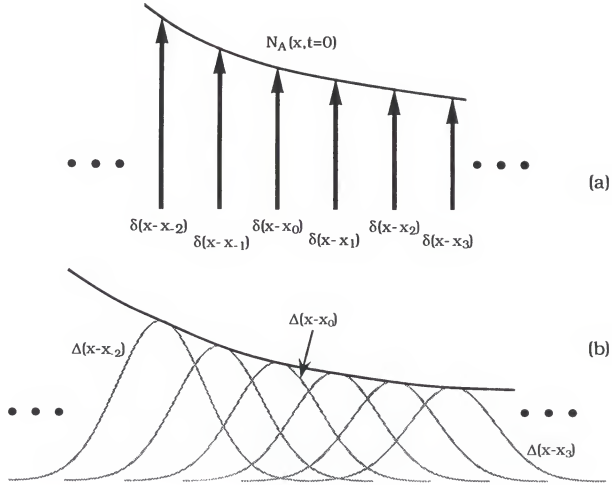

Fig. 3-1. (a) Initial condition represented by the delta functions $\delta(x-x_i)$;
(b) Normalized diffusion profile after time t (dark lines)
composed by individual gaussian functions $\Delta(x-x_i)$ (light lines).

delta function input, the solution of Eq. (2.34) is given by the Green's function [Cran75],

$$\Delta(x-x_I,t) = \frac{1}{\sqrt{4\pi m D_A t}} \exp\left[-\frac{(x-x_I-\mu_A \mathcal{E} t)^2}{4mD_A t}\right] . \qquad (3.2)$$

After time t, the finite planar source diffuses and becomes a Gaussian function in one dimension, with its half-width at 1/e point $W_{1/e} = 2\sqrt{mD_A t}$ and the amplitude $\frac{1}{W_{1/e}\sqrt{\pi}}$. Summing up all the impulse responses, as seen from Fig. 3-1(b), the solution of Eq. (2.34) with the initial condition $N_A^o(x)$ can be obtained.

$$N_A(x,t) = \sum_i N_A^o(x_I)\Delta(x-x_I,t)$$

$$= \sum_i \frac{N_A^o(x_I)}{W_{1/e}\sqrt{\pi}} \exp\left[-\left(\frac{x-x_I-\mu_A \mathcal{E} t}{W_{1/e}}\right)^2\right] . \qquad (3.3)$$

As the number of discrete points increases, the summation in Eq. (3.3) can be written as an integral

$$N_A(x,t) = \int_{-\infty}^{\infty} N_A^o(x')\Delta(x-x',t)dx' . \qquad (3.4)$$

where $\Delta(x-x',t)$ is given by Eq. (3.2). The initial and boundary conditions are given by Eq. (2.24). To accommodate the diffusion on both sides of the planar source, the limits of the integral are chosen from $x = -\infty$ to $+\infty$. Furthermore, for computational purposes, we will assume the melt ($x < 0$) is replaced by a virtual host glass with the same diffusion characteristics. In other words, the host glass is assumed to be infinite in extent in both directions. The integration is

performed for very small time steps $t = \Delta t$. The resulting profile is used as the initial condition for the subsequent integration. The process continues until the desired time of diffusion t is reached by successive integrations at intervals Δt, the sum of which makes up the time t. The above procedure is especially suited for the two step diffusion process, where the diffusion profile of the first step is used as the initial condition $N_A^o(x) = N_A(x,t = 0)$ for the second step using the Green's function method as described above.

Surface Waveguides with Inifite Source—One-Step Process

The above procedure can also be used for solving the first diffusion step with either a finite or an infinite source. For the infinite source, the concentration of the diffusants remains constant at all times at the surface of the glass. Therefore, we must assume that the boundary condition at $x \leq 0$ is $N_A^o(x,t) = N_{A0}$; note that the value of N_{A0} does not remain the same near the surface with time $t > 0$, if Eq. (3.4) is employed. As before, we divide the time t into many intervals Δt and recursively evaluate the integral for all time steps; however, we need to reset the boundary condition $N_A(x \leq 0,t) = N_{A0}$ for each evaluation of the integral at successive Δt's. Thus, the evolution of the concentration profile is continued until the final solution is reached. The accuracy has been checked for the infinite-source case where the analytical solution is given by Eq. (2.32). We use the same values of the diffusion parameters for both the analytical and numerical solutions. We obtained a better accuracy for $\mathcal{E} \neq 0$, especially when the slope of the concentration profile at $x = 0$ is nearly zero as shown in Fig. 3-2 for the curve identified as 2. Curve 1 represents the case without the field

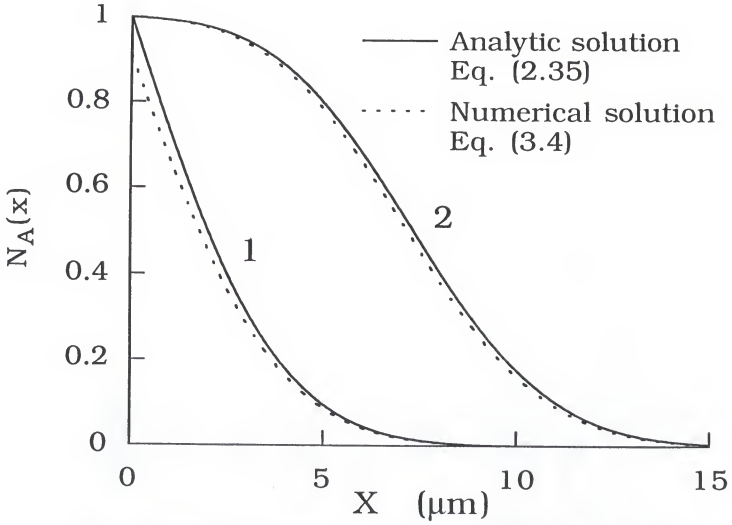

Fig. 3-2. Concentration profiles with and without applied field for t=30 min, mD_A=0.15 μm^2/min, μ_A=5.0 $\mu m^2/V \cdot min$ and $\mathcal{E}$=45 V/mm. The solid and dashed lines are evaluated by Eq. (2.35) and Eq. (3.4), respectively. The curves 1 and 2 denote the diffusion without and with the applied field, respectively.

and corresponds to an erfc profile. The solid lines represent the analytical result while the dashed lines denote the numerical solution.

Buried Waveguides—Two-Step Process

The surface waveguides in Fig. 3-2 are fabricated by a single-step diffusion process. To fabricate buried waveguide by exchanging ions in the molten salt, a two-step process is needed. The second step process involves the sample from the first step being diffused in molten salt bath containing no A (silver) ions, again with or without the application of an external field. In this case, the boundary condition is $N_A(x < 0,t) = 0$. The concentration profile of the first step becomes the initial condition for the second step.

a) *Arbitrary electric field E_2 or time t_2.* The numerical solution can be obtained by following the same procedure used in the calculation of the first step, *i.e.*, integrating Eq. (3.4) now with different boundary conditions. Figure 3-3 shows the one-step diffusion profile, namely, the erfc profile identified as 1, as well as the second step diffusion profiles with an arbitrary applied field in the second step, identified by 2 through 4 in the figure with profile 1 as the initial condition. x_p and W are the peak position and 1/e full width of the resulting profiles, respectively. Note that for small applied fields E_2 and/or for small diffusion times t_2 in the second step, $N_A(0, t_2)$ never equals zero, but it may be close, as seen in Fig. 3-3(curve 2). Note that $N_A(x < 0,t_2) = 0$. However, with increasing t_2 for a given E_2 and/or for large E_2, $N_A(0, t_2)$ becomes zero as seen from Fig. 3-3(curves 3 and 4). It is obvious that for achieving almost symmetric, buried waveguides the application of the field in the second step is necessary.

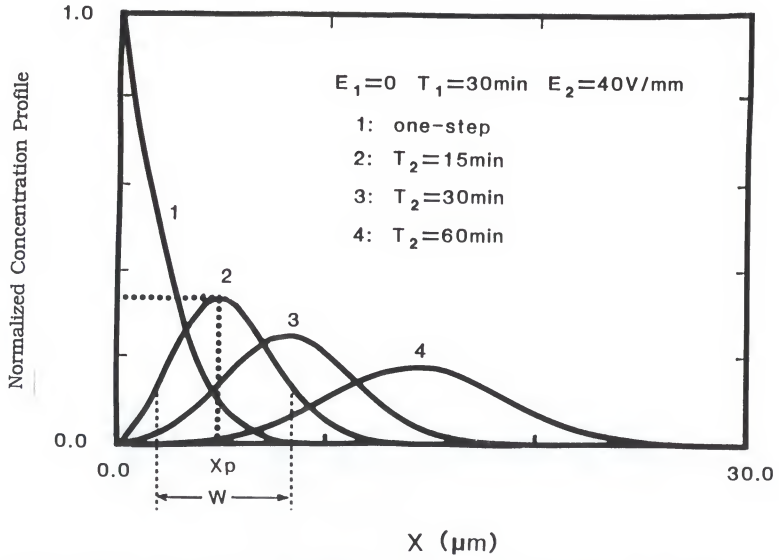

Fig. 3-3. The one-step and two-step diffusion profiles. In the first step, the diffusion time T_1 is 30 min and no applied field E_1=0, denoted as 1. In the second step, the applied E_2= 40 V/mm and the diffusion times T_2 are 15, 30 and 60 min denoted as 2, 3, and 4, respectively.

b) *Large E_2 and/or t_2.* We now assume that in the second step, the applied field is sufficiently large to block the out-diffusion of ion A into the melt. Rewriting the position x and the location of the delta function source x' in terms of the normalized variables u and u', the resulting index profile, for $u \geq \frac{-\mu_A \mathcal{E} t_2}{W_{eff2}}$ again with the boundary condition $N_A(x < 0, t) = 0$, can be obtained from Eq. (3.4) as

$$N_A(u) = \int_0^\infty \frac{N_{A1}(u'\sqrt{\tau})}{\sqrt{\pi}} \exp[-(u-u')^2]du' , \qquad (3.5)$$

where $u \equiv \frac{x-\mu_A \mathcal{E} t_2}{W_{eff2}}$, $u' \equiv \frac{x'}{W_{eff2}}$, $\tau = \frac{t_2}{t_1}$, $W_{eff2} = 2\sqrt{mD_A t_2}$, t_1 and t_2 are the diffusion time in the first and second steps, respectively, and $N_{A1}(\frac{x\sqrt{\tau}}{W_{eff2}})$ is the concentration profile of the single-step process, *e.g.*, $N_{A1}(\frac{x\sqrt{\tau}}{W_{eff2}}) = N_{A0}\,\mathrm{erfc}(\frac{x}{2\sqrt{mD_A t_1}})$ for $\mathcal{E} = 0$.

3.2.2. Green's Function: 2 and 3 Dimensional Cases

In the one dimensional case, the impulse response of Eq. (2.34) was expressed by Eq. (3.2). The Green's function method can easily be extended to 2-D and 3-D problem. In the cases of 2-D and 3-D diffusions, the impulse responses become [Cran75]

$$\Delta(x-x_i, y-y_i, t) = \frac{1}{4\pi m D_A t} \exp\left[-\frac{(x-x_i-\mu_A \mathcal{E}_x t)^2+(y-y_i-\mu_A \mathcal{E}_y t)^2}{4mD_A t}\right], \qquad (3.6)$$

and $$\Delta(x-x_i,y-y_i,z-z_i,t) = \frac{1}{\sqrt{(4\pi m D_A t)^3}} \cdot \exp\left[-\frac{\sum_{q=x,y,z}(q-q_i-\mu_A \mathcal{E}_q t)^2}{4mD_A t}\right] , \quad (3.7)$$

respectively, where $\mathcal{E}_q$ denotes the component of the applied field in the q (= x, y, or z) direction. The boundary conditions for 2-D or 3-D cases make the numerical calculation by the Green's function method very complicated. Since a considerably large amount of CPU time is required to evaluate the integrals, the Green's function approach may not be practical. Furthermore, the Green's function approach is not applicable for solving the nonlinear diffusion equation. The finite difference method is more suitable and is described in the following section.

3.2.3. Finite Difference Method (FDM)

To illustrate FDM, we begin by considering the one dimensional Taylor's expansion. By truncating Taylor's series, the finite difference is used to approximate the derivatives in the differential equations. Let us employ this technique to the one-dimensional linear equation Eq. (2.23) first. The second derivative of N_A with respect to x can be expressed by the second-order, central difference method, as

$$\left.\frac{\partial^2 N_A}{\partial x^2}\right|_{x_i} \cong \frac{N_A(i+1)-2N_A(i)+N_A(i-1)}{(\Delta x)^2} , \quad (3.8)$$

where the integers i+1, i, and i-1 in the parentheses denote the positions at $x = x_{i+1}$, x_i, and x_{i-1}, respectively, and Δx is the difference

in position between two adjacent grid points. To accommodate the change in concentration N_A with time, the concentration can be written as $N_A(i,j)$, where i denotes the position x_i and j corresponds to the diffusion time t_j. Eq. (3.8) can, therefore, be rewritten in terms of $N_A(i,j)$ as

$$\left.\frac{\partial^2 N_A}{\partial x^2}\right|_{x_i,t_j} \cong \frac{N_A(i+1,j)-2N_A(i,j)+N_A(i-1,j)}{(\Delta x)^2} . \qquad (3.9)$$

The left hand side of Eq. (2.23) can again be approximated by the central difference method as

$$\left.\frac{\partial N_A}{\partial t}\right|_{x_i,t_{j+0.5}} \cong \frac{N_A(i,j+1)-N_A(i,j)}{\Delta t} , \qquad (3.10)$$

where the derivative of the concentration N_A in Eq. (3.10) is evaluated at $t = t_{j+0.5}$ rather than $t = t_j$ or t_{j+1} and identified by the subscript on the left hand side of Eq. (3.10) as $t_{j+0.5}$. However, a problem arises due to the fact that the time $t = t_{j+0.5}$ in Eq. (3.10) is ahead by 0.5 units from that in Eq. (3.9). This difficulty is addressed in detail in the following subsection.

1-D Linear Diffusion Equation, without Field

Equation (2.23) describes the diffusion equation for the linear case. As discussed above, Eqs. (3.9) and (3.10) represent the derivatives at two different times. Equating the two equations with different times

$$\left.\frac{\partial N_A}{\partial t}\right|_{x_i,t_{j+0.5}} \cong mD_A \left.\frac{\partial^2 N_A}{\partial x^2}\right|_{x_i,t_j} , \qquad (3.11)$$

may result in larger truncation errors. Crank [Cran75] resolved this problem by rewriting RHS of Eq. (3.11) as an average of $\frac{\partial^2 N_A}{\partial x^2}$ between t_j and t_{j+1}:

$$\left.\frac{\partial N_A}{\partial t}\right|_{x_i,t_{j+0.5}} \cong \frac{mD_A}{2}\left(\left.\frac{\partial^2 N_A}{\partial x^2}\right|_{x_i,t_j} + \left.\frac{\partial^2 N_A}{\partial x^2}\right|_{x_i,t_{j+1}}\right). \qquad (3.12)$$

As a result, the truncation error is reduced for the second-order central difference formula. The finite difference form of Eq. (3.12) can then be expressed as

$$\frac{N_A(i,j+1)-N_A(i,j)}{\Delta t} = \frac{mD_A}{2}\left(\frac{N_A(i+1,j)-2N_A(i,j)+N_A(i-1,j)}{(\Delta x)^2} + \frac{N_A(i+1,j+1)-2N_A(i,j+1)+N_A(i-1,j+1)}{(\Delta x)^2}\right) \qquad (3.13)$$

where the order of total error is $O\{(\Delta t)^2+(\Delta x)^2\}$. By defining $r_1 = \frac{mD_A}{2}\frac{\Delta t}{(\Delta x)^2}$, Eq. (3.13) becomes

$$r_1 N_A(i-1,j+1)+(-1-2r_1)N_A(i,j+1)+r_1 N_A(i+1,j+1) = -r_1 N_A(i-1,j)+(-1+2r_1)N_A(i,j)-r_1 N_A(i+1,j) \qquad (3.14)$$

The left hand side represents the time $t=t_{j+1}$ where N_A at position $x=x_{i-1}$, x_i, and x_{i+1} are unknown, while the right hand side represents the time $t=t_j$ where N_A at $x=x_{i-1}$, x_i, and x_{i+1} are obtained from the calculation in the previous step. In the case of $j=0$, N_A is given by the initial condition at the three positions $x=x_{i-1}$, x_i, and x_{i+1}. The computation width in the x direction is discretized say, into $\mathcal{K}$ points.

The boundary conditions of N_A, *viz.*, $N_A(0, j+1)$ and $N_A(\mathcal{K}+1, j+1)$, at the extremities $x = x_0$ and $x_{\mathcal{K}+1}$ at $t=t_{j+1}$ are usually known. Therefore, the unknowns are $N_A(1,j+1)$, $N_A(2,j+1)$,..., $N_A(\mathcal{K},j+1)$ and the total number of the unknowns is $\mathcal{K}$. A matrix form representation of Eq. (3.14) can be obtained which is easily solved for the unknowns by the available scientific subroutine library such as IMSL or ESSL.

$$\mathbf{A}_{1\,\mathcal{K}\times\mathcal{K}}\,\mathbf{N_A}(j+1)_{\mathcal{K}\times 1} = \mathbf{A}_{2\,\mathcal{K}\times\mathcal{K}}\,\mathbf{N_A}(j)_{\mathcal{K}\times 1} - \mathbf{B}(j+1)_{\mathcal{K}\times 1}\,, \qquad (3.15)$$

where $$\mathbf{N_A}(j)^T=\left[N_A(1,j),\ldots,N_A(\mathcal{K},j)\right]\,,$$

the boundary conditions $$\mathbf{B}(j+1)^T=\left[r_1 N_A(0,j+1),0,\ldots,0,r_1 N_A(\mathcal{K}+1,j+1)\right],$$

$$\mathbf{A}_{1\,\mathcal{K}\times\mathcal{K}}=\begin{bmatrix} -1-2r_1 & r_1 & & 0 \\ r_1 & -1-2r_1 & \ddots & \\ & \ddots & \ddots & r_1 \\ 0 & & r_1 & -1-2r_1 \end{bmatrix},$$

$$\mathbf{A}_{2\,\mathcal{K}\times\mathcal{K}}=\begin{bmatrix} -1+2r_1 & -r_1 & & 0 \\ -r_1 & -1+2r_1 & \ddots & \\ & \ddots & \ddots & -r_1 \\ 0 & & -r_1 & -1+2r_1 \end{bmatrix}$$

and the superscripts T represent the transpose of the matrix. Notice that $\mathbf{A_1}_{\mathcal{K}\times\mathcal{K}}$ is a tri-diagonal, symmetrical matrix. This method is implicitly stable and the truncation error in the calculation is negligible as $\frac{\Delta t}{(\Delta x)^2}$ becomes smaller [Cran75]. However, the round-off error due to the limited accuracy of the representation of a number in computer is accumulated in each time step, so that the deviation from

the exact solution becomes larger for smaller $\frac{\Delta t}{(\Delta x)^2}$ and more time steps. To reduce the error, we use $\frac{mD_A}{2}\frac{\Delta t}{(\Delta x)^2} \sim 10^{-3}$ at the beginning of the calculation and ~ 0.1 during the final steps of the evaluation.

1-D Linear Diffusion Equation, with Field

For diffusion with an applied field, corresponding to the linear equation expressed by Eq. (2.34), Eq. (3.12) can be modified by adding one more term to include the drift component:

$$\left.\frac{\partial N_A}{\partial t}\right|_{x_i,t_{j+0.5}} \cong \frac{mD_A}{2}\left(\left.\frac{\partial^2 N_A}{\partial x^2}\right|_{x_i,t_j} + \left.\frac{\partial^2 N_A}{\partial x^2}\right|_{x_i,t_{j+1}}\right) + \frac{\mu_A \mathcal{E}}{4}\left(\left.\frac{\partial N_A}{\partial x}\right|_{x_{i+0.5},t_j} + \left.\frac{\partial N_A}{\partial x}\right|_{x_{i-0.5},t_j} + \left.\frac{\partial N_A}{\partial x}\right|_{x_{i+0.5},t_{j+1}} + \left.\frac{\partial N_A}{\partial x}\right|_{x_{i-0.5},t_{j+1}}\right). \quad (3.16)$$

where

$$\left.\frac{\partial N_A}{\partial x}\right|_{x_{i+0.5},t_j} + \left.\frac{\partial N_A}{\partial x}\right|_{x_{i-0.5},t_j} = \frac{N_A(i+1,j)-N_A(i,j)}{\Delta x} + \frac{N_A(i,j)-N_A(i-1,j)}{\Delta x} = \frac{N_A(i+1,j)-N_A(i-1,j)}{\Delta x}.$$

Similarly, Eq. (3.13) can be rewritten for the field-assisted diffusion as

$$\frac{N_A(i,j+1)-N_A(i,j)}{\Delta t} = \frac{mD_A}{2}\left(\frac{N_A(i+1,j)-2N_A(i,j)+N_A(i-1,j)}{(\Delta x)^2} + \frac{N_A(i+1,j+1)-2N_A(i,j+1)+N_A(i-1,j+1)}{(\Delta x)^2}\right) + \frac{\mu_A \mathcal{E}}{4}\left(\frac{N_A(i+1,j)-N_A(i-1,j)}{\Delta x} + \frac{N_A(i+1,j+1)-N_A(i-1,j+1)}{\Delta x}\right). \quad (3.17)$$

Let $$r_1 = \frac{mD_A}{2}\frac{\Delta t}{(\Delta x)^2}$$

and $$r_2 = \frac{\mu_A \mathcal{E}}{4}\frac{\Delta t}{\Delta x}.$$

With these substitutions, Eq. (3.17) can be rewritten in matrix form similar to Eq. (3.15) with the matrices $\mathbf{A_1}$, $\mathbf{A_2}$ and the boundary condition $\mathbf{B}(j+1)$ now defined as

$$\mathbf{A}_1 = \begin{bmatrix} -1-2r_1 & r_1+r_2 & & 0 \\ r_1-r_2 & -1-2r_1 & \ddots & \\ & \ddots & \ddots & r_1+r_2 \\ 0 & & r_1-r_2 & -1-2r_1 \end{bmatrix}, \quad \mathbf{A}_2 = \begin{bmatrix} -1+2r_1 & -r_1-r_2 & & 0 \\ -r_1+r_2 & -1+2r_1 & \ddots & \\ & \ddots & \ddots & -r_1-r_2 \\ 0 & & -r_1+r_2 & -1+2r_1 \end{bmatrix} \quad \text{and}$$

$\mathbf{B}(j+1)^T = \left[(r_1-r_2)N_A(0,j+1), 0, \ldots, 0, (r_1+r_2)N_A(\mathcal{K}+1,j+1)\right]$. Again $\mathbf{A_1}$ is a tri-diagonal matrix although not symmetrical. The finite difference method is more flexible for various boundary conditions compared to the Green's function method.

2-D Linear Diffusion Equation

For the case of the 2-D diffusion equation, the concentration array $\mathbf{N_A}(j)$ is illustrated in Fig. 3-4, where the dots represent the mesh points and total number of points is $\mathcal{K}_x\mathcal{K}_y$. The matrix $\mathbf{A_1}$ then becomes a block tri-diagonal matrix with the size of $\mathcal{K}_x\mathcal{K}_y$ by $\mathcal{K}_x\mathcal{K}_y$, which has the order of $\mathcal{K}^4$ if $\mathcal{K}_x=\mathcal{K}_y=\mathcal{K}$. The size of the matrix can be reduced by employing the nonuniform meshes in the two-dimensional case. However, the CPU time may increase enormously for nonuniform meshes for the same size of the matrix $\mathbf{A_1}$.

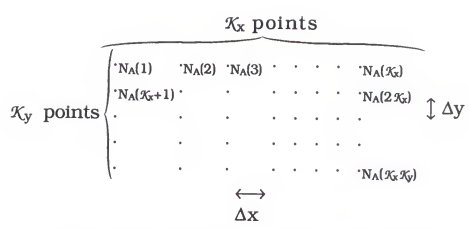

Fig. 3-4. Two-dimensional mesh points. Δx and Δy are the grid sizes.

1-D and 2-D Nonlinear Diffusion Equation

The implicit finite difference method as described above has the advantages of convergence and stability. Yet it is impossible to convert a nonlinear differential equation, *e.g.*, Eq. (2.22), into a matrix form since the matrix operation is intrinsically linear in nature. To solve the nonlinear diffusion equation, an explicit finite difference method with iterations is introduced. Iteration loops are used in each time step to achieve accurate results. The method is described below.

Considering Eq. (2.22), the concentration N_A at $t=t_{j+1}$ can be estimated as

$$\begin{aligned}\left.\frac{\partial N_A}{\partial t}\right|_{x_i,t_{j+1}} &\cong \left.\frac{\partial N_A}{\partial t}\right|_{x_i,t_{j+0.5}} \\ &= \frac{1}{2}\left(\frac{\partial}{\partial x}\left(\frac{mD_A}{1-\alpha N_A}\frac{\partial N_A}{\partial x}\right)\right|_{x_i,t_j} + \left.\frac{\partial}{\partial x}\left(\frac{mD_A}{1-\alpha N_A}\frac{\partial N_A}{\partial x}\right)\right|_{x_i,t_{j+1}}\Bigg) \qquad (3.18) \\ &\cong \left.\frac{\partial}{\partial x}\left(\frac{mD_A}{1-\alpha N_A}\frac{\partial N_A}{\partial x}\right)\right|_{x_i,t_j} .\end{aligned}$$

It is assumed that $N_A(t=t_{j+1}) \cong N_A(t=t_j)$ for small time step Δt in the above equation. The assumption is valid for very small Δt. However, the truncation error induced in the calculation of each time step may accumulate and result in large error. Therefore, iteration loops are used in each time step to refine the results so that a more accurate solution can be obtained. The concentration $N_A(t=t_{j+1})$ evaluated in Eq. (3.18) is used as an intial guess to compute a more accurate $N_A(t=t_{j+1})$ by

$$\left.\frac{\partial N_A}{\partial t}\right|_{x_i,t_{j+0.5}} = \frac{1}{2}\left(\left.\frac{\partial}{\partial x}\left(\frac{mD_A}{1-\alpha N_A}\frac{\partial N_A}{\partial x}\right)\right|_{x_i,t_j} + \left.\frac{\partial}{\partial x}\left(\frac{mD_A}{1-\alpha N_A}\frac{\partial N_A}{\partial x}\right)\right|_{x_i,t_{j+1}}\right), \quad (3.19)$$

The finite difference forms of Eq. (3.19) are given by

$$\left.\frac{\partial N_A}{\partial t}\right|_{x_i,t_{j+0.5}} \cong \frac{N_A^1(i,j+1)-N(i,j)}{\Delta t}, \quad (3.20)$$

$$\left.\frac{\partial}{\partial x}\left(\frac{mD_A}{1-\alpha N_A}\frac{\partial N_A}{\partial x}\right)\right|_{x_i,t_j} \cong \frac{mD_A}{(\Delta x)^2}\left(\frac{N_A(i+1,j)-N_A(i,j)}{1-\alpha\left[N_A(i+1,j)+N_A(i,j)\right]/2} - \frac{N_A(i,j)-N_A(i-1,j)}{1-\alpha\left[N_A(i,j)+N_A(i-1,j)\right]/2}\right), \quad (3.21)$$

and

$$\left.\frac{\partial}{\partial x}\left(\frac{mD_A}{1-\alpha N_A}\frac{\partial N_A}{\partial x}\right)\right|_{x_i,t_{j+1}} \cong \frac{mD_A}{(\Delta x)^2}\left(\frac{N_A^o(i+1,j+1)-N_A^o(i,j+1)}{1-\alpha\left[N_A^o(i+1,j+1)+N_A^o(i,j+1)\right]/2} - \frac{N_A^o(i,j+1)-N_A^o(i-1,j+1)}{1-\alpha\left[N_A^o(i,j+1)+N_A^o(i-1,j+1)\right]/2}\right), \quad (3.22)$$

where N_A^o is the guessed concentration at $t=t_{j+1}$ and N_A^1 is the unknown concentration at $t=t_{j+1}$. The procedure is repeated by substituting the calculated N_A^1 into N_A^o in Eq. (3.22) until steady state values of N_A are attained. However, great care must be exercised in

the case of large $r_1 = \frac{mD_A\Delta t}{2(\Delta x)^2}$ which is primarily determined by the time step Δt. As Δt increases, the number of iterations increases and the steady state values of N_A may deviate from the exact values because of the accumulation of the round-off error. The solution may not converge for large r_1 if αN_A is close to one. The steady state values for each time step can be reached more quickly by using a smaller Δt with less iterations, implying that more time steps are required for a fixed diffusion time. The round-off error may also accumulate if many time steps are involved in the calculation.

Figure 3-5 shows the 1-D concentration profiles modeled by an explicit finite difference method with α=0.0, 0.5, 0.8, and 0.9. For the sake of illustration, D_A is assumed to be 0.015 μm^2/min corresponding to that of the Ag^+-Na^+ exchange in BK7 glass at 340°C. As expected, the profile is a complementary error function for α=0. As α increases, the profiles becomes more and more gaussian-like. The slope near the surface (x=0) gets smaller as α becomes larger. Figure 3-6(a) shows a surface plot of a 2-D concentration profile for t=720 min, D_A= 0.0042 μm^2/min, α=0.9 and the mask width W_M=3.5 μm. Figure 3-6(b) shows the contour equi-concentration profile in the transverse dimension. The 1/e width and depth are 7.3 μm and 3.3 μm, respectively. It is obvious that the aspect ratio of the waveguide is larger than two. The ratio determines the waveguide characteristics as will be explained in chapter 5. The 2-D diffusion is performed by allowing the ion exchange to occur via a mask opening in the glass substrate delineated

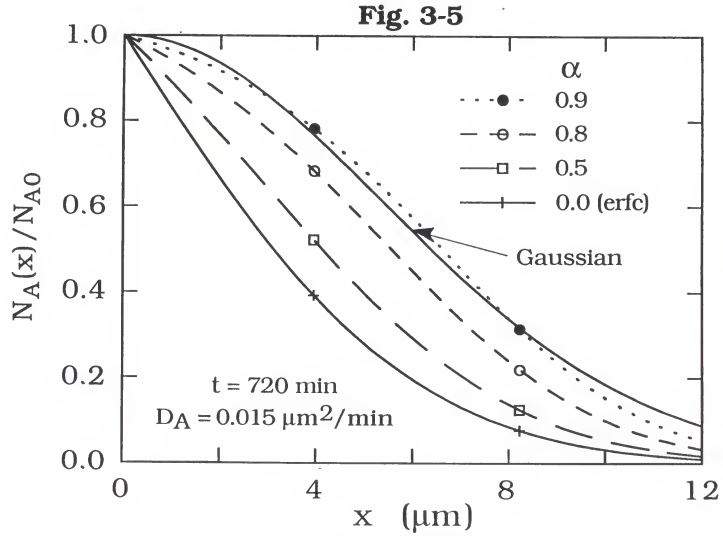

Fig. 3-5 Concentration profile solved by FDM for α = 0.0(erfc), 0.5, 0.8, and 0.9. The diffusion coefficient and time are 0.015 μm^2/min and 720 min, respectively. A Gaussian curve is drawn for comparison with the dotted curve (α=0.9).

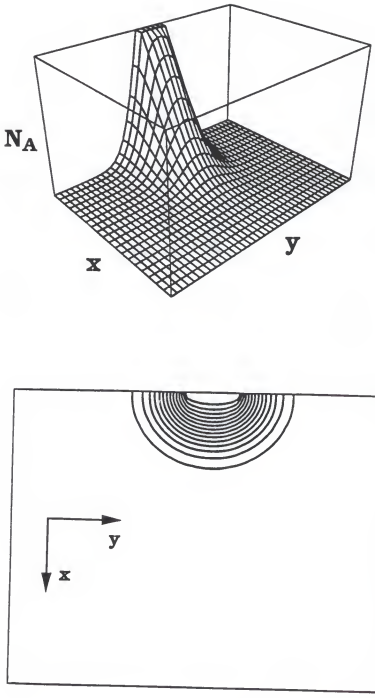

Fig. 3-6. 3-D concentration profiles for t=720 min, D_A=0.0042 μm^2/min, α=0.9, and W_M=3.5 μm. (a) Surface plot. (b) Contour plot.

through a standard photolithographic process described in the next chapter. The mask opening region always has a constant concentration as seen from the surface profile by the flat top. As the mask opening becomes narrower, the width of the flat top decreases and the contour lines are expected to become semicircles. In this case, the aspect ratio of the waveguide becomes two.

3.3. Guided Wave—Helmholtz Equation

It is well known that the optical wave is essentially confined in the transverse directions and guided along the longitudinal direction. The change in the index profile is assumed to be small and proportional to the concentration profile in the case of ion-exchanged waveguides. The index profiles are obtained numerically as described in the last section. The knowledge of the behavior of the guided wave is crucial to the design of optical devices. Two approaches are usually used to solve the modal properties of one-dimensional waveguides: one is geometrical optics and the other is wave optics. The former, *i.e.*, the ray optics, is an approximation that is valid as long as the waveguide dimensions are larger than the wavelength of the light. The latter or the wave optics is always valid and is particularly used to determine the modal field distribution; nevertheless, it is more complicated than the ray optics. Since the concentration profile of the dopant ions is continuously changed from maximum to zero, the index in the waveguide region is inhomogeneous and graded. Hence, we will focus on the graded-index waveguide and emphasize the field distribution of the guided waves. However, the WKB method, which adopts the ray approach, will be discussed briefly in this chapter since the method is

useful in the characterization of the mode indices of the planar multimode waveguide.

3.3.1. Vector and Scalar Helmholtz Equation

The wave propagation in a source-free, linear dielectric medium is governed by the vector Helmholtz (or the wave) equations. Assuming a z-propagating wave with time- and z-dependence expressed as $\exp(j\omega t - j\beta z)$ and ε, μ_o and β independent of z, the wave equations become [Koge88]

$$\nabla_t^2\vec{E_t} + \nabla_t\left(\vec{E_t}\cdot\nabla_t \ln\varepsilon\right) + \left(\omega^2\varepsilon\mu_o - \beta^2\right)\vec{E_t} = \vec{0}\,, \tag{3.23}$$

and

$$\nabla_t^2\vec{H_t} + \left(\nabla_t \ln\varepsilon\right)\times\left(\nabla_t\times\vec{H_t}\right) + \left(\omega^2\varepsilon\mu_o - \beta^2\right)\vec{H_t} = \vec{0}\,, \tag{3.24}$$

where $\vec{E_t}$ and $\vec{H_t}$ are the transverse components of the electric and magnetic fields of the waveguide modes, respectively, and depend on the transverse coordinates only; ω is the angular frequency; ε and μ_o are the scalar permittivity and the permeability of the medium, and β is the propagation constant. The transverse Laplacian is defined as $\nabla_t^2 \equiv \frac{\partial^2}{\partial x^2} + \frac{\partial^2}{\partial y^2}$. Note that $\vec{E_t}$ and $\vec{H_t}$ are independent of time and z. The corresponding z-components of the fields are, derived from $\nabla\cdot\vec{H} = 0$ and $\nabla\cdot(\varepsilon\vec{E}) = 0$ and given, in terms of the transverse components, as follows:

$$j\beta E_z = \nabla_t\cdot\vec{E_t} + \vec{E_t}\cdot\nabla_t \ln\varepsilon \tag{3.25}$$

and

$$j\beta H_z = \nabla_t\cdot\vec{H_t}\,. \tag{3.26}$$

Similarly, E_z and H_z are independent of time and z.

For a slowly varying index medium, $\nabla_t \ln \varepsilon$ is approximately equal to zero and the gradient terms (second term) in the Eq. (3.23) and Eq. (3.24) can be ignored. The above four equations are rewritten as

$$\nabla_t^2 \vec{E_t} + \left(\omega^2 \varepsilon \mu_o - \beta^2\right) \vec{E_t} = \vec{0}\,, \tag{3.27}$$

$$\nabla_t^2 \vec{H_t} + \left(\omega^2 \varepsilon \mu_o - \beta^2\right) \vec{H_t} = \vec{0}\,, \tag{3.28}$$

$$j\beta E_z = \nabla_t \cdot \vec{E_t}\,, \tag{3.29}$$

and

$$j\beta H_z = \nabla_t \cdot \vec{H_t}\,. \tag{3.30}$$

In principle, we only need to solve the above equations for either $\vec{E_t}$ or $\vec{H_t}$. The other field vector can be calculated by using Maxwell's curl equations

$$\nabla \times \vec{E} = -j\omega\mu_o \vec{H} \tag{3.31}$$

and

$$\nabla \times \vec{H} = j\omega\varepsilon \vec{E}\,. \tag{3.32}$$

The transverse components in x and y directions are easily decoupled using separation of variables. As a result, Eq. (3.27) and Eq. (3.28) become

$$\begin{cases} \nabla_t^2 E_x + \left(\omega^2 \varepsilon \mu_o - \beta^2\right) E_x = 0 \\ \nabla_t^2 E_y + \left(\omega^2 \varepsilon \mu_o - \beta^2\right) E_y = 0 \end{cases} \tag{3.33}$$

$$\begin{cases} \nabla_t^2 H_x + \left(\omega^2 \varepsilon \mu_o - \beta^2\right) H_x = 0 \\ \nabla_t^2 H_y + \left(\omega^2 \varepsilon \mu_o - \beta^2\right) H_y = 0\,. \end{cases} \tag{3.34}$$

For a two-dimensional surface waveguide, with the y-direction parallel to the surface of the substrate E_x/E_y is close to, but not equal to, zero

for the quasi-TE modes and similarly, H_x/H_y is nearly equal to zero for the quasi-TM modes. Thus, the scalar Helmholtz equation is expressed as

$$\nabla_t^2 F + \left(\omega^2 \varepsilon \mu_o - \beta^2\right) F = 0 , \tag{3.35}$$

where F represents E_y for the quasi-TE mode or H_y for the quasi-TM mode. In the above equation, F and ε are functions of x and y and ε is assumed to be a slowly varying function of x and y. By substituting $\nabla_t^2 = \frac{\partial^2}{\partial x^2} + \frac{\partial^2}{\partial y^2}$, the scalar Helmholtz equation becomes

$$\frac{\partial^2 F}{\partial x^2} + \frac{\partial^2 F}{\partial y^2} + k_o^2(n^2 - N^2)F = 0 , \tag{3.36}$$

where n is the index of refraction; the mode or the effective index $N \equiv \beta/k_o$ and $k_o^2 = \omega^2 \varepsilon_o \mu_o$. In the case of one-dimensional waveguide, the above equation can be further simplified as

$$\frac{d^2 F}{dx^2} + k_o^2(n^2 - N^2)F = 0 . \tag{3.37}$$

In the following sections, numerical methods will be presented to solve Eq. (3.36) for 2-D waveguides and Eq. (3.37) for 1-D waveguides.

3.3.2. One-Dimensional Waveguides

One-dimensional (planar) waveguides are assumed to confine the energy in the x-direction. The study of multimoded, planar waveguides helps us characterize the index profile and correlate it to the diffusion profile. Knowledge of the index profile is essential to the design and fabrication of the waveguides.

WKB Method

The well-known WKB method, used to obtain approximate solutions of the Schrödinger equation, can be applied to Eq. (3.37) to solve for the modes in a multimode waveguide with slowly varying index profile n(x). Once the mode indices (N) in the wave equation are solved, Eq. (3.37) becomes an ordinary differential equation and the fields can be obtained by solving the equation using a numerical technique, such as the Runge-Kutta method.

According to the WKB method, the characteristic equation for the m^{th}-order mode is given by [Gord66]

$$2k_o \int_0^{x_m} [n^2(x)-N_m^2]^{1/2} dx - 2\phi_b - 2\phi_c = 2m\pi, \qquad (3.38)$$

where x_m is the turning point for the m^{th} mode; $-2\phi_b$ and $-2\phi_c$ are the phase shifts at the turning point and at the cover-guide interface. It is assumed that the waveguide is a graded-index waveguide with its cover-guide interface at x=0. In the ray picture (Fig. 3-7), the left hand side of Eq. (3.38) represents the total transverse phase shift the ray suffers in one round trip across the guide. This must equal $2m\pi$ to achieve constructive interference. At the turning point x_m, the ray reverses its direction and travels back to the surface of the waveguide; the index at that point equals the mode index, *i.e.*,

$$N_m = n(x_m) . \qquad (3.39)$$

Figure 3-7 shows the graded-index profile of the waveguide on the left

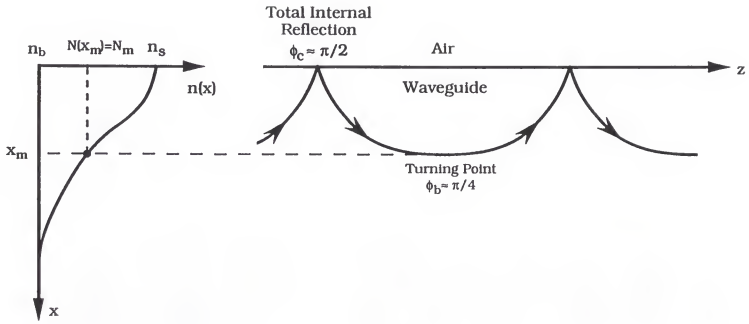

Fig. 3-7. Ray diagram for the graded-index waveguides. The index profile is shown on the left. The notations are defined in the text.

and the curved path traversed by the ray in the waveguide on the right. At the cover-guide interface, again it is reflected back due to total internal reflection. The phase shift ϕ_c at the cover -glass interface equals

$$\phi_c = \tan^{-1}\left(r\sqrt{\frac{N_m^2-n_c^2}{n_s^2-N_m^2}}\right), \qquad (3.40)$$

where n_c and n_s are the cover index and the surface index, respectively, and r=1 for the TE mode and $r = n_s^2/n_c^2 > 1$ for the TM mode. ϕ_c for the TM mode is always larger than that for the TE mode. If the mode index N_m is close to n_s, then $\phi_c \cong \pi/2$. In the case of highly asymmetrical waveguides, *i.e.*, $n_b-n_c >> n_s-n_b$, ϕ_c is also approximately equal to $\pi/2$, where n_b is the substrate index. ϕ_b approximately equals $\pi/4$ [Gord66] as the ray approaches grazing incidence at $x = x_m$ with the index approaching the mode index. However, this approximation may give erroneous results for the modes close to cutoff [Sriv87a]. Since N_m is the only unknown, Eq. (3.38) can be solved numerically for a given index profile. The accuracy of the this method depends on how accurate we can estimate the phase shifts ϕ_c and ϕ_b if no approximation is used. For the three-layer slab, step-index waveguides, the approximations of $\phi_b \cong \pi/4$ and $\phi_c \cong \pi/2$ are not accurate enough and the exact expressions for the phase shifts must be used. Thus, Eq. (3.38) becomes

$$2k_oW\sqrt{n_s^2-N_m^2} - 2\phi_b - 2\phi_c = 2m\pi, \qquad (3.41)$$

where W is the width of the waveguide; ϕ_c is expressed in Eq. (3.40) and ϕ_b is obtained by substituting ϕ_b and n_b with ϕ_c and n_c in Eq.

(3.40), respectively. No analytical solutions for the above equation are available. However, Eq. (3.41) can be normalized [Koge74] as

$$V\sqrt{1-b} = m\pi + \phi_b + \phi_c \,, \qquad (3.42)$$

where the normalized frequency $V \equiv k_o W\sqrt{n_s^2-n_b^2}$; the normalized mode index $b \equiv \frac{N_m^2-n_b^2}{n_s^2-n_b^2}$; $\phi_b = \tan^{-1}(1+q_M)\sqrt{\frac{b}{1-b}}$; $\phi_c = \tan^{-1}(\frac{1+q_M}{1-a\,q_M})\sqrt{\frac{a+b}{1-b}}$; the asymmetry $a \equiv \frac{n_b^2-n_c^2}{n_s^2-n_b^2}$ and $q_M = 0$ for the TE mode and $q_M = \frac{n_s^2}{n_b^2}$ -1 for the TM mode. The asymmetry a is zero for the symmetrical waveguides ($n_b = n_c$). In general, a is large for air-covered and/or small-index-change guides. Figure 3-8 shows b versus V for the TE modes for a=0, 1, 10, and ∞. The normalized mode index b is zero for the mode close to cutoff and ϕ_b is also zero. b approaches unity for the well-confined mode and both ϕ_b and ϕ_c are near $\pi/2$. There is no cutoff for the fundamental mode (m=0) in the case of a=0. The mode index N_m of the TE mode is always larger than that of the TM mode with the same mode number m in the case of an isotropic medium. However, the mode indices are the identical for the TE modes and the TM modes in the case $n_s \rightarrow n_b$ and $n_c \neq n_b$ since q_M approaches zero for the TM modes.

Matrix Method

Equation (3.42) can be used to obtain the mode index of a three-layer slab waveguide which has the simplest structure: the substrate, film and cover layers. In this subsection we consider multilayer slab waveguides which can be 5-layer directional couplers or discretized

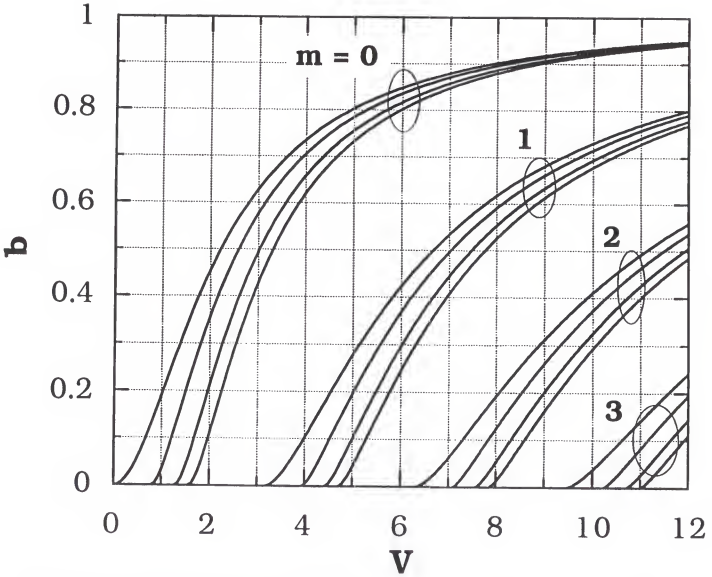

Fig. 3-8. The normalized mode index (b) versus the normalized frequency (V) characteristics of 3-layer step-index waveguides for mode m = 0, 1, 2, and 3. The asymmetry factors are 0, 1, 10, and ∞, respectively, from left to right for each mode.

graded-index waveguides. 2X2 matrix method will be employed here to solve the mode indices as well as the mode fields of a multilayer waveguide. This method can be used to solve not only the multilayer waveguides but also the multilayer transmission and reflection problems.

For the TE modes of a planer waveguide, the components E_z, E_x, and H_y are zero. The coordinate system is defined in Fig. 3-9 which shows a sketch of a multilayer waveguide, where superscripts '+' and '-' represent the positive and negative traveling wave, respectively; E_i and n_i are the amplitudes of the field and the index in layer i. d_2, d_3,... are the thicknesses associated with layer 2, 3,.... In this case, Eq. (3.37) becomes

$$\frac{d^2E_y}{dx^2} + k_0^2(n^2(x)-N^2)E_y = 0 . \qquad (3.43)$$

E_y is the transverse electric field. The H fields, in terms of E_y, are given by

$$H_x = -\frac{\beta}{\omega\mu_o} E_y , \qquad (3.44)$$

and

$$H_z = \frac{j}{\omega\mu_o}\frac{dE_y}{dx} , \qquad (3.45)$$

where β is the propagation constant. The solution of E_y in layer i can be expressed as

$$E_y(\text{layer i}) = E_i^{+} e^{-jk_ix} + E_i^{-} e^{jk_ix}, \qquad (3.46)$$

$$d'_{i-1} < x \le d'_i \equiv \sum_{m=2}^{i} d_m$$

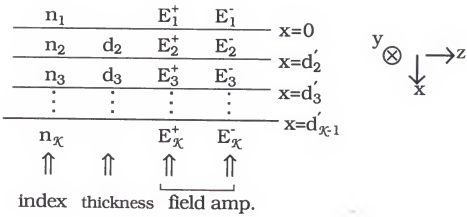

Fig. 3-9 Multilayer structure of waveguide.

where k_l is defined as $k_0\sqrt{n_l^2-N^2}$. The first term of RHS of the above equation is a positive-x propagating wave and the second term is a negative-x wave. The solutions of Eq. (3.43) are oscillating fields for $n_l > N$. On the other hand, the solutions become exponential functions for $n_l < N$ and imaginary k_l. The boundary conditions require that the tangential components E_y and H_z (or $\frac{dE_y}{dx}$ in Eq. (3.45)) be continuous at the interface of each layer. Therefore, at the $(i-1)^{th}$ interface the field must be

$$\begin{aligned} E_y(x=d_{i-1}') &= E_{i-1}^+ e^{-jk_{i-1}d_{i-1}'} + E_{i-1}^- e^{jk_{i-1}d_{i-1}'} \\ &= E_i^+ e^{-jk_i d_{i-1}'} + E_i^- e^{jk_i d_{i-1}'} \end{aligned} \qquad (3.47)$$

$$-\omega\mu_o H_z(x=d'_{i-1}) = -k_{i-1}E^+_{i-1}\,e^{-jk_{i-1}d'_{i-1}} + k_{i-1}E^-_{i-1}\,e^{jk_{i-1}d'_{i-1}}$$
$$= -k_i E^+_i\,e^{-jk_i d'_{i-1}} + k_i E^-_i\,e^{jk_i d'_{i-1}} \quad . \qquad (3.48)$$

From Eqs. (3.47) and (3.48), we can obtain

$$\begin{pmatrix} E^+_{i-1} \\ E^-_{i-1} \end{pmatrix} = M_1 \begin{pmatrix} E^+_i \\ E^-_i \end{pmatrix}, \qquad (3.49)$$

where

$$M_1 = \frac{1}{2}\begin{pmatrix} \left(1+\frac{k_i}{k_{i-1}}\right)e^{j(k_{i-1}-k_i)d'_{i-1}} & \left(1-\frac{k_i}{k_{i-1}}\right)e^{j(k_{i-1}+k_i)d'_{i-1}} \\ \left(1-\frac{k_i}{k_{i-1}}\right)e^{-j(k_{i-1}+k_i)d'_{i-1}} & \left(1+\frac{k_i}{k_{i-1}}\right)e^{-j(k_{i-1}-k_i)d'_{i-1}} \end{pmatrix}. \qquad (3.50)$$

For a structure consisting of $\mathcal{K}$ layers,

$$\begin{pmatrix} E^+_1 \\ E^-_1 \end{pmatrix} = M_2 \begin{pmatrix} E^+_2 \\ E^-_2 \end{pmatrix} = M_2\, M_3 \begin{pmatrix} E^+_3 \\ E^-_3 \end{pmatrix}$$
$$= M_2\, M_3 \cdots M_{\mathcal{K}} \begin{pmatrix} E^+_{\mathcal{K}} \\ E^-_{\mathcal{K}} \end{pmatrix} = M \begin{pmatrix} E^+_{\mathcal{K}} \\ E^-_{\mathcal{K}} \end{pmatrix}. \qquad (3.51)$$

A 2x2 matrix M correlates the fields between the first layer and the last layer. The matrix is determined by the parameters of the waveguide, *i.e.*, the indices and the thickness, and independent of the fields. In the case of the waveguide problem, the fields must be confined in the guiding layers and exponentially decaying in the outer layers. Therefore, the amplitudes E_1^- and $E_{\mathcal{K}}^+$ are zero. To solve for the mode index, an arbitrary value of $E_{\mathcal{K}}^-$ is substituted into Eq. (3.51). E_1^+ and E_1^- can be evaluated by choosing different trial mode indices until E_1^- is zero for a trial mode index. The trial value is one of the mode indices of the waveguides. The mode field is obtained by substituting all the calculated amplitudes E_1,..., $E_{\mathcal{K}}$ into Eq. (3.46). The matrix method is also useful for solving for the fields of the radiation modes.

In the case of complex-index systems, *i.e.*, lossy or gain media, the method is applicable as well. However, the mode index may also be a complex number in this case.

For the TM modes, the components H_z, H_x, and E_y are zero. The scalar Helmholtz equation becomes

$$\frac{d^2H_y}{dx^2} + k_0^2(n^2(x)-N^2)H_y = 0 \tag{3.52}$$

and the E fields are given by

$$E_x = \frac{\beta}{\omega\varepsilon} H_y \tag{3.53}$$

and

$$E_z = -\frac{j}{\omega\varepsilon}\frac{dH_y}{dx}. \tag{3.54}$$

Similar expression for the adjacent H fields can be obtained

$$\begin{pmatrix} H_{i-1}^{+} \\ H_{i-1}^{-} \end{pmatrix} = M_i \begin{pmatrix} H_i^{+} \\ H_i^{-} \end{pmatrix}, \tag{3.55}$$

where

$$M_i = \frac{1}{2}\begin{pmatrix} \left(1+\frac{n_{i-1}^2 k_i}{n_i^2 k_{i-1}}\right) e^{j(k_{i-1}-k_i)d_{i-1}'} & \left(1-\frac{n_{i-1}^2 k_i}{n_i^2 k_{i-1}}\right) e^{j(k_{i-1}+k_i)d_{i-1}'} \\ \left(1-\frac{n_{i-1}^2 k_i}{n_i^2 k_{i-1}}\right) e^{-j(k_{i-1}+k_i)d_{i-1}'} & \left(1+\frac{n_{i-1}^2 k_i}{n_i^2 k_{i-1}}\right) e^{-j(k_{i-1}-k_i)d_{i-1}'} \end{pmatrix}. \tag{3.56}$$

Since the tangential components H_y and E_z are continuous, according to Eq. (3.54), $\frac{1}{n^2}\frac{dH_y}{dx}$ is continuous. As a result, the slope of H_y is not continuous if the index is discontinuous.

The matrix method is usually more accurate than the WKB method for the TE modes as well as for the TM modes. The mode

fields are easily obtained by the matrix method. This method is applicable to both the step-index and the graded-index waveguides if the step indices are used to approximate the discretized graded-index profile. As mentioned earlier, it can be used to solve for the modes in complex-index or lossy waveguides. However, this method may need more CPU time.

Finite Difference Method

As described earlier, the nonlinear diffusion equation can be converted into a finite difference form and solved by iterations. Similarly, the scalar Helmholtz equation can be converted into a finite difference expression. However, the Helmholtz equation involves the following unknowns: the propagation constant or the mode index as well as the mode field as shown in Eq. (3.37). The mode indices have discrete values and each of them corresponds to a mode field. In this subsection, the application of the finite difference formula to the Helmholtz equation will be described and compared to the methods mentioned in the last subsection.

Let us consider the first term in Eq. (3.37), *i.e.*, d^2F/dx^2, which can be represented in the form of Eq. (3.8). By rewriting Eq. (3.37), one can obtain the expression at $x=x_i$:

$$\frac{F(i+1)-2F(i)+F(i-1)}{(\Delta x)^2} + k_0^2(n^2(i)-N^2)F(i) = 0 \qquad (3.57)$$

or

$$\frac{1}{v^2} F_{i-1} + \left(f_i - \frac{2}{v^2}\right) F_i + \frac{1}{v^2} F_{i+1} = b\, F_i\,, \qquad (3.58)$$

where the field $F_i=F(i)=F(x=x_i)$; $v^2\equiv k_o^2(n_s^2-n_b^2)(\Delta x)^2$; $f_i\equiv\frac{n_i^2-n_b^2}{n_s^2-n_b^2}$; the index $n_i=n(i)=n(x=x_i)$ and $b\equiv\frac{N^2-n_b^2}{n_s^2-n_b^2}$. n_s, n_b and b, as defined earlier, are the maximum index, the substrate index and the normalized mode index, respectively. It is known that the guided field is zero away from the waveguide region. Therefore, it is reasonable to assume that $F_0=0$ and $F_{\mathcal{K}+1}=0$ at the calculation boundaries, as shown in Fig. 3-10, where $\mathcal{K}$ is the number of the discretized points of the field. For i=1 to $\mathcal{K}$, Eq. (3.58) can be expressed as

$$\begin{bmatrix} d_1 & s & & & 0 \\ s & d_2 & \cdot & & \\ & \cdot & \cdot & \cdot & \\ & & \cdot & \cdot & s \\ 0 & & & s & d_{\mathcal{K}} \end{bmatrix} \begin{bmatrix} F_1 \\ F_2 \\ \cdot \\ \cdot \\ F_{\mathcal{K}} \end{bmatrix} = b \begin{bmatrix} F_1 \\ F_2 \\ \cdot \\ \cdot \\ F_{\mathcal{K}} \end{bmatrix}, \qquad (3.59)$$

where $s\equiv\frac{1}{v^2}$ and $d_i\equiv f_i-\frac{2}{v^2}$. For the nontrivial solutions of the field, the normalized mode index b must be an eigenvalue of the $\mathcal{K}x\mathcal{K}$ tri-diagonal matrix which is shown in Eq. (3.59). The eigenvectors of this matrix are the mode fields of the waveguide. The eigenvalues and vectors can be solved by commercially available subroutines *e.g.*, IMSL. All the positive eigenvalues are the b values of the guided modes and the maximum eigenvalue and eigenvector correspond to the b value and the field of the fundamental mode, respectively.

The finite difference method can yield all the mode indices as well as the mode fields. Since we assume that the fields vanish at the calculation boundaries, only the guided modes can be solved by this

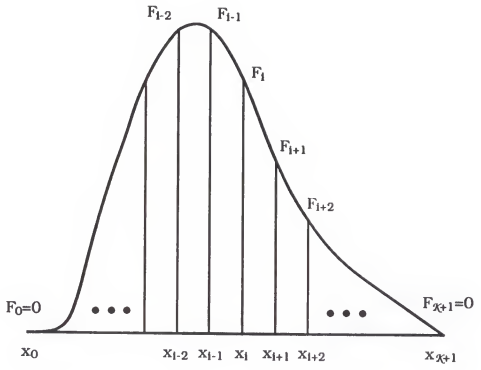

Fig. 3-10. 1-D field profile with the assumption F_0 and $F_{\chi+1}=0$ using in FDM.

method. Attention must be given to calculation of the modes close to cutoff, where the fields may extend away from the guided region. In this case, more points and larger calculation boundaries must be taken. Compared to the matrix method, this method can not solve the TE and TM modes without modifications of Eq. (3.59). For the step-index waveguides with a couple of layers, the number of points can not be reduced as in the case solved by the matrix method. However, for the graded-index waveguides with real indices, the finite difference method can give quick results for all the modes. The implementation of the computer program for the finite difference method is quite easy as long as the scientific subroutine package is accessible. The application of this method to the two-dimensional problems is somewhat straightforward compared to the WKB and matrix methods as will be explained in the next section.

3.3.2. Two-Dimensional Numerical Method

Most guided-wave optical devices consist of two-dimensional channel waveguides. Only a few special 2-D index profiles have explicit analytic solutions, *e.g.*, step-index and parabolic-index circular optical fibers [Marc79]. Thus, numerical methods are very important for an understanding of 2-D guided-wave behavior in rectangular geometry.

Two methods are introduced in this section. The first is the effective index method and the second is the finite difference method. Again, the emphasis is put on the scalar Helmholtz equation for the two-dimensional case, *i.e.*, Eq. (3.36).

Effective Index Method

The effective index method [Rama74, Hock77, Chia86, Veld88] is popular and easy to implement for the 2-D channel waveguides. This method is mainly used to calculate the mode indices of the waveguides. By converting a 2-D index profile into its 1-D equivalent profiles, the mode index can easily be evaluated since the numerical methods for the 1-D planar waveguides are available as discussed in the last section. In general, solving the 1-D equivalent index profiles is much easier than solving the 2-D index profile directly.

The method is briefly described below [Veld88]. First, we consider the scalar Helmholtz equation, Eq. (3.36). Assume that the modal field F(x,y) can be written as

$$F(x,y) = F_1(x,y)\, F_2(y)\,, \tag{3.60}$$

where $F_1(x,y)$ is a slowly varying function of y so that

$$\frac{\partial^2 F(x,y)}{\partial y^2} = \frac{\partial^2}{\partial y^2}\left(F_1(x,y)F_2(y)\right) \equiv F_1(x,y)\,\frac{\partial^2 F_2(y)}{\partial y^2}\,. \tag{3.61}$$

An effective index profile $n_{eff}(y)$ is defined to satisfy

$$\frac{\partial^2 F_1}{\partial x^2} + k_0^2\left[n^2(x,y) - n_{eff}^2(y)\right]F_1 = 0\,. \tag{3.62}$$

As shown in Fig. 3-11, the channel waveguide is sliced vertically in the depth direction normal to the surface of the sample with either uniform or nonuniform slice thickness. The thickness of the slice should be small enough to accommodate index variations. The thickness can be judicially chosen with its value increasing

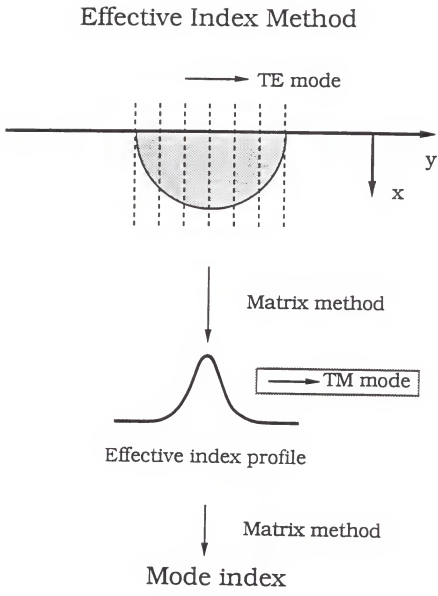

Fig. 3-11. The procedure in the effective index method for evaluating the mode index of 2-D waveguides.

monotonically with the distance between the slice and the center of the waveguide. Since there is no sharp boundary in the y-direction for the ion-exchanged channels, the location of the slices is not that critical. The nonuniform spacing approach uses less memory and aids in saving computer CPU time. Each sliced layer has its own mode index $n_{eff}(y)$ and modal field $F_1(x,y)$. $n_{eff}(y)$ is evaluated for each layer by assuming that, within the layer, the index is invariant in the y-direction and, hence, only a 1-D index profile is considered in solving Eq. (3.62). To solve for the mode index of each slice in Eq. (3.62), we utilize the 1-D matrix method in which only a 2X2 matrix is involved. Hence, the 1-D matrix method is suitable for a memory-limited calculation environment, *e.g.*, a personal computer. Once the effective index profile $n_{eff}(y)$ is solved, by substituting Eqs. (3.60), (3.61), and (3.62) into Eq. (3.36), the 2-D Helmholtz equation is reduced to a 1-D Helmholtz equation:

$$\frac{\partial^2 F_2}{\partial y^2} + k_0^2\left[n_{eff}^2(y) - N^2\right] F_2 = 0 \,. \qquad (3.63)$$

Thus, the mode index N of a 2-D index profile can be solved by solving the equivalent, 1-D graded-index profile, namely, $n_{eff}(y)$ by again using the 1-D matrix method. Although the effective index method is suitable for the fundamental mode since its use is restricted by the assumption of a slowly varying field $F_1(x,y)$ in the derivation of the algorithm, we have verified its validity for both the fundamental mode of channel waveguides and the first two normal modes of the weakly coupled directional couplers. Nevertheless, the effective index approach is known to fail near the cutoff [Chia86].

A quasi-TE mode of a channel waveguide has its polarization parallel to the surface of the guide (y-direction). Therefore, in this case, F_1 in Eq. (3.62) represents the transverse E field. However, in order to maintain the polarization in the same direction, a TM mode is used in the solution of Eq. (3.63), where F_2 is assumed to represent the transverse H field. On the other hand, if we had considered instead, the TM mode in Eq. (3.62), F_2 in Eq. (3.63) would now represent the transverse E field corresponding to the TE mode in the equivalent, planar, graded-index waveguide in the y-direction. Our numerical results (presented later in chapter 6) indicate that there is little difference in the TE and the TM mode indices due to the asymmetry of the channel waveguide between the TE and the TM modes.

Finite Difference Method

The 1-D finite difference method can be extended to the 2-D finite difference method by defining mesh points similar to those shown in Fig. 3-4. In this case, Eq. (3.59) for 1-D waveguides becomes

$$A_{x_s x_f \times x_s x_f} F_{x_s x_f \times 1} = b F_{x_s x_f \times 1} , \qquad (3.64)$$

where A is a block tri-diagonal symmetrical matrix and equals

$$A_{\mathcal{K}_x\mathcal{K}_y\times\mathcal{K}_x\mathcal{K}_y} = \left[\begin{array}{cccc} \overbrace{\mathcal{D}_1 & \mathcal{S}_2 & & 0}^{\mathcal{K}_y \text{ blocks}} \\ \mathcal{S}_2 & \mathcal{D}_2 & \ddots & \\ & \ddots & \ddots & \ddots \\ & & \ddots & \ddots & \mathcal{S}_2 \\ 0 & & & \mathcal{S}_2 & \mathcal{D}_{\mathcal{K}_y} \end{array}\right], \quad \mathcal{D}_1 \text{ and } \mathcal{S}_2 \text{ are matrices,}$$

$$\mathcal{D}_{1\ \mathcal{K}_x\times\mathcal{K}_x} = \left[\begin{array}{cccc} d_{(1-1)\mathcal{K}_x+1} & s_1 & & 0 \\ s_1 & d_{(1-1)\mathcal{K}_x+2} & \ddots & \\ & \ddots & \ddots & s_1 \\ 0 & & s_1 & d_{(1-1)\mathcal{K}_x+\mathcal{K}_x} \end{array}\right], \quad \mathcal{S}_{2\ \mathcal{K}_x\times\mathcal{K}_x} = \left[\begin{array}{ccc} s_2 & & 0 \\ & s_2 & \\ & \ddots & \\ 0 & & s_2 \end{array}\right],$$

$$F_{\mathcal{K}_x\mathcal{K}_y\times 1} = \left[\begin{array}{c} F_1 \\ F_2 \\ \vdots \\ F_{\mathcal{K}_x\mathcal{K}_y} \end{array}\right], \quad \text{and } d_i = f_i - \frac{2}{v^2}\left(1+\frac{1}{r^2}\right),\ r=\frac{\Delta y}{\Delta x},\ s_1=\frac{1}{v^2},\ s_2=\frac{1}{v^2 r^2}.$$ The

boundaries have been assumed to be zero. Since the matrix A is band symmetrical, we do not need to solve for all the eigen-solutions because commercial subroutines are available to obtain a couple of largest eigen-values and vectors, which are associated to the lower order modes. Thus, less CPU time and memory are needed. Even though the CPU time is reduced by using a symmetrical matrix, it still takes about 200 seconds CPU time in the IBM 3090-600J computer with vector processors for $\mathcal{K}_x=\mathcal{K}_y=51$, which produces a 2600 by 2600 matrix. If nonuniform mesh sizes are used in the 2-D finite difference method, the CPU time may become an order of magnitude larger and actual run time may be much longer due to the lower priority of the job.

Compared to the effective index method, the 2-D finite difference method is more accurate as long as enough points are taken, which may result in the need for a supercomputer. The algorithm described above does not distinguish betwwen the polarizations of the modes. Therefore, it is not suitable to simulate devices which are birefringent. If the mode is close to cutoff, the calculation boundaries and the number of points must be increased to maintain the same accuracy.

3.4. Propagating Wave—Beam Propagation Method

The beam propagation method (BPM) is a powerful tool for dealing with the propagation of optical beam through a medium with a small index variation. This method, developed by Fleck *et al* [Flec76] in 1976, has found wide applications to the simulation of optical guided-wave devices, *e.g.*, fibers [Feit78, Feit79, Feit80], tapered waveguides [Baet82], Y-branches [Baet82], directional coupler [Feit83], cross couplers [Neye85], modulators [Dani84], nonlinear directional couplers [Thyl86], grating devices [Yevi82] and lasers [Yevi86, Kacz88, Fede89]. With only a few assumptions [Vanr81], BPM shows its flexibility and precision in modeling almost all kinds of propagation problems. The accuracy of BPM has been demonstrated by simulating the propagation of an eigenmode in a straight waveguide. Furthermore, it is not necessary to solve for the mode field or the mode index of the waveguide in the evolution of a guided-wave by BPM. However, this method provides numerical results, not analytical solutions. On the other hand, in some devices, *e.g.*, the directional couplers, the

coupled-mode theory (CMT) [Mill54, Yari73] may give analytical expressions to predict the device characteristics. But the accuracy of the prediction depends on the validity of some assumptions such as the weak coupling in the coupled-mode theory, it is not applicable to strongly coupled waveguides. Device simulation can also be done by evaluating the local normal mode coupling at several steps along the longitudinal direction [Burn88a, Burn88b, Burn89]. The disadvantage of this method is the need to calculate the normal mode fields at each step.

This section will present the theory of BPM, the numerical implementation and its application to a 3-dB asymmetrical cross coupler. Emphasis will be placed on the propagation in 2-D structures (y and z directions) although most of the integrated optical devices are 3-D in nature. The equivalent index profiles can be obtained by slicing the 3-D index profile along the z-direction, assuming that each slice is z-invariant and converting the 2-D (x and y directions) index profile of each slice into a 1-D (y direction only) effective index profile by the effective index method. The implementation of BPM is quite easy. However, due to the limitations of the method, care must be taken in the calculation in some cases, which will be mentioned in this section.

3.4.1. BPM Formulation

Beam propagation method is one of the wave-optics approaches for the analysis of the propagation of the beam in a graded-index medium. 3-D as well as 2-D simulation can be be performed by BPM. Recently many simulations have been done by BPM because of its

power. Several modified BPM's [Nyma89, Yevi89a, Yevi89b, Yevi89c, Yevi90a, Yevi90b] were proposed over the last two years. However, since less assumptions have been made for the standard BPM, only the standard one illustrated by Okoshi [Okos85] will be discussed here.

Considering the vector Helmholtz equation including the longitudinal components E_z and H_z, Eqs. (3.23) and (3.24) can be rewritten as

$$\nabla^2\vec{E} + \nabla\left(\vec{E}\cdot\nabla\ln\varepsilon\right) + \omega^2\varepsilon\mu_o\,\vec{E} = \vec{0} \tag{3.65}$$

$$\nabla^2\vec{H} + \left(\nabla\ln\varepsilon\right)\times\left(\nabla\times\vec{H}\right) + \omega^2\varepsilon\mu_o\,\vec{H} = \vec{0}\,, \tag{3.66}$$

Again with the assumption of a slowly varying index profile, $\nabla\ln\varepsilon \cong 0$, the index gradient terms of Eqs. (3.65) and (3.66) can be neglected. One then obtains

$$\nabla^2\vec{E} + k_o^2 n^2\,\vec{E} = \vec{0} \tag{3.67}$$

$$\nabla^2\vec{H} + k_o^2 n^2\,\vec{H} = \vec{0}\,, \tag{3.68}$$

where n is a function of x, y, and z; k_o is the wave number in vacuum. Let $\tilde{F}$ represent the E or H fields for the quasi-TE or quasi-TM modes, respectively. The wave equation becomes

$$\frac{\partial^2\tilde{F}}{\partial z^2} = -\left(\nabla_\perp^2 + k_o^2 n^2\right)\tilde{F} \equiv -\mathcal{A}\tilde{F}, \tag{3.69}$$

where $\nabla_\perp^2$ is the transverse Laplacian $\frac{\partial^2}{\partial x^2}+\frac{\partial^2}{\partial y^2}$ and $\mathcal{A}$ is an operator. The above equation has the solution at $z=\Delta z$ in terms of the field at $z=0$ as

$$\tilde{F}(x,y,\Delta z) = \exp(\pm j\mathcal{A}\,\Delta z)\,\tilde{F}(x,y,0)$$
$$= \exp(-j\mathcal{A}\Delta z)\,\tilde{F}(x,y,0), \qquad (3.70)$$

where the plus sign for the reflected wave is neglected. The operator $\mathcal{A}^{1/2}$ can be decomposed into three terms:

$$\mathcal{A}^{1/2} = (\nabla_\perp^2 + k_o^2 n^2)^{1/2}$$
$$= \frac{\nabla_\perp^2}{(\nabla_\perp^2 + k_o^2 n^2)^{1/2} + k_o n} + k_o n$$
$$= \frac{\nabla_\perp^2}{(\nabla_\perp^2 + k_o^2 n^2)^{1/2} + k_o n_o} + k_o n_o + k_o n_o\left(\frac{n}{n_o} - 1\right), \qquad (3.71)$$

where n_o is a reference index, independent of position. n_o is typically set equal to the substrate index or the approximate mode index in the waveguide. It is also assumed that the position-dependent index n in the first term of RHS of Eq. (3.71) is equal to n_o. Therefore, the operator $\mathcal{A}^{1/2}$ is expressed as the summation of the propagation in the homogeneous medium with index n_o and a position-dependent phase correction term $\chi(x,y,z)$:

$$\mathcal{A}^{1/2} = \frac{\nabla_\perp^2}{(\nabla_\perp^2 + k_o^2 n_o^2)^{1/2} + k_o n_o} + k_o n_o + k_o n_o\left(\frac{n}{n_o} - 1\right), \qquad (3.72)$$

where $\chi(x,y,z) = k_o n_o\left(\frac{n}{n_o} - 1\right)$ and $\left|\frac{n-n_o}{n_o}\right| << 1$. The phase of $\tilde{F}$ can be approximated to be $\exp(-jk_o n_o z)$ since we assume $n \cong n_o$. Thus, the field $\tilde{F}$ becomes

$$\tilde{F}(x,y,z) = F(x,y,z)\,\exp(-jk_o n_o z)\,, \qquad (3.73)$$

where the amplitude is a slowly varying function of z and the beam is assumed to be quite parallel to the z-direction. Substituting Eq. (3.73) and (3.71) into Eq. (3.69), we have

$$F(x,y,z+\Delta z) = \exp\left[-j\Delta z\left(\frac{\nabla_\perp^2}{(\nabla_\perp^2+k_o^2n_o^2)^{1/2}+k_on_o}+\chi\right)\right]F(x,y,z) + O(\Delta z^3)$$

$$\cong \exp\left[-j\frac{\Delta z}{2}\left(\frac{\nabla_\perp^2}{(\nabla_\perp^2+k_o^2n_o^2)^{1/2}+k_on_o}\right)\right]\exp(-j\chi\Delta z)$$

$$\exp\left[-j\frac{\Delta z}{2}\left(\frac{\nabla_\perp^2}{(\nabla_\perp^2+k_o^2n_o^2)^{1/2}+k_on_o}\right)\right]F(x,y,z)+O(\Delta z^3)\ .$$

(3.74)

The first factor in the RHS of Eq. (3.74), $\exp\left[-j\frac{\Delta z}{2}\left(\frac{\nabla_\perp^2}{(\nabla_\perp^2+k_o^2n_o^2)^{1/2}+k_on_o}\right)\right]$, is equivalent to the wave propagation in a homogeneous medium with index n_o for a distance $\Delta z/2$, as shown in Fig. 3-12 for z between 0 and $\Delta z/2$. The factor $\exp(-j\chi\Delta z)$, which is position-dependent, represents a phase correction term. Once the initial condition F(x,y,z) is given, the field at $z+\Delta z$ can be evaluated by Eq. (3.74). Repeating the procedure, the propagation of the wave can be traced in a step-by-step manner. The analogy of Eq. (3.74) is equivalent to propagating an optical beam through a periodic array of thin lenses as shown in Fig. 3-12 [Feit78], where the lenses serve the purpose of modifying the phase of the beam. The complicated propagation problem is, then, converted into a simple calculation procedure. The smaller step size Δz, the smaller the truncation error.

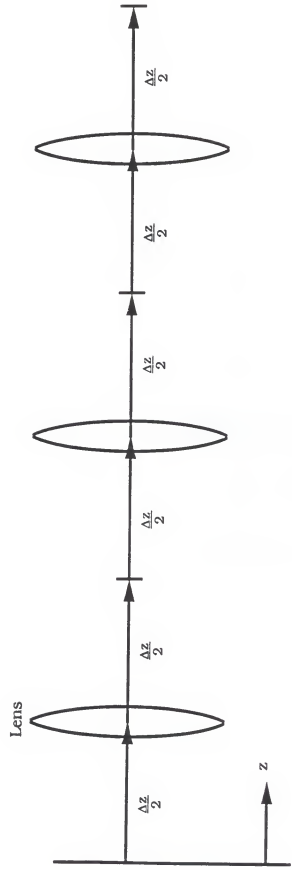

Fig. 3-12. The equivalent analogy of wave propagating in a medium by BPM expressed in Eq. (3.74).

3.4.2. Numerical Implementation

Equation (3.74) is the basic BPM equation for general cases. It can be reduced to a 2-D expression by writing F(x,y,z) as F(y,z), where z is the propagation direction and y is the transverse direction parallel to the waveguide surface. The effective index method is used to convert the 3-D (x,y,z) index profile into a 2-D (y,z) problem by slicing the devices vertically along x direction and calculating the effective index profile as a function of y for each slice as mentioned earlier. The difference is that the mode index of the effective index profile is not evaluated. The calculation involves solving for the propagation of the wave in a homogeneous medium n_o which is described by Okoshi [Okos85]. It will be briefly introduced here.

The first step is to evaluate the Fourier transform $F_n(z)$ of the field F(y,z):

$$F(y,z)=\sum_{n=-\mathcal{K}/2}^{\mathcal{K}/2} F_n(z)\exp(jk_{yn}y)\,, \qquad (3.75)$$

where $\mathcal{K}$ is the total number of points; $k_{yn}=\frac{2\pi}{L}n$; and L is the width of the computational area in the y direction. The field at $z+\Delta z/2$, before the lens, is expressed as

$$F_n(z+\frac{\Delta z}{2}) = \exp\left[-j\frac{\Delta z}{2}\left(\frac{\nabla_\perp^2}{(\nabla_\perp^2+k_o^2n_\delta^2)^{1/2}+k_on_o}\right)\right]F_n(z)\,, \qquad (3.76)$$

where $\nabla_\perp^2$ can be replaced by $-k_{yn}^2$ in the calculation. To evaluate the field just after the lens, we need the field in the spatial domain so that the phase can be calculated by the phase correction term. Therefore,

in the second step the inverse Fourier transform is employed to yield $F(y,z+\Delta z/2)$ before the lens. Next this field is multiplied by $\exp(-j\chi\Delta z)$ to obtain the phase corrected field and, then, propagating for $\Delta z/2$ to complete the calculation for the section Δz. Since the field is in k_y-domain at $z+\Delta z$, the calculation of Fourier transform is not necessary for the next section before the lens. Hence, one Fourier transform and one inverse Fourier transform are involved in the propagation through one section. The CPU time may be saved by using the fast Fourier transform (FFT). In the calculation the mode index and the mode field are not needed. The other advantage is that the radiation modes are not neglected. However, there are some limitations. First, the index must be close to the reference index n_o and the step size Δz must be small enough. Because of the nature of FFT, the boundary condition is periodic over the calculation width L. Therefore, absorbers must be placed at the calculation boundary so that the field is not transmitted beyond the boundaries or reflected to the waveguide region. The number of mesh points must be the power of 2 and the mesh points are equally distributed. BPM is also applicable to the simulation of 3-D devices. In this case, the 2-D FFT is used and $\nabla_\perp^2 = -k_{xm}^2 - k_{yn}^2$.

3.4.3. Simulation of Cross Coupler by BPM

The simulation of a cross coupler is given here as an example to illustrate the power of BPM. Cross couplers have wide applications in optical signal processing, *e.g.*, 3dB power divider [Huss89, Huss90]. The schematic of an asymmetric cross coupler is shown in Fig. 3-13.

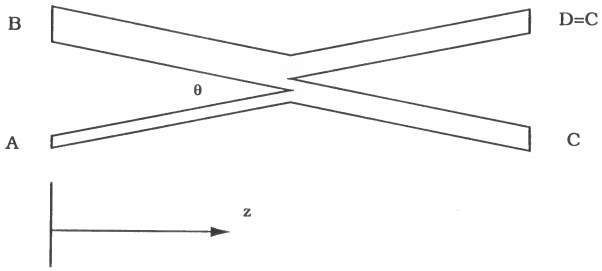

Fig. 3-13. Schematic diagram of a cross-coupler. The input branches A and B are asymmetrical, while the output branches C and D are symmetrical.

The waveguide width W_B is wider than W_A at input and W_C=W_D at output. As long as no mode conversion occurs, namely, the adiabatic condition is satisfied [Huss89, Huss90], the power inputs from branch A and B will keep in the first higher mode and the fundamental mode, respectively, through the device. It is obvious that the fundamental normal mode and first higher mode have equal powers at output branches since the structure is symmetric at the output. Thus, 3-dB power splitting is possible if the wave is input either from port A or port B. The simulation is shown in Fig. 3-14 for W_A=6.0 μm, W_B=8.0 μm and W_C=W_D=7.0 μm. The angle θ is 1.25 mrad. The figure shows the magnitude of the field as functions of y and z. The power input from branch B is equally divided at the output ports C and D. BPM can also be used to predict the radiation loss of the devices. This will be discussed in chapter 5 for the case of the tapered waveguides.

3.5. Summary of Numerical Methods

Systematic modeling for integrated optics is possible if we can simulate the index profiles and the fields in waveguide devices. In most cases, analytical solutions are not available. Therefore, numerical methods are of paramount importance. In this chapter, the Green's function method for the linear diffusion equation and the finite difference method for solving the nonlinear diffusion equation in the case of 1- and 2-D waveguides were introduced. The methods for solving the 1-D Helmholtz equation that were discussed in this chapter include the WKB method, the matrix method, and the finite

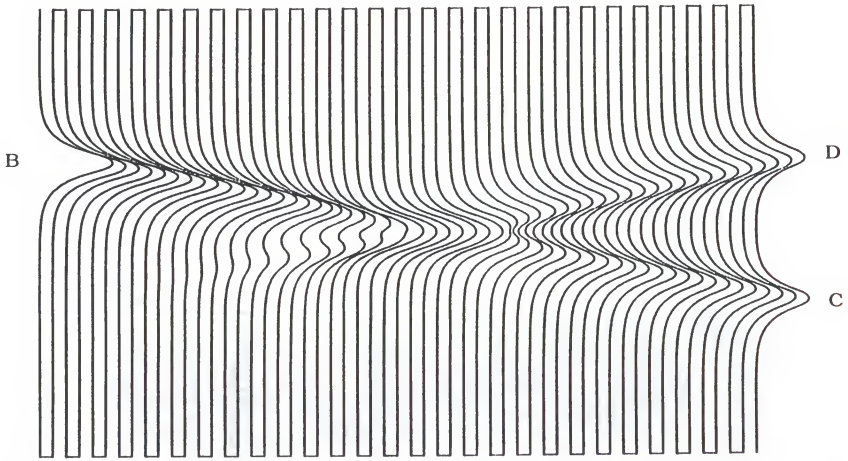

Fig. 3-14. Simulation of cross-coupler by BPM. The wave is launched from the left hand side and outputs from the right hand side.

difference method. The effective index method and the extended 2-D finite difference method used to solve the 2-D Helmholtz equation were also presented. Finally, the BPM was presented and its use was demonstrated by propagating a wave through an asymmetric 2X2 cross coupler.

CHAPTER 4
FABRICATION AND CHARACTERIZATION

4.1. Fabrication

The processing steps involved in the fabrication of ion-exchanged glass waveguides are quite simple and cost-effective. It can be done at relatively low temperatures (200~400^{o}C) compared to the fabrication of semiconductor waveguides. In general, the fabrication process is quite similar to the standard process in the well-developed silicon technology in the sample preparation and photolithography stages; this reduces the cost in the setup of the facility if the semiconductor processing equipments are already available. Clean areas and hoods are generally required to avoid contamination from the environment during the diffusion. In the diffusion, an external electric field can be applied to speed up the diffusion and, thus, reduce the processing time or temperature, as described in the previous chapters.

Several commercial glass substrates are available for fabricating ion-exchanged waveguides. Among them, BK7 glass has high optical homogenity, low loss at the wavelengths of interest and the ability to withstand the attack of molten salt, specifically the nitrate melt. The sodium and potassium ions in BK7 glass (see Table 1 for glass composition) are suitable for exchanging since they are glass network modifiers and have rather high diffusion coefficients compared to

other ions in this glass. The transition temperature of the glass is also higher than the temperature required for silver or potassium ion exchange. Therefore, we have chosen this glass for the ion exchange process.

As described in chapter 2, silver-ion exchanged waveguides can be fabricated by applying a field across the sample with the silver thin film as an anode [Vilj80]. The metallic silver is oxidized and driven by the external field into the substrate to form waveguides. However, in this project we emphasize the exchange performed in the molten salt bath since the diffusion setup is simpler and easier and yields low-loss waveguides. The process of fabricating high-performance, low-loss optical waveguides, briefly described in [Sriv87b, Zhen89, Chen90b], is detailed in this chapter. The fabrication of 1-D waveguides will be presented first since the fabrication is easier than 2-D waveguides. The process will be described in section 4.1.1 for 1-D waveguides and 4.1.2 for 2-D waveguides.

4.1.1. One-Dimensional Waveguides

One-dimensional waveguides are fabricated on a planar substrate without any masks on the glass and are useful in the characterization of the diffusion parameters such as the self-diffusion coefficient, the activiation energy, *etc.*, and waveguide parameter *e.g.*, the maximum index change. The process includes melt preparation, sample preparation, diffusion, and, finally, waveguide cleaning and polishing.

Melt Preparation

An aluminum beaker is used in the diffusion because the oxidized surface layer on the beaker is inert to the nitrate melt and both the Al and its ions cannot easily diffuse into the sample. Before preparing the melt, the container is thoroughly cleaned by using a commercial aluminum etchant at low temperature for two or three hours. Al etchant is rinsed away in de-ionized (DI) water. Next the beaker is dried by a nitrogen gun and baked on the hot plate for more than an hour at ~300^{o}C so that its surface is oxidized.

The preparation of the melt depends on the ions used in the exchange. For Ag^{+}-Na^{+} exchange in BK7, the salt bath consists of 0.333-MF KNO_3, 0.666-MF $NaNO_3$ and 10^{-3}-MF $AgNO_3$ which gives an index change of 0.012. Higher index change can be obtained by increasing the concentration of silver ions. The purpose of KNO_3 in the salt mixture is to prevent the K^{+} out-diffusion [Zhen89]; out-diffusion of K^{+} would cause cracks in the sample [Bran86, Zhen89]. A typical bath contains 300 grams of $NaNO_3$, 178.44 grams KNO_3 and 900 mg $AgNO_3$. The silver nitrate is weighed in a small teflon beaker to an accuracy of milligrams and added to the molten salt at 330^{o}C. The salt bath must remain clear during the addition of $AgNO_3$. If the melt is contaminated, it is likely that a dark or high-reflection thin film floating on the melt surface would be observed. Most frequently the contamination comes from the salts. Hence, ultrapure or ACS grade chemicals are recommended. Sometimes a careless cleaning of a thermocoupler or stirrer may cause the melt contamination.

Sample Preparation

First, a 2"X2"X1 mm substrate glass is fixed on the ceramic by wax and cut by a wafer saw into appropriate sizes, which depend on the application. For cross couplers, the length of samples can be as long as 2 inches. Usually, the size of samples is 1X1 inch square for straight channel waveguides. Since glass is isotropic, the orientation of the samples is not important in cutting. After cutting, each sample is marked by the diamond pen and cleaned.

Sample cleaning is done in a clean room under a hood because some chemicals are inflammable and hazardous to health. In the cleaning process, a dust-free N_2 gun is used to dry the samples. The wax on the samples is removed by alternatively and repeatedly immersing the samples into warm and fresh acetone and 1,1,1-Trichloroethane (TCA) in separate glass beakers. Each beaker must be labeled and used for only one chemical. After the wax is removed, a standard cleaning procedure is followed; the samples are tenderly washed with soap and DI water and dried by the N_2 gun. Care must be exercised due to the sharp edges of the glass after cutting. Next, the samples are subjected to sequential and quick immersions in warm and fresh acetone, TCA, acetone and methanol for two minutes each and prebaked.

Prebaking and Diffusion

The prepared substrates are transferred from the clean room to the processing laboratory in air-tight sample boxes and prebaked in an oven for several hours at 200°C to remove any moisture from the surface. The molten salt is ready for diffusion when it reaches the

desired diffusion temperature. The diffusion setup is shown in Fig. 4-1. A sample is placed on the bottom of the aluminum container with a thermocoupler next to the sample to accurately sense the substrate temperature. A 0.5-mm spacer is inserted between the beaker and hot plate to keep the beaker from direct contact with the hot plate since the temperature variation on the hot plate, controlled by an ON/OFF relay in the temperature controller, may be large and nonuniform. A teflon tape wrapped shield and a cover are used to insulate the beaker from the ambient. This allows desirable temperature uniformity in the melt, to within a few degrees C in the vertical direction and less than $1^{o}C$ in the horizontal direction. No stirrer is, therefore, required which simplifies the setup. The thermocoupler is calibrated by a mercury thermometer prior to the diffusion since difference in the readings by the common thermocoupler and mercury thermometers may be as large as $10^{o}C$. The temperature control and a precise temperature setting are very crucial since the waveguide characteristics strongly depend on the diffusion temperature.

Before the diffusion, the samples are heated by holding them just above the melt for a couple of minutes. A timer is used to monitor the diffusion time. Once the samples are immersed and covered by the molten salt, the timer is started. During the diffusion process, the substrates must be free of air bubbles on the surface otherwise they will cause inhomogeneous diffusion. The bubbles can be wiped out by the surface tension of the salt bath. They are removed by repeatedly taking the substrates out of the melt and quickly lowering them into the melt. The single-mode waveguides at 1.3 μm wavelength can be

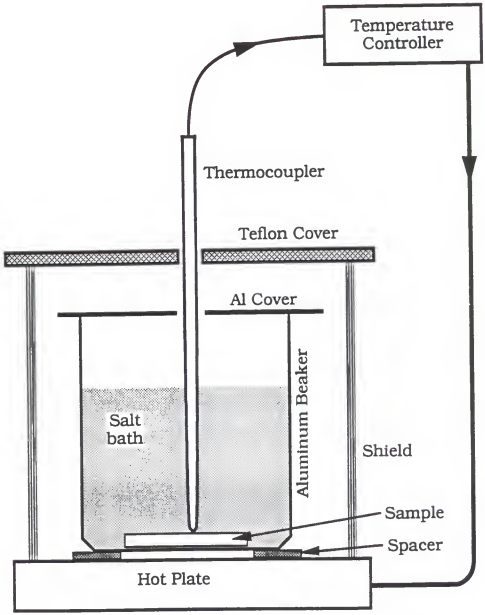

Fig. 4-1. The diffusion setup used in the ion-exchange process.

fabricated at 340°C by diffusing for about 8-12 hours in BK7 glass. Multimode waveguides are attainable by increasing the temperature or the diffusion time. After the diffusion is completed, the withdrawal of the samples from the melt should be slow so that no microcracking is induced in the glass. The substrates are pulled out of the melt and set aside to cool down to room temperature.

Waveguide Cleaning and Polishing

The salt on the glass is removed by rinsing the glass in DI water. The waveguides are cleaned again using the same standard procedure described earlier in this section.

The samples must be thoroughly cleaned before polishing in order to avoid scratches from dust particles. First, using Bee-wax, a small and cleaned glass pad is attached at edge of the waveguide surface to be polished, as shown in Fig. 4-2(a). The small pad serves as a protection from edge chipping during the polishing since the waveguides are usually only a few microns deep. The width of the pad is about 3 mm and the length is the same as the width of the subtrate. The pad-waveguide assembly is placed on the holder such that the distance between the substrate edge to be polished and the holder edge is about 2 mm. In the next step the sample and holder are tightly clamped together at wax melting point so that the gap between the waveguide and the pad is minimized (less than 5 μm) as shown in Fig. 4-2(b). Next a brass block is used to hold the clamp and the sample, as shown in Fig. 4-2(c). The substrate must exceed the surface of the block by approximately 1 mm so that this part can be easily polished away. To avoid damaging the block in the polishing, some glass slides

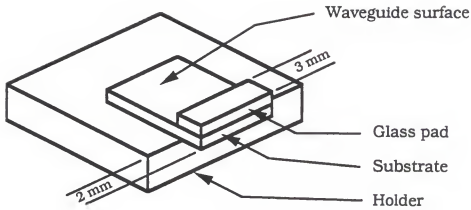

(a)

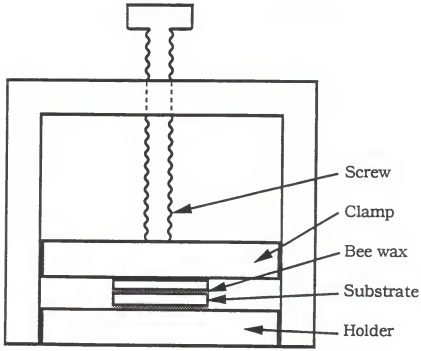

(b)

Fig. 4-2. The sample holder for polishing glass waveguides. (a) Substrate and glass pad waxed on a holder. (b) Side view of the clamped sample and holder.

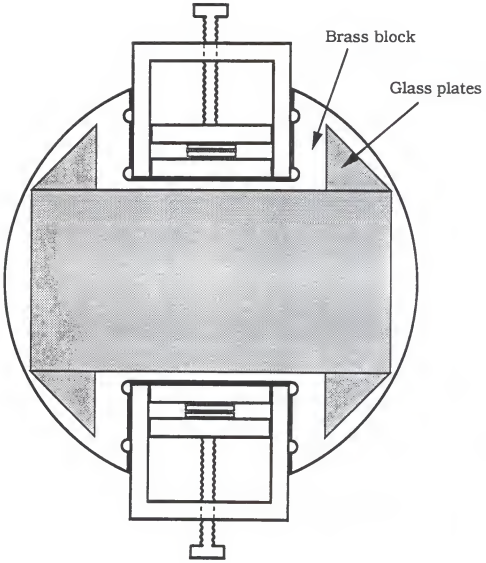

(c)

Fig. 4-2 – continued. (c) Brass block with sample holder. The shaded areas are the glass slides waxed on the surface of the brass block.

are waxed on the block surface as shown by the shaded areas in Fig. 4-2(c). The slides can also slow down the polishing rate.

The polishing procedures are described as follows. The sample is first ground by hand with grit 400 SiC powder until the surface of the polished sample edge is on the same level as the block surface. The surface of the sample edge is not smooth due to the roughness of the powder. After cleaning the block and the sample with water, the sample is polished by 5 μm alumina powder for about two minutes. Note that the position of the clamp on the brass block must be kept fixed to assure good polishing of the waveguide. The block is again rinsed in water and dried by a N_2 gun. In the next polishing step, 1 μm diamond paste on a nylon cloth, held by an adhesive back on a smooth disc, is used. In this step, the block rotates as the disk spins. Since the rotations of the block and the disc does not occur around the same axis, uniform polishing can be achieved. The polishing may last for 30~60 minutes depending on the scratch sizes before the fine polishing. After polishing and cleaning, the sample is checked under a microscope with oblique incidence light so that the scratches on the surface can be easily seen. A finer polish with a quarter micron diamond paste may be required for small-size (single-mode) waveguides. The edge of the sample at the pad-waveguide interface should be smooth and flat like a mirror after this step of processing. After polishing, the pad is removed by melting the wax. The bee wax on the waveguide is removed by warm TCA. If any residue is left on the waveguide, it is removed by soap and DI water. The samples are stored in a round sample box with the waveguide side up so that the polished edges may not be damaged by the box wall. If the glass substrates are

damaged or even broken, then all the efforts are done in vain. Polishing requires great care even though it is not the most critical step in dictating the performance of the devices.

4.1.2. Two-Dimensional Waveguides

The fabrication process of the 2-D or channel waveguides is similar to the 1-D waveguides except that some more steps are needed to define the channels. The processes include melt preparation, sample preparation, mask evaporation, photolithography, etching, prebaking, diffusion, polishing, and removal of mask, where the underlines highlight the additional steps for the 2-D waveguides. They are described in this subsection.

Choice and Evaporation of the Mask Material

The purpose of the mask is to prevent the diffusion of the silver ions into the undesired regions in the glass. The choice of the mask material is important because the mask must be able to 1) bond to the substrate tightly, 2) tolerate the attack of the nitrate melt at the diffusion temperature for the desired duration, 3) not react with the silver ions, 4) not contaminate the melt, 5) not diffuse into the substrate, 6) not affect (either retard or accelerate) the silver-sodium exchange in the mask opening region, 7) prevent the penetration of the silver ions in the masked region, 8) dissolve easily in a solvent after diffusion, 9) open windows with sharp edge by the etching or liftoff processes, and 10) be seen under the microscope in the mask aligner for alignment. Many materials have been tried in this laboratory, *e.g.*, Al, Ti, Cr, Ag, Al_2O_3, SiO_2, *etc.* It is found that the best

choice is a mask consisting of an Al film on a thin Al_2O_3 layer since this structure eliminates the shortcomings of both Al and Al_2O_3 films used alone. It was found that the aluminum film, used for years in our laboratory, may induce a local field at the edges of the mask opening just under the mask and reduce the silver ions into metallic form in that region, thus, increasing the loss of the waveguides [Walk83b]. The lowest loss silver ion-exchanged waveguides are usually found to be the ones with the least reduction of silver ions. The reduction of the silver ions into metallic silver can be identified by a yellowish color at edges of the waveguides. The Al_2O_3 film itself is not useful since it is transparent and not effective for blocking the diffusion of the silver ions. However, a composite structure consisting of Al_2O_3 and Al films eliminates the problems associated with the single-material film.

The mask is fabricated by E-beam evaporation at a vacuum of about 10^{-5} torr. Before this step, the samples must be completely cleaned and moisture- and dust-free. First, a 400 Å Al_2O_3 film is evaporated very slowly (~2Å/sec). The thickness is measured by quartz crystal thickness monitor. Next, a 1500 Å Al film is evaporated in about 15 seconds, which results in the structure shown in Fig. 4-3(a). The film should look shiny and mirror-like indicating good quality. If the carbon crucible for the Al evaporation is contaminated by aluminum carbide, the film may become yellowish and can not be easily etched away by Al etchant. Therefore, the crucibles must be changed frequently.

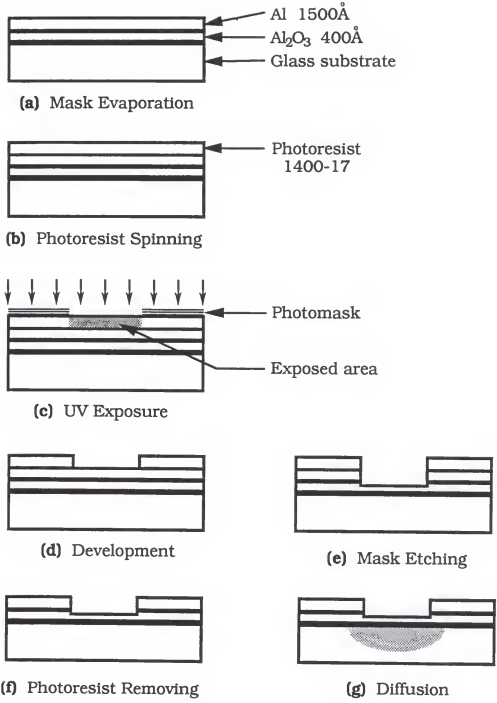

Fig. 4-3. Procedures to pattern the mask and fabricate 2-D waveguides.

Photolithography

After the evaporation, the samples are moved to the photolithography room as soon as possible for the photolithography processing. A N_2 gun with 0.45 μm filter is used to blow the samples. The sample is then loaded on the photoresist spinner which is set at 4000 rpm for 35 seconds spinning time. The Shipley 1400-17 positive photoresist is dropped on the sample by a syringe with a 0.45 μm filter until the sample is covered by the photoresist. After spinning, the thickness of the photoresist film is approximately 0.5 μm. The samples are then kept in an oven for soft-baking at 90°C for 30 minutes under N_2 atmosphere. The structure of samples at this stage is shown in Fig. 4-3(b). The light reflected from the samples should be uniform and have the same color, indicating the uniformity of the photoresist film.

The exposure of the photoresist is done by UV light (~365 nm wavelength) in the mask aligner, as shown in Fig. 4-3(c). The photomask, designed by a workstation VIA-100, has several band of the same patterns separated by a 100 μm opening. Each band has twenty straight channels whose openings are from 0.5 μm to 10 μm in a step of 0.5 μm. The separation of channels is 75 μm which is much larger than the dimensions of the mode fields. The material of photomask is usually anti-reflection coated chrome. Depending on the intensity of the light, the exposure time is set to 2.3 seconds. If the diagonally pin-point connected, one-micron grids, as shown in Fig. 4-4(a) are seriously connected after development without photoresist (Fig. 4-4(b)), then it is over-exposed. If they are seriously separated by

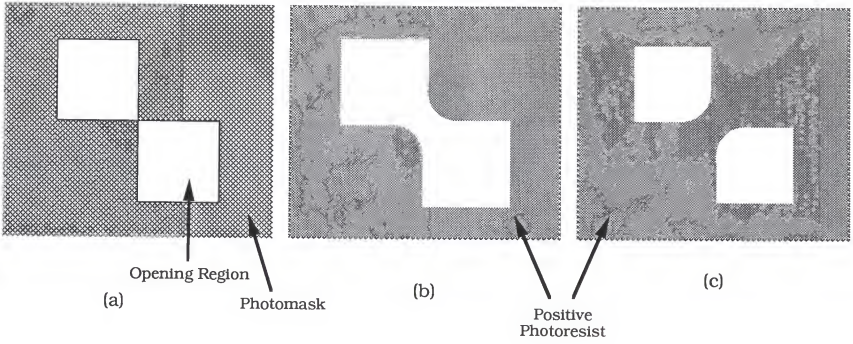

Fig. 4-4. Patterns used to check the exposure time. (a) Pattern on the photomask. The squares are 1 by 1 μm square, pin-point connected. (b) The squares are seriously connected after development. (b) The squares are separated by the photoresist.

the photoresist (Fig. 4-4(c)), then it is under-exposed. The exposure time must be determined to the precision of 0.1 second or within 5% error. The resolution of the photoresist is approximately one micron. The photoresist is developed for 50 seconds just after the exposure using Shipley 351 developer diluted in five-part DI water by volume. The development must be done at the same temperature (around $22^{o}C$) with gently stirring to assure reproducible results. Next, the sample is immediately rinsed in smoothly flowing DI water for one minute to stop the action of the developer and dried by the filtered N_2 gun. Figure 4-3(d) shows the sideview of the sample. The patterns are checked and measured under the microscope. If the UV exposure time is not correct, the pattern opening on the sample will be either larger or smaller than the opening on the photomask. If the edge of the pattern is rough, it may be caused by either the unclean photoresist or the dust or the residue photoresist on the master mask which must be cleaned before every use by the procedure described in the last subsection. The mask aligner is originally designed for semiconductor wafers of a thickness of less than 20 mils. For the substrate thickness of 40 mils or 1 mm, spacers are used to lift the photomask so that uniform and unstressed contact between the mask and the sample can be attained. Hard-baking of the photoresist after development is unnecessary for the aluminum etching process since the opened region on the Al film may be oxidized resulting in edge roughness in the etching process.

Etching

The etching process opens windows for ion-exchange in the regions defined by the photoresist on the Al and Al_2O_3 films. A commercial PAE etchant is used in this process; it consists of 16 parts phosphoric acid, two parts water, one part nitric acid, and one part acetic acid. The samples are immersed into the etchant for a couple of minutes and then stirred mildly. One extra minute of etching time is added from the time when the pattern is just etched through. Since the Al film may not be the same in each case, the total etching time may vary from sample to sample. After etching, the samples are rinsed in DI water at once to stop the etching process and wash the etchant away. The sideview of the sample after etching is shown in Fig. 4-3(e). The PAE etchant is also able to etch the alumina sandwiched between the Al and the glass. However, the etching rate is much slower than that for the Al film. Since the thin alumina layer hardly affects the silver-sodium ion-exchange, the etching of Al_2O_3 film is not critical. Although the alumina layer is very thin, yet the film helps weaken the local field induced by Al film as mentioned earlier and decreases the silver ion reduction under the mask at the waveguide edge. As a result, it can reduce the propagation loss of the waveguides. Again the opened pattern on the Al mask must be examined under the microscope and compared to the pattern on the photoresist. They should be exactly the same. Over-etched samples exhibit larger opening in the waveguide region with rougher edges while under-etched samples show darker spots or lumps in that region under a microscope. The resolution of an optical microscope is around one visible wavelength. However, it is still a convenient tool since the Al mask is opaque and

can be easily inspected. The width deviation of the waveguide and the edge smoothness of mask opening are primarily determined by the photolithography and the etching. Therefore, these two steps are crucial in the fabrication of high quality reproducible waveguides.

After the etching process, the photoresist is removed by acetone and the sample cross-section appears as shown in Fig. 4-3(f). To assure a complete removal of the photoresist, a photoresist remover with neutral pH value is used since the residue photoresist may cause contamination of the melt. The samples are cleaned again by standard cleaning procedure before the prebaking and diffusion.

Prebaking, Diffusion and Polishing

Basically these processes for 2-D waveguides are the same as 1-D waveguides. Prebaking oxidizes the surface of the aluminum, which helps strengthen the mask film on the sample. Longer diffusion time and/or higher temperature are used for fabricating single-mode 2-D channel waveguides than 1-D planar waveguides. After diffusion, the side view of sample appears as shown in Fig. 4-3(g), where the waveguide region is shown by the shaded area. In the polishing, the edge to be polished must be exactly normal to the channels except for some special applications where an inclined, polished edge is needed. Since the aluminum mask is still on the sample, the alignment for polishing can be easily done under the microscope.

Removal of Mask

The aluminum mask is removed by immersion in warm PAE etchant around 80°C for half an hour or longer. The undesired residue aluminum in the waveguide region may increase the waveguide loss.

The Al_2O_3 film can also be removed by the PAE etchant. However, nitric acid is used for this purpose. The sample is immersed in dilute nitric acid for about 30 minutes and then rinsed in DI water. After removing the mask, the waveguides must be cleaned by the standard procedure prior to the characterization.

4.2. Characterization

The optical waveguides are characterized by their index profile, mode index, field profile, losses, and spectral response for the quasi-TE and the quasi-TM modes. While all the techniques are presented in this chapter, the technique to measure the spectral response will be discussed in chapter 6. Since the substrate index as well as the characteristics of the waveguide depend on the wavelength, it is important to measure these characteristics by a monochromatical light source, or preferrably a laser source. Most of the measurements were done using a laser diode at 1.3 μm wavelength since the lowest dispersion[1] occurs at this wavelength in optical fibers. A He-Ne laser at 0.633 μm wavelength is generally used for alignment.

4.2.1. Mode Index of Planar Waveguides

The mode index of 1-D waveguides is useful in determination of the 1-D index profile as well as the diffusion coefficient and in projecting the fabrication conditions of single-mode channel waveguides. In this subsection the prism coupler [Tien69, Tien70, Ulri70] and inverse WKB method [Whit76, Chia85] are discussed, and

[1] Since the line width of light can never be zero, dispersion of a pulse is inevitable.

the results are compared to FDM to determine the self-diffusion coefficient of the silver ions. This methodology can be applied to the other ion-exchange systems to obtain the self-diffusion coefficient. This method to determine the self-diffusion coefficient is easier than the conventional technique using the isotropic tracer diffusion.

Prism Coupler

The prism coupler technique utilizes a high-index prism to launch the light into a waveguide. It has the ability to selectively excite only one of the guided modes in a multimode waveguide. Compared to the the grating coupling, the prism-coupler method is simpler and easier since no additional sample preparation is needed. Of course, the coupling into a specific mode depends on the coupling condition. The principle of operation is illustrated in Fig. 4-5 and briefly explained below.

Suppose that the incident angle θ at the base of the prism is larger than the critical angle $\theta_c=\sin^{-1}(n_a/n_p)$, where n_a and n_p are the index of the air and the prism, respectively. A standing wave in the direction normal to the prism base is formed due to the superposition of the incident wave and the totally reflected wave in the prism. The energy flow of the standing wave is in the direction parallel to the waveguide surface. The propagation constant of the input beam in the horizontal direction is

$$\beta_p = k_o\, n_p \sin\theta\,, \qquad (4.1)$$

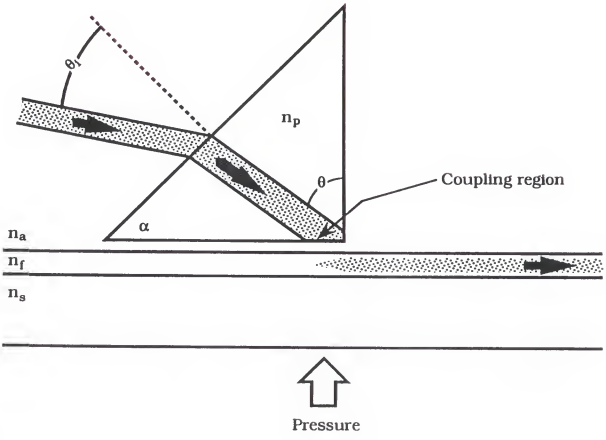

Fig. 4-5. Schematic diagram of a prism coupler. The light (shaded region) is launched into the waveguide through the prism. The waveguide is tightly clamped against the prism.

where k_o is the wave number in vacuum. If β_p is the same as the propagation constant of a guided mode, then the wave in the prism may couple into that mode in the waveguide according to coupled-mode theory. The above coupling condition can be expressed as

$$\beta_p = k_o n_p \sin\theta = k_o N , \qquad (4.2)$$

where N is the mode index and can be evaluated by measuring the coupling angle θ.

The gap which controls the coupling efficiency is itself controlled by the pressure on the pin-point support below the waveguide and must be adjusted to give optimal coupling. If the gap is too wide, then no coupling occurs to the waveguide modes. For single-mode glass waveguides, the gap is of the order of half a wavelength. The adjustment by varying the pressure on the support is somewhat critical. To achieve this thickness, both the prism and the waveguide surface must be clean and flat to avoid damaging the waveguide or the prism. The control of position of the coupling spot is also important to launch the maximum power into the waveguide. The position must be chosen so that the energy of the guided light in the waveguide does not transfer back to the prism. Note that from Eq. (4.2), n_p must be larger than the largest, fundamental mode index N_0. Since N_0 are different for different waveguides, the best way is to choose $n_p > n_s$, the surface index of the waveguide. We used a prism made by SF18 glass with refractive indices of 1.71653 and 1.69171 at 0.6328 and 1.3 μm wavelength, respectively. The glass has relatively high hardness and high transmission at both the visible and the near-infrared wavelength. The prism coupler technique is not applicable in the case

of the buried waveguides since the coupling may be very weak for the embedded waveguides.

Experiment and Measurement

The experimental setup is shown in Figs. 4-6(a) and (b), where figure (a) shows the light source part and (b) shows the prism coupler and detection part. Two linearly polarized lasers are used in the setup; a 1.3 μm wavelength semiconductor laser and a 0.633 μm He-Ne laser. Only one source is used at a time; the other one is blocked. The visible He-Ne laser is employed for alignment. A chopper and a compensator are inserted at position A (B) for measurement at 1.3 (0.633) μm. The compensator adjusts the polarization so that linearly polarized light can be launched. The microscope objective lens OBJ1 is used for collimating the output from the semiconductor laser; OBJ2 is used for coupling into the fiber, while OBJ3 (Fig. 4-6(b)) is used for coupling out of the fiber and focusing at the base of the prism. The distance between the fiber and the prism is about 50 cm so that the focused beam is almost collimated at the prism base. An XYZ transitional stage (not shown in the figure) is used to adjust the position of the coupling spot on the prism base so that the output is maximized and the position of the coupling spot is unchanged as the prism is rotated. The optimal position of the prism and the coupling spot for a collimated gaussian beam are discussed by Ulrich [Ulri70] and Tamir [Tami79]. The objective OBJ4 images the output at a germanium detector (DET1) through a slit. The signal from the detector is amplified and measured by a calibrated power meter and a lock-in amplifier is used to digitize it. Then the signal is sent to a microcomputer through an

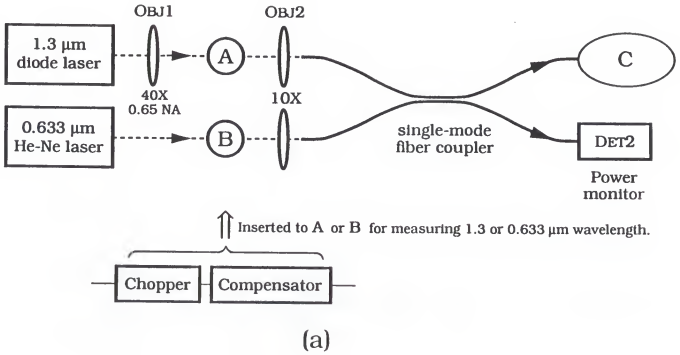

Fig. 4-6. Prism coupler measurement setup. (a) Light source part. The light is launched into a fiber coupler and split into a power monitor and measurement part denoted as C.

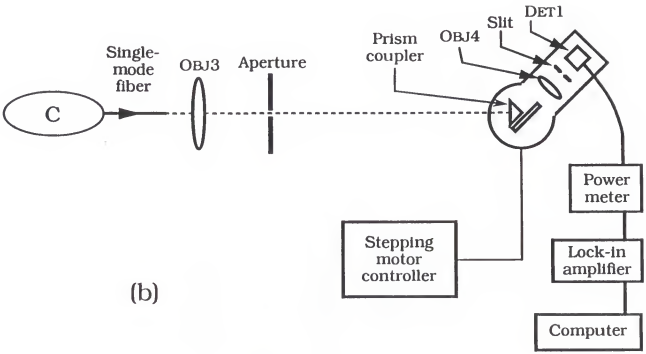

Fig. 4-6 – continued. (b) Measurement part. The light output from the fiber is focused at a prism. The signal is sent to a computer through a power meter and lock-in amplifier.

RS-232C interface. In figure (a), another germanium DET2 is used to monitor for laser power.

To measure the angle precisely, the stepping motor controller is reset to zero when the reflected light from the prism front surface passes through the aperture and refocuses on the fiber, thus, establishing the reference. The angle θ_i shown in Fig. 4-5 can be read directly from the stepping motor controller and corresponds to a peak in the power detected by DET1. θ_i is positive if the incident beam lies between the normal to the prism and its base. The mode index is given by [Tami79]

$$N = n_p \sin\left[\alpha + \sin^{-1}\left(\frac{\sin\theta_i}{n_p}\right)\right], \qquad (4.3)$$

where α is the angle between the base and the incident face of the prism. Three factors determine the accuracy of N: θ_i, α, and n_p. θ_i can be measured accurately to within a minute in radian which corresponds to an accuracy of 10^{-4} in the mode index. The other two factors α and n_p depend on the precision in the manufacturer's specifications. The polarization fluctuation in the fiber caused by the environment may reduce the measurement accuracy of the birefringent waveguides. The resolution of the measurement limits the maximum number of modes measurable in a highly multimode graded-index waveguide where the difference between the mode indices becomes smaller for higher-order modes. Therefore, a chopper and a lock-in amplifier in the setup are recommended to decrease the noise and improve the resolution.

Inverse WKB method

As described in the last chapter, the mode indices of a graded-index waveguide can be evaluated by the WKB method. On the other hand, the inverse WKB method is used to construct the index profile from given mode indices. Since the number of measured modes is limited as pointed out in the last subsection, a continuous index profile can not be exactly obtained. However, the method provides some useful information on planar waveguides *e.g.*, the maximum index change Δn_{max} and the depth of the index profile. Obviously, the larger the number of modes, the higher the accuracy in the constructed index profile.

The characteristic equation of a graded-index waveguide, expressed in Eq. (3.38), can be rewritten as

$$k_o \int_0^{x_m} [n^2(x)-N_m^2]^{1/2} dx = m\pi + \frac{\pi}{4} + \frac{\pi}{2} . \qquad (4.4)$$

We have assumed that ϕ_s and ϕ_c are $\frac{\pi}{4}$ and $\frac{\pi}{2}$, respectively, and the index profile n(x) is monotonically decreasing from the surface. For the fundamental mode (m=0), and the above equation becomes

$$k_o \int_0^{x_0} [n^2(x)-N_0^2]^{1/2} dx = \frac{3\pi}{4} . \qquad (4.5)$$

Suppose that the index function is approximated to be a linear function between $n(x)=n_s$ and $n(x)=N_0$:

$$n(x)=n_s - \left(\frac{n_s-N_0}{x_0}\right) x , \qquad (4.6)$$

where the maximum index at the glass surface is n_s and x_0 is the turning point of the fundamental mode. n_s is determined in two ways as will be described later. Substituting Eq. (4.6) into Eq. (4.5), we obtain

$$\frac{x_0 k_0}{n_s - N_0} \int_{N_0}^{n_s} \sqrt{x^2 - N_0^2}\, dx = \frac{3}{4}\pi \tag{4.7}$$

$$x_0 = \frac{\frac{3\pi}{4k_0}(n_s - N_0)}{\int_{N_0}^{n_s} \sqrt{x^2 - N_0^2}\, dx}$$

$$= \frac{\frac{3\pi}{4k_0}(n_s - N_0)}{\left(n_s \sqrt{n_s^2 - N_0^2} + N_0^2 \log \left| \frac{N_0}{n_s + \sqrt{n_s^2 - N_0^2}} \right| \right)}. \tag{4.8}$$

The first turning point x_0 can be evaluated by Eq. (4.8). For the first higher mode m=1, Eq. (4.4) is expressed as

$$\frac{7\pi}{4} = k_0 \int_0^{x_1} \sqrt{n^2 - N_1^2}\, dx$$

$$= k_0 \left[\int_0^{x_0} \sqrt{n^2 - N_1^2}\, dx + \int_{x_0}^{x_1} \sqrt{n^2 - N_1^2}\, dx \right], \tag{4.9}$$

where x_1 is the turning point for the first higher mode. Since the turning point for the fundamental mode is found by Eq. (4.8), the first integral of the right hand side of Eq. (4.9) from x=0 to x=x_0 can be evaluated. Again a linear approximation is used to interpolate the index profile between x=x_0 and x_1 in Eq. (4.9) as follows:

$$n(x) = N_0 - \left(\frac{N_0 - N_1}{x_1 - x_0} \right)(x - x_0) \quad \text{for } x_0 < x < x_1. \tag{4.10}$$

The turning point x_1 can be calculated by substituting Eq. (4.10) into Eq. (4.9). Thus n(x) is assumed to be a piecewise linear function with connected points at x_m. The procedure is repeated for other turning points. As a result, the approximate piecewise-linear index profile can be obtained.

Errors in the calculated index profile may be induced from the estimation of n_s as well as the accuracy in the measured mode indices. We have to estimate the surface index precisely to obtain an accurate index profile. Two methods are used to estimate the index at the surface [Whit76, Chia85]. The value of n_s mainly affects the accuracy of the lower order modes and not the higher order modes [Whit76]. The index profile evaluated from incorrect n_s may have very large error especially near the surface. Therefore, White and Heidrich [Whit76] proposed a method to optimize the smoothness of the index profile by evaluating the minimal value of the sum of the triangular areas defined by each of the three successive turning points x_k, x_{k+1}, and x_{k+2} and the associated mode indices N_k, N_{k+1}, and N_{k+2} (k=0, 1,...), *e.g.*, {(x=0, n_s), (x_0, N_0), (x_1, N_1)}, {(x_0, N_0), (x_1, N_1), (x_2, N_2)},..., *etc.* Note that the first set of the three points correspond to the surface index, the fundamental mode index, and the first higher mode index. For a waveguide with five modes, there are four sets of triangular points. Since the number of modes is limited, the computing time for minimizing the total area is short. This method can usually give satisfactory results even when the measured mode indices are not very accurate. This minimal-area technique is good for profiles with large variation at the surface, *e.g.*, erfc profile, exponential profile, *etc.* Chiang [Chia85] discussed an extrapolation technique to estimate the

surface index n_s by a given set of measured mode indices and the corresponding mode orders. Although Eq. (4.4) is valid for non-negative integers (m) only, it is allowed to have non-integral values for prediction of m which gives the hypothetical turning point at the surface with the maximum index n_s. Suppose that the upper limit of the integral on the LHS of Eq. (4.4) is at the surface x = 0. In this case the LHS equals zero and m = -0.75, indicating that the hypothetical mode having the turning point at the surface should have m = -0.75. Thus, the index at the surface can be obtained by extrapolating the given sets of points with the integer mode order m and the mode index N_m to m = -0.75. An effective-index profile N(m) as a function of m can be constructed by inter- and extra-polating the points between the measured points *i.e.*, m=0, 1, 2,.... . With N(m) a nearly continuous function, a smooth index profile n(x) can be obtained by using the procedure described earlier in this subsection. However, the extrapolation may not give an accurate n_s, resulting in a round-off error in the index profile at surface. Therefore, this extrapolation technique is good for evaluating n_s in those profiles which show slower variations near the surface, such as gaussian or parabolic index profiles. Usually, consistent results are obtained by the two methods above in the case of Ag^+-Na^+ exchange in BK7 glass. The predicted index profiles are usually more accurate in the region where the index is close to the substrate index. Hence, the width of the reconstructed index profile can be precisely determined by the inverse WKB method using either of the two methods.

4.2.2. Experimental Procedure to Determine the Diffusion Coefficient

The silver diffusion profile of the waveguide can be analyzed using an atomic absorption spectrophotometer (AAS) [Chlu87], an electron microprobe [Zhen89], or a scanning electron microscope (SEM) [Rama86, Lagu86a]. Alternatively, multimode planar waveguides can be characterized optically by measuring the mode indices with a prism coupler as described earlier and the index profile (concentration profile) can be constructed by the inverse WKB method. Figure 4-7 shows the normalized concentration (index) profile measured by various techniques for $N_{Ag}=2x10^{-4}$ MF in the soda-lime glass demonstrating excellent agreement in the results. As mentioned in chapter 2, a complementary error (erfc) function (solid line in the same figure) is obtained for low concentration of the silver ion in the glass. The width (W_{eff}) of the profile at 0.1573 points, yielded from the comparison, equals $2\sqrt{mD_At}$ (section 2.2.3), where t is the given diffusion time and m is taken to be 1.49 in this glass[Rama88d]. Thus, mD_A is evaluated by $(W_{eff}/2)^2/t$, which is concentration-independent for low silver concentration in glass. The double alkali effect is neglected in this case.

The waveguides which support one or two modes have either a small depth or a low concentration of silver ions (small Δn). In this case the silver concentration profile determined by the above methods is somewhat inaccurate due to the resolution of the measurements.

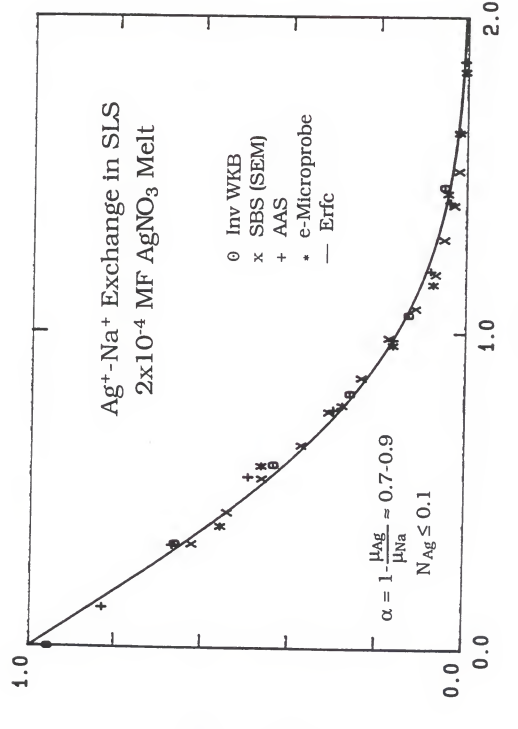

Fig. 4-7. Normalized silver concentration profile in soda-lime glass. The measured data points excellently fit to the erfc function (solid line) for concentration $N_{Ag} \leq 0.1$.

The inverse WKB is also not applicable since one or two modes are insufficient to construct a profile. In this case computer simulation [Rama88a, Chen90a] is used to model the index profile. First, the 1-D nonlinear diffusion equation (Eq. 2.22) is solved by the finite difference method to obtain the index profile. The unknown parameters used in the calculation are the self-diffusion coefficients of silver and sodium ions and N_{A0}, the mole fraction of the silver ions at the surface (see Eq. (2.24)). The parameters are substituted by a set of guessed values. The calculated index profile is, then, used in solving the Helmholtz equation to attain the mode indices by the finite difference method. In this step the unknown parameter is the maximum index change at surface of the waveguide. The index at the surface is assumed to be the same as that of a highly multimode waveguide. The solved eigen values (mode indices) are compared to the mode indices measured by the prism coupler. If the mode indices do not match, a new set of the guessed parameters are used. By trial-and-error, we thus fit the calculated mode indices to the measured ones. Once they are matched, the self-diffusion coefficient of the silver ions is obtained.

Figures 4-8(a) and (b) show the normalized index profile for the one-step diffusion without and with an applied field, respectively. The solid lines represent the theoretical curves and the discrete points denote the measured mode indices at the positions calculated by the inverse WKB method. The ion exchange of Ag^+ with Na^+ in soda-lime silicate glass was carried out at 330^oC with $2X10^{-4}$ MF $AgNO_3$ in $NaNO_3$ mixture. The silver concentration in the glass is less than 0.1 MF. The index profile, shown in Fig. 4-8(a), is expected to be similar

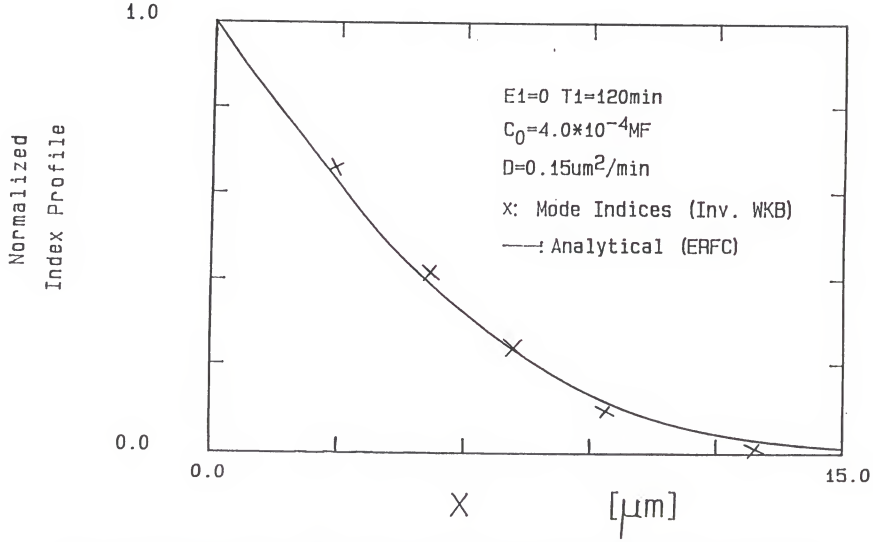

Fig. 4-8. Fitting of mode indices by the inverse WKB method. The discrete points are evaluated by the inverse WKB method from measured mode indices. The solid lines are the analytical results. (a) Diffusion without applied field.

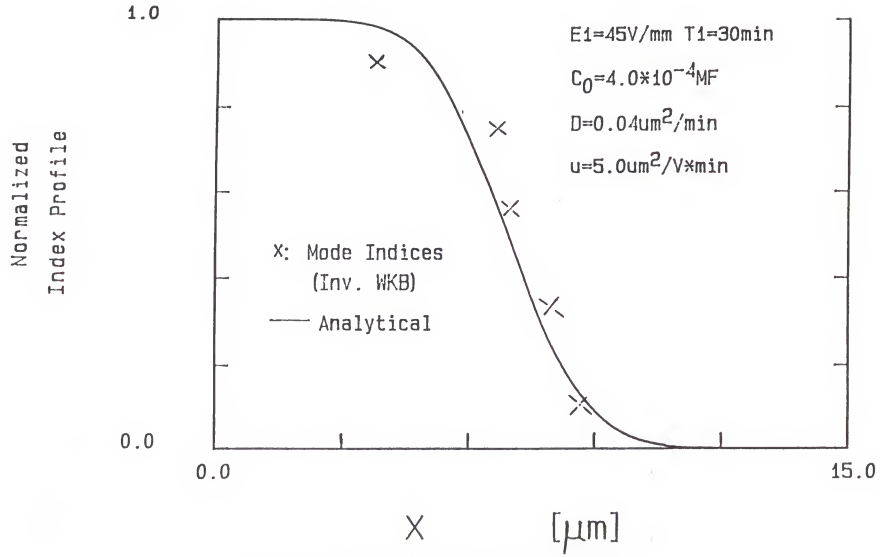

Fig. 4-8 – continued. (b) Diffusion with applied field.

to the erfc function for diffusion without the external field. There are five modes in this waveguide with a diffusion time of 120 minutes. The diffusion coefficient is found to be 0.15 μm^2/min in this case. The other curve in Fig. 4-8(b), showing zero slope at the surface, is the case of an applied field. The diffusion is performed for 30 minutes under an electric field of 45 V/mm. Five modes are observed in this waveguide. The best fit is obtained with D_A=0.04 μm^2/min and μ_A=5.0 μm^2/V•min. For the same temperature the diffusion coefficient is smaller for the case of the applied field. The reason is that the space-charge effect is enhanced by the applied field since the mobilities of silver and sodium ions are not equal. As discussed previously in chapter 2, the modeling assumes that the space-charge density is negligible and, therefore, the diffusion coefficient obtained by the theory is not the correct one. However, for the case of the diffusion without an applied field, the fitting method yields accurate results as will be demonstrated in the next chapter.

4.2.3. 2-D Mode Field and Loss Measurement

Mode field profile measurement is of paramount importance in characterizing single-mode waveguides and devices. The mode field of the guide determines the fiber-waveguide coupling loss, the performance of the directional coupler, *etc.* The light source setup is the same as shown in Fig. 4-6(a). However, the difference in this setup is that the light from the fiber coupler is launched into the waveguide directly, as shown in Fig. 4-9. A single-mode fiber is used to couple the light into either the TE or TM mode of the waveguide. The

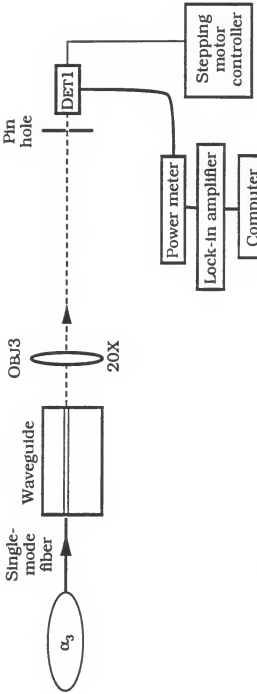

Fig. 4-9. The nearfield measurement setup. The light source part C is shown in Fig. 4-6(a).

polarization of the light is achieved by adjusting the compensator at position A or B (Fig. 4-6(a)) so that the linearly polarized light is obtained at output. The fiber must be kept as steady as possible to prevent polarization fluctuations during the measurement. The waveguide output is collected through a high-quality planar objective (OBJ3) by imaging the output on a germanium detector (DET1) with a 10 μm pinhole mounted in front of the detector.

The 2-D near-field intensity pattern is measured by scanning the detector-pinhole assembly horizontally and vertically by the stepping motor. Notice that the waveguide image is inverted by OBJ3 and magnified by about 65 times. The signal from DET1 is, then, sent to a lock-in amplifier through a power meter/current amplifier. A computer is interfaced with the lock-in amplifier to transfer the data from the amplifier. Often more than 500 points are sampled in each scan of about 1200 μm. Since the diameter of the pinhole is 10 μm, an unnecessarily large number of points does not increase the resolution of the measured intensity profile. Furthermore, too many data points may occupy a large space in storage disk and slow down the data processing speed. However, the averaging of a sufficient number of sampling points may smooth out the random noise in the signal.

The Fabry-Perot effect caused by the Fresnel reflections at the fiber-waveguide gap can be observed by the output power oscillation when adjusting the gap separation. Maximum transmission is obtained when the gap separation equals an odd number of quarter wavelengths since the index of the substrate is similar to that of the fiber. This requires submicron reproducibility of the transitional stage. The stability of the holders of the single-mode fiber, waveguide, and

objective OBJ3 is also important for reproducible measurements. A movement of 1 μm in the waveguide or OBJ3 will be magnified at the detector and may result in a shift of 65 μm in the image since the magnification factor is 65. By removing the waveguide, the near-field intensity profile of the single-mode fiber is also measured using the same setup. The horizontal and vertical profiles of the circularly symmetrical fiber must be the same and they are symmetrical if the fiber face is carefully prepared.

The magnification of the system is determined as follows. Since there are several single-mode waveguides on the same substrate and the separation of the straight channel waveguides is known, the magnification is measured by first aligning the detector at the maximum intensity when the fiber launches light into a waveguide (WG1) and then displacing the fiber laterally across the substrate to the next waveguide (WG2) and measuring the distance through which the pinhole has to be translated to collect the light from WG2. The magnification factor is obtained by dividing the translation distance of the pinhole by the separation between WG1 and WG2. After determining the magnification factor, the width and depth intensity profiles are obtained. The near-field profile is calculated by taking the square root of the intensity profile.

The loss of the waveguide can be measured by the same setup without the pinhole. First, the power output (P_{in}) from the single-mode fiber is measured. Next, the waveguide is inserted between the fiber and OBJ3. The power (P_{out}) is, then, measured by maximizing the fiber-waveguide coupling. In this case, in addition to the coupling and waveguide propagation losses, only the reflection at the waveguide

output end contributes to the insertion loss. The reflection of the objective OBJ3 is the same during the loss measurement with and without the waveguide and, hence, it is not considered in the loss measurement. The total insertion loss of the waveguide equals 10 $\log_{10}(P_{out}/P_{in})$ {dB}.

As pointed out earlier, the total insertion loss consists of three primary loss mechanisms: 1) Fresnel loss due to reflection of the optical field at the waveguide output end, 2) mode mismatch loss due to the difference in mode fields of the single-mode fiber and channel waveguide, and 3) propagation loss resulting from the surface scattering and absorption in the waveguide. The Fresnel loss of the waveguide due to the glass-air interface is determined by the substrate index. By assuming normal incidence and a small Δn, the loss is estimated to be $10 \log[4n_b/(n_b+1)^2] = -0.18$ dB for BK7 glass $n_b = 1.50371$ at 1.3 μm wavelength. The mode mismatch loss is calculated by maximizing the overlap integral:

$$\eta(x_0,y_0) = \frac{\left[\int_{-\infty}^{\infty}\int_{-\infty}^{\infty} E_f(x,y)\cdot E_g(x-x_0,y-y_0)\,dx\,dy\right]^2}{\left[\int_{-\infty}^{\infty}\int_{-\infty}^{\infty} E_f^2(x,y)\,dx\,dy\right]\left[\int_{-\infty}^{\infty}\int_{-\infty}^{\infty} E_g^2(x,y)\,dx\,dy\right]}, \quad (4.11)$$

where $E_f(x,y)$ and $E_g(x,y)$ are the mode field profiles of the fiber and waveguides, respectively. The mode mismatch loss is given by

$10 \log_{10}(\eta)$ (dB). Figure 4-10 shows the measured near-field intensity profile for the fiber (solid line) and a surface waveguide in the horizontal (parallel to the waveguide surface, denoted as '+') and vertical (normal to the surface, denoted as 'o') directions. It is clearly seen that due to the asymmetry in the index profile the mode field intensity profile in the vertical direction is asymmetrical and has narrow width compared to the symmetrical profile in the horizontal direction. The mismatch loss is 0.22 dB calculated by Eq. (4.11) in this case.

Once the reflection and mode mismatch losses are determined, the propagation loss of the waveguide can be obtained by subtracting them from the overall fiber-waveguide insertion loss. The lowest propagation loss of a single-mode, silver-exchanged surface-waveguide device in BK7 glass achieved to date is 0.15 ± 0.1 dB/cm [Chen90b]. If the propagation loss is below 0.1 dB/cm, then the technique described above is not adequate. Instead a resonant structure, *e.g.*, Fabry-Perot interferometer, ring resonator [Eguc83, Conn87], *etc.* must be used for an accurate loss measurement.

The reflection loss is usually inevitable without using an index matching fluid and, thus, it imposes a fundamental lower limit on the insertion loss. The mode mismatch loss can be reduced by adjusting the maximum index change and the fabrication condition or even burying the waveguide with a two-step diffusion process [Kane85, Lagu86a, Kane86, Rama86, Ross86, Chen88]. Recently, Pantchev [Pant87], Zhenguang *et al.* [Zhen88], Günther and Jestel [Gunt88], and Gevorgyan [Gevo90] demonstrated novel single-step diffusion

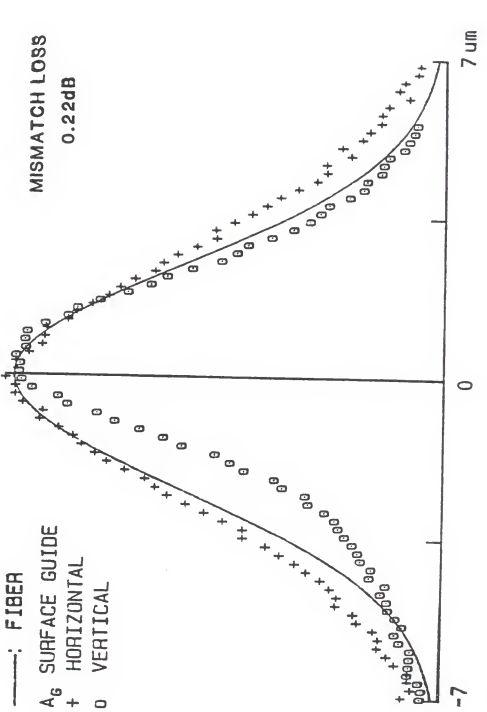

Fig. 4-10. Near-field intensity profiles of 2-D silver-exchanged surface waveguide and fiber. The mismatched loss is 0.22 dB between the waveguide and fiber.

processes to fabricate buried waveguides with an applied field. Such developments may be necessary to simplify the process and, as a result, reduce the cost of fabricating ion-exchanged waveguides.

4.3. Summary

In this chapter the fabrication processes for 1-D and 2-D Ag^+-Na^+ exchanged waveguides were described in detail. The characterization of 1-D waveguides by the prism coupler measurement and inverse WKB method allows determination of the diffusion characteristics and the associated index change. Characterization of the channel waveguides including the mode field and the loss measurement were also addressed. These characterization techniques are used in the simulation of the tapered waveguides in the next chapter.

CHAPTER 5
MODELING OF TAPERED WAVEGUIDES

5.1. Introduction

Tapered channel waveguides are extremely useful in integrated optical devices. Often they are used as interconnections between a single-mode fiber and a waveguide device with different mode sizes to reduce the mode mismatch loss since the tapered guide provides a smooth transition between them. In addition, an efficient short taper design permits the use of small devices resulting in an increased packing density. Suchoski and Ramaswamy [Such87] reported on tapers fabricated in Ti:$LiNbO_3$. Mahapatra and Connors [Maha88a] demonstrated a low loss thermal taper using Ag^+-Na^+ exchange in Corning O211 glass. Recently, Zhenguang *et al.* [Zhen89] achieved low loss, single-mode waveguides with near adiabatic, fiber-compatible tapers at both ends in BK7 glass, which is an important step before glass waveguides become useful in passive system applications. The understanding of the evolution of the index change, channel (guide) size, modal field, and propagation constant is of paramount importance in the design of low loss tapers. A model that tracks the above parameters as a function of the taper length and fabrication conditions is essential to gain a complete understanding of the performance of the tapered devices.

In this chapter, we first present a systematic study of modeling of the planar waveguides, followed by a model for straight channel waveguides and tapered transitions in BK7 glass [Chen89b, Chen90a]. Using 1-D multimode planar waveguides, we determine the diffusion coefficient, index profile, and surface index change. The calculated diffusion coefficient and estimated index change are in good agreement with the measured values. These parameters are employed for the 2-D modeling of straight channel waveguides of different widths. Again, the results are compared to the experimental data to ensure the accuracy of the modeling.

The first step of the taper fabrication process is similar to that described in the last chapter (Fig. 5-1(a)). In the second step, which we call postbaking, thermal tapers are formed by nonuniform diffusion under a thermal gradient along the waveguide direction since the diffusion coefficient is a function of temperature, as shown in Fig. 5-1(b). Therefore, the tapered waveguide dimension in the propagation direction can be controlled by varying the temperature along this direction. The thermal gradient causes the maximum index change at the surface to decrease and the size of the waveguides to increase along the taper. In order to analyze the tapered waveguide, the taper is sectioned longitudinally with its own distinct waveguide parameters in each section as a 2-D channel waveguide. The index change is assumed to be proportional to the silver concentration, and the negligible birefringence observed in these guides [Zhen89] demonstrates that they are nearly stress free [Bran86]. Hence, the index changes at the surface are the same for both the TE and TM modes. The 2-D nonlinear diffusion equation Eq. (2.21) for the ion exchange and the

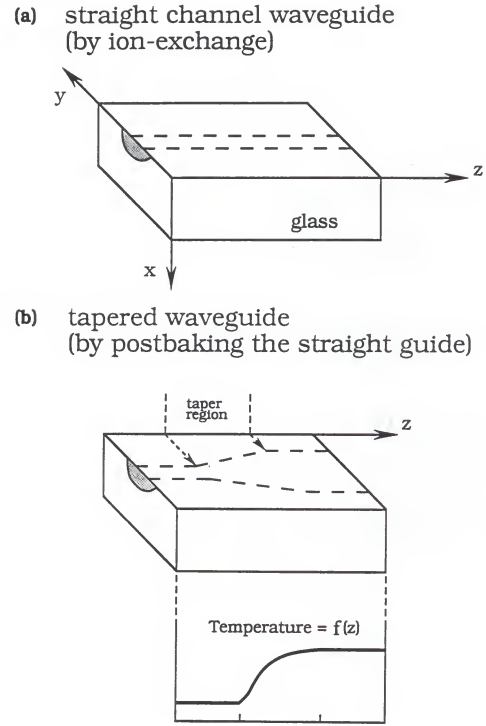

Fig. 5-1. Schematic diagram of (a) a straight channel waveguide fabricated by a single step binary ion exchange and (b) a tapered guide by postbaking a straight channel under a thermal gradient.

2-D Helmholtz wave equation Eq. (3.36) are numerically solved by FDM as discussed in chapter 3. An Arrhenius type relation, Eq. (2.40), is used to represent the self-diffusion coefficient of silver ions for the nonuniform temperature diffusion. The results show that the calculated index profile and mode sizes along the taper agree very well with the measured values for the cases of straight channel waveguides as well as the tapers. The agreement shows that the model can be used to predict the evolution of the index profile, propagation constant, and size of the modal field in single step as well as two-step ion-exchanged waveguides. The radiation loss of the tapered waveguides is evaluated by BPM for various taper profiles, *e.g.*, linear, quadratic, raised-sine *etc.* as functions of taper length in the z direction [Chen89a]. It is also useful in predicting the mismatch loss in a coupler between devices using tapered transition.

5.2. Modeling

As shown in Fig. 5-2, the modeling includes three parts: the modeling of planar waveguides, channel waveguides, and tapered waveguides. Simulations and experiments were done simultaneously to ensure the accuracy of the modeling.

5.2.1. Planar Waveguides

The multimode planar waveguide is modeled first, to get the fitting parameters, which are used in the simulation of the channel and tapered waveguides as shown in Fig. 5-2. The 1-D index profile of the planar guide in the x-direction is obtained by first solving the 1-D

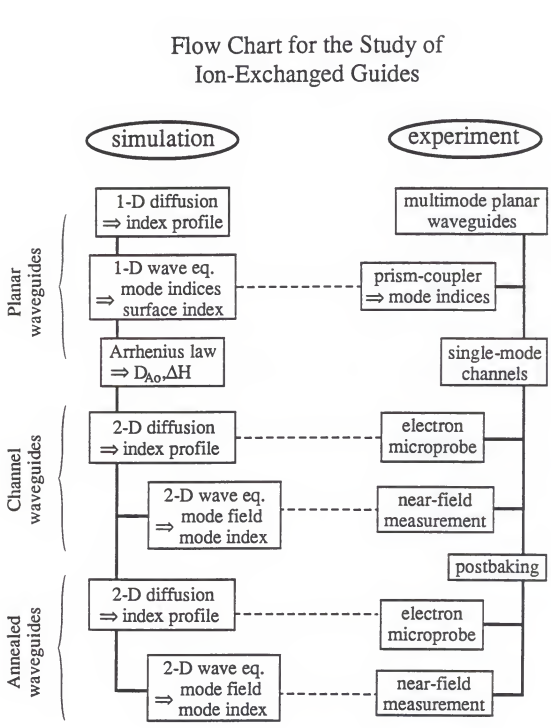

Fig. 5-2. Flow chart of the modeling of planar, channel, and tapered waveguides that includes the simulation and correlation with experimental results.

nonlinear diffusion equation Eq. (2.22) by FDM. The initial and boundary conditions are expressed by Eq. (2.24). However, a close-form solution is not available in this case. The fitting parameters are α, N_{A0}, D_{A0}, and ΔH for 1-D waveguides. N_{A0} depends on the ion-exchange equilibrium condition [Rama88d] at the glass surface. To choose appropriate values of α and N_{A0} for the initial fitting parameters, we first analyzed the index profiles which were reconstructed by the inverse WKB method from the mode indices of multimode waveguides measured by the prism coupler technique as described in the last chapter. The magnitude of αN_{A0} determines the slope of the index function at the surface. The initial values of N_{A0} and α for the fitting of the calculated and experimental index profiles can be estimated from the slope of the rebuilt index profile obtained using the inverse WKB method, so that the fitting parameters N_{A0} and α are readily obtained. The self-diffusion coefficient D_A dictates the width of the index profile or the depth of the waveguide. Thus, the technique involves choosing N_{A0} and α first and varying D_A until the depth of diffusion is matched. Then N_{A0} and α are adjusted again to achieve the best fit of the index profile. Figure 5-3 shows both the calculated index profile (solid line) and the experimental profile (cross-points) in BK7 glass. The diffusion was performed for 48 hours at 330°C in a melt of 0.33 MF KNO_3, 0.67 MF $NaNO_3$, and 0.001 MF $AgNO_3$. The best fitting values of N_{A0} and α are found to be 0.9 and 0.99, indicating that the self-diffusion coefficient of the silver ions is two order of magnitude less than that of sodium ions. The surface index change Δn_{max}, which is linearly proportional to N_{A0}, is estimated to be 0.02 at 0.633 μm wavelength for the above melt composition. The cross-points denote

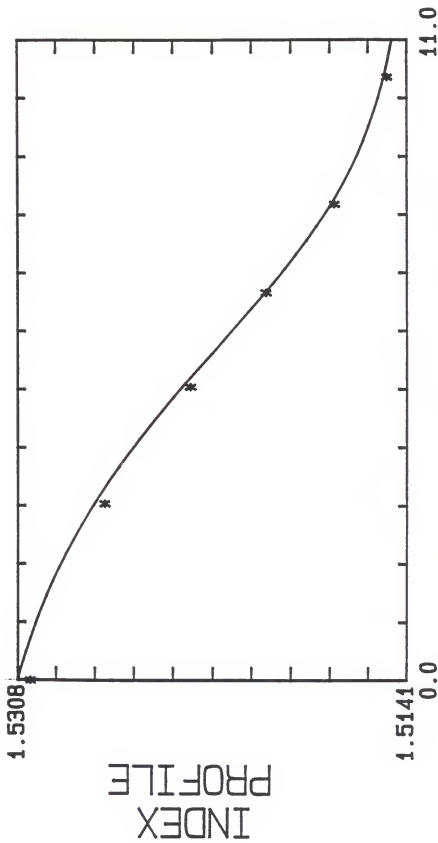

Fig. 5-3. Index profiles of a multimode planar waveguide reconstructed by an inverse WKB method (cross-points) from the prism-coupler measurement and solved by FDM (solid-line). The fabrication condition is described in the text.

the reconstructed profile of a multimode planar waveguide using the inverse WKB method employing the measured mode indices. For this case, the self-diffusion coefficient of silver ions in BK7 glass at 330°C was estimated to be $2.9X10^{-3}$ μm^2/min. The results show a gaussian-like profile for the silver exchanged waveguide in BK7 at this concentration. Several multimode waveguides were fabricated at different diffusion temperatures, and in each case the self-diffusion coefficient (D_A) was evaluated using the above procedure, resulting in the temperature dependence of D_A. Figure 5-4 shows the calculated self-diffusion coefficient of silver ions in BK7 as a function of the diffusion temperature for the above melt. The coefficients D_{A0} and ΔH in the Arrhenius relation Eq. (2.40) are found to be $3.705X10^6$ μm^2/min and 105.1 kJ/mole, respectively. The activation energy is close to that reported by Eguchi *et al.*, 98.7 kJ/mole [Eguc83].

Multimode planar waveguides allow the determination of N_{A0}, α, D_{A0}, and ΔH. These values are used for channel simulation as shown in Fig. 5-2. The self-diffusion coefficient of Ag^+ in channel waveguides is assumed to be the same as that of the planar waveguides.

5.2.2. Channel Waveguides

The 2-D diffusion equation is also numerically solved by FDM. However, the boundary conditions are modified to accommodate the diffusion through the mask opening. In the mask opening region, the concentration of cation A at the surface, is the same as in the planar waveguide case, namely, N_{A0}. Under the mask, the concentration

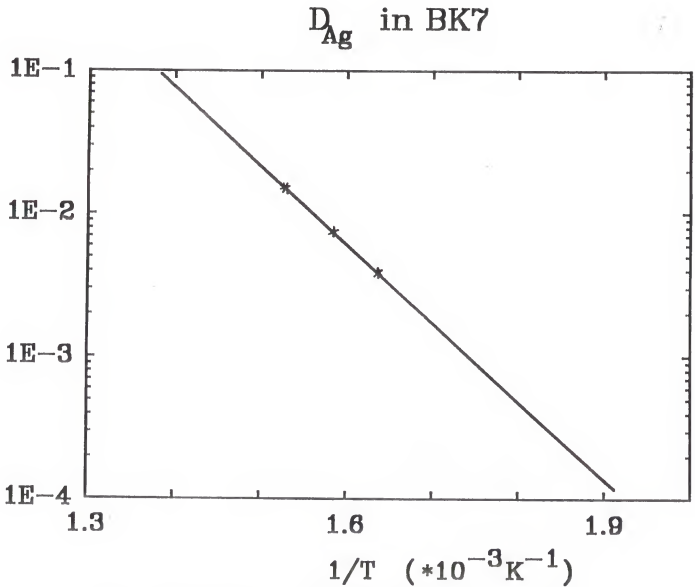

Fig. 5-4. Self-diffusion coefficient D_{Ag} (μm^2/min) of silver ion in BK7 as a function of temperature.

gradient of ion A is set to zero in the vertical direction at the air-glass interface:

$$\left.\frac{\partial N_A}{\partial x}\right|_{x=0} = 0 . \qquad (5.1)$$

The numerical accuracy of the results is checked by comparing with a 1-D analytical solution, which is a complementary error function for α=0 as discussed in chapter 2. The index profile, obtained from the diffusion simulation for channel waveguides by using the parameters (D_{A0} and ΔH) from our 1-D modeling, is compared with the concentration profile of single-mode channel waveguides, obtained by an electron microprobe, as outlined in the flow chart in Fig. 5-2.

The 2-D Helmholtz equation Eq. (3.36) is solved by FDM with the assumption that the field vanishes at the outer calculation boundary. The separation between the outer boundaries in both the horizontal and vertical directions is chosen to be much larger than the widths of the mode fields so that the above assumption is valid. Finally, the mode fields of the channel waveguides calculated by FDM are compared to the near-field measurements. In the experiment, considerable effort was put into fabrication of the single-mode waveguides since they have wide applications in the optical communication system. Hence, in the simulation of channel and tapered waveguides, we focus only on the fundamental mode.

5.2.3. Tapered Waveguides

In the simulation of the second step, *i.e.*, postbaked waveguides, the first step concentration of ion A is used as the input. The

concentration gradient of ion A in the vertical direction at the air-glass interface is set to zero, as before, in the region under the mask. Since the width of the waveguide becomes larger after postbaking and the total number of cations A remains constant, the maximum concentration of ions at the surface decreases with the maximum index change still occurring at the surface. As described previously, the tapered guide was sectioned along the longitudinal direction for modeling purposes with each section having a lower Δn_{max} and larger waveguide size than the straight channel waveguide depending on the temperature during postbaking (and hence location) along the waveguide direction. The same procedure outlined previously for the channel waveguide was used to simulate each section making up the taper. The simulation results of the two-step process are again checked by the electron microprobe data (procedure indicated in the flow chart in Fig. 5-2). As before, the 2-D Helmholtz equation was solved to determine the mode fields and mode indices in each section.

5.2.4. Results and Comparison with Experiment

In this subsection we present the simulation results on Ag^+-Na^+ exchanged waveguides and tapered transitions and compare them with the experimental results. The full widths of the index profile at 1/e points in the horizontal and vertical directions represented by d_y and d_x, respectively, are shown in Fig. 5-5 as a function of the mask width W_M for straight surface channels. The surface channels are made at 340°C for 12 hours with 10^{-3} MF silver nitrate in the melt. The open rectangles ❑ show the index profile widths measured by the

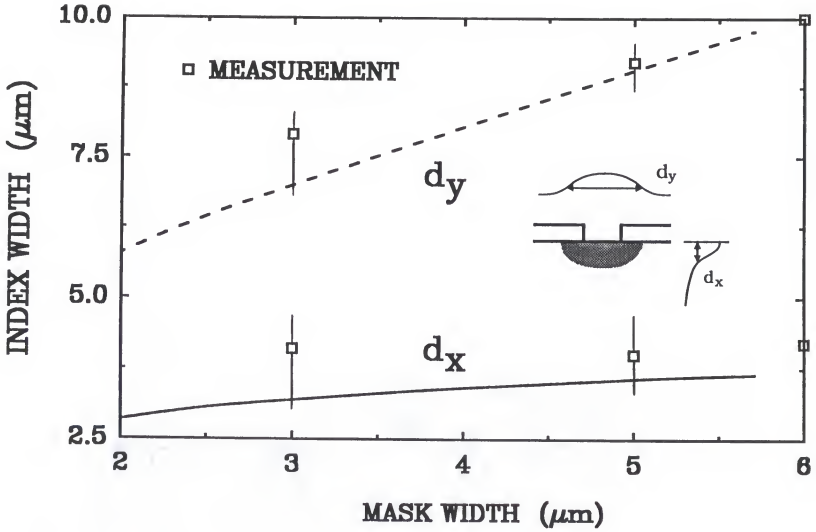

Fig. 5-5. 1/e width (d_y, dashed line) and 1/e depth (d_x, solid line) of the index profile vs. the mask opening. The open squares with the error bars are measured values using an electron microprobe.

electron microprobe for mask openings W_M = 3, 5, and 6 μm [Zhen89]. The electron microprobe data are not as accurate as is desired due to the destructive nature of the measurements. In other words, if the width of the profile is measured, the depth can not be measured accurately. This error decreases with increasing mask width as shown by the error bars in the figure. Figure 5-6 shows the lateral diffusion defined as (d_y - W_M) vs. W_M and represented by the dashed line. The solid line shows the diffusion depth of the surface channels normalized to the depth of the planar waveguide d_p fabricated under identical conditions. The lateral diffusion tends to saturate at ~4 μm for mask openings larger than 3 μm. Therefore, d_y increases proportionally with W_M so that (d_y - W_M) saturates for W_M > 3 μm. As seen in Fig. 5-6, d_x/d_p is limited by the mask opening and approaches a value of only 0.75 for W_M = 6 μm. (The waveguides are multimode for W_M > 6 μm.) The variation of the full widths of the mode fields at 1/e intensity points in the horizontal and vertical directions, W_h and W_v, respectively, is shown in Fig. 5-7. The discrete points represent values obtained by the near-field measurement. The aspect ratio defined as W_h/W_v is usually larger than one for surface waveguides. The mode size increases at small mask openings since the guides are near cutoff. W_v decreases monotonically and approaches the mode size of the corresponding planar waveguide as W_M increases. W_h first decreases and increases again for wider mask openings, which shows that the modes are near cutoff for narrower channels and well confined for wider channels in the horizontal direction.

The results described so far give insight into designing tapers by varying the mask width only. The channels become multimoded for

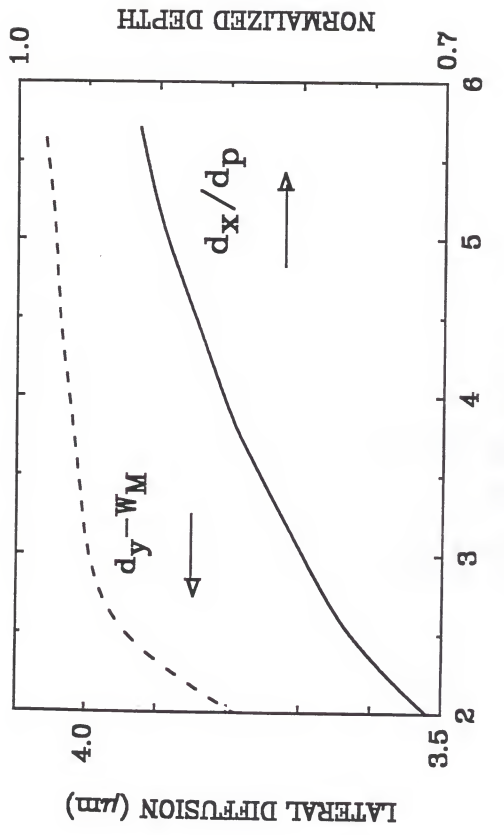

Fig. 5-6. Lateral diffusion (d_y-W_M, dashed line) and normalized depth (d_x/d_p, solid line) as functions of the mask opening W_M, where d_p is the 1/e diffusion depth of the surface-planar waveguide fabricated in the same conditions.

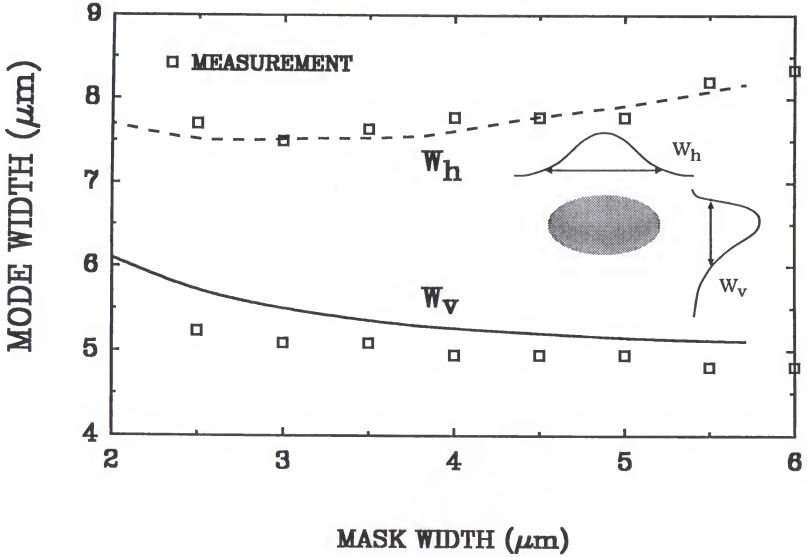

Fig. 5-7. 1/e widths of the mode fields in the horizontal direction (W_h, dashed line) and the vertical direction (W_v, solid line) as a function of mask opening. The open squares are data points obtained by the near field measurement.

W_M > 6 μm, which implies that a single mode waveguide with tapered mode size in the longitudinal direction is difficult to make in one step by varying only the mask opening. Tapered waveguides fabricated by just varying the mask width are expected to approach cutoff at the narrow end or become multimoded at the wide end. Figure 5-8 shows the diffusion depth d_x as a function of the diffusion time in the first step process for the planar guide as well as for channels of W_M = 8 and 3 μm. The processing parameters are the same as those for the data presented in Figs. 5-5 to 5-7, except that the diffusion time is allowed to vary now. The diffusion times of single-mode operation with 8 and 3 μm mask openings are between ~90 and 230 min and 180 and 830 min, respectively. The diffusion time for the single-mode waveguide with W_M =8 μm requires more accurate control than that of the channel with W_M = 3 μm. Single-mode tapered waveguides with W_M from 3 μm to 8 μm in the longitudinal direction can be obtained by diffusing the silver ions in the interval between 180 and 230 min. For mask opening covering more than this range, the control of diffusion is even more critical to fabricate single-mode tapered waveguides. If the narrow end of the tapered waveguide is close to cutoff, the mode size may not monotonically increase along the longitudinal direction even though the waveguide is single mode. Furthermore, the scattering loss is expected to be larger for the waveguides or tapers near cutoff.

In the postbaking technique presented here, the control of the postbaking time to make a single-mode tapered waveguide is not as critical as that of the diffusion time in the single step process (Fig. 5-8), resulting in better controllability and assured reproducibility. The

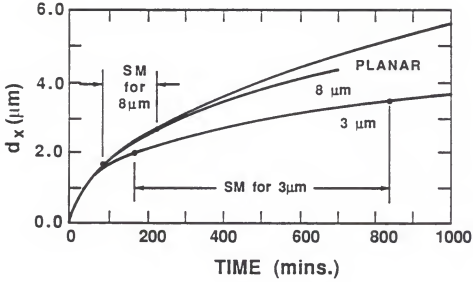

Fig. 5-8. Calculated depths of index profile d_x as a function of the diffusion time. d_x for planar waveguide and the channel waveguides for W_M= 3 and 8 μm fabricated in the same condition. The arrows show the single mode regions for the channel waveguides at λ = 1.3 μm.

calculated width of the index profile in postbaked guides versus temperature is shown in Fig. 5-9. The mask opening is chosen to be 3.5 μm in the first step because the channel guide supports fairly well guided mode with good mode circularity and low loss. The postbaking time is 5 hours. Both the depth and width increase as the temperature increases. The experimental values before and after postbaking, shown as open rectangles, are in excellent agreement with the calculated values for d_y. The figure shows that the width of the taper is not a linear function in the longitudinal direction, although the temperature distribution [Zhen89] was nearly linear. Since the total number of silver ions remains almost constant as a result of postbaking, the maximum index of the waveguide n_s at the surface decreases with increasing temperature (Fig. 5-10) when the waveguide size becomes larger (Fig. 5-9). The dark circle in Fig. 5-10 denotes n_s before postbaking. The normalized frequency V (Fig. 5-11), which equals $k_o d_x \sqrt{2 n_b \Delta n_{max}}$, increases slowly with temperature compared to the change of widths of the waveguides (Fig. 5-9). Again the dark circle data point denotes the V value before postbaking. The normalized mode index $b = (N^2-n_b^2)/(n_s^2-n_b^2)$ (Fig. 5-12), where $N = \beta/k_o$ is the mode index and n_b is the bulk substrate index, increases slightly at lower temperatures because initially the mode index does not drop as much as the surface index and also the size of the waveguide increases. However, at higher temperatures, b decreases and moves closer to cutoff due to a larger asymmetry factor resulting from the lower surface index, even though V increases (Fig. 5-11). The dependence of b on the postbaking temperature is useful in designing devices where phase matching is critical, such as directional couplers, grating

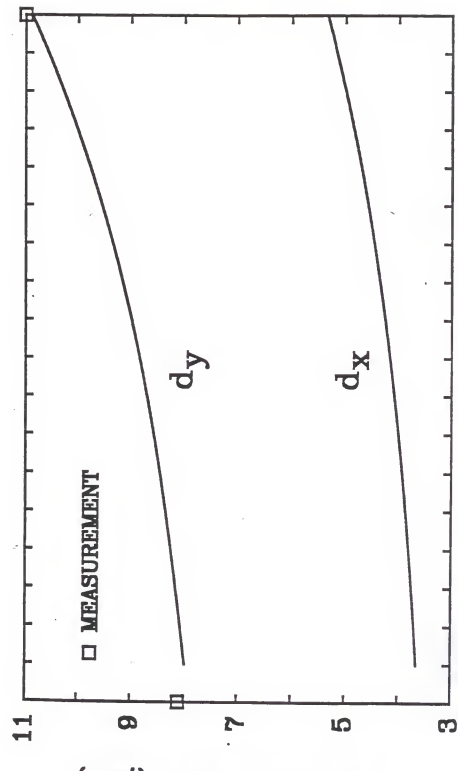

Fig. 5-9. Width d_y and depth d_x of the index profile for the tapered waveguide vs. the postbaking temperature. The open squares show the data measured by the electron microprobe, and the solid lines are calculated values.

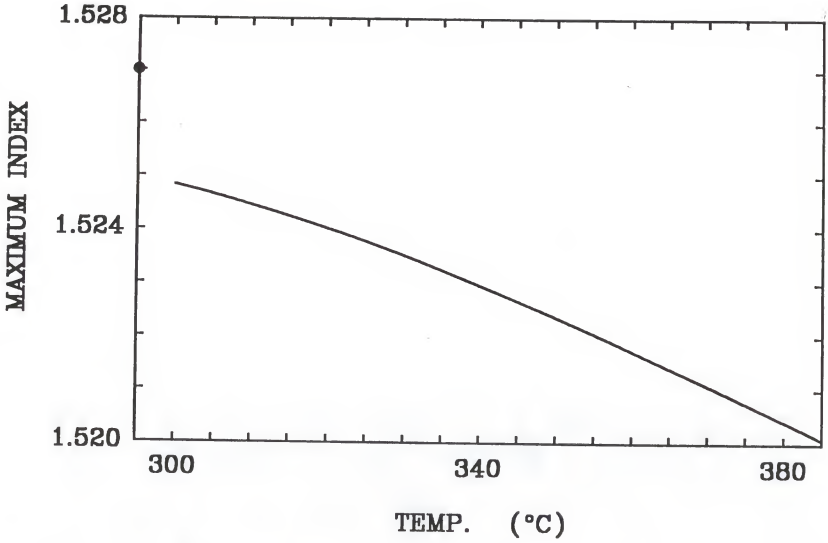

Fig. 5-10. Calculated surface index n_s vs. postbaking temperature. The closed circle on the vertical axis shows the calculated data point prior to postbaking. The same symbols are used for the values before postbaking in Figs. 5-11 – 13.

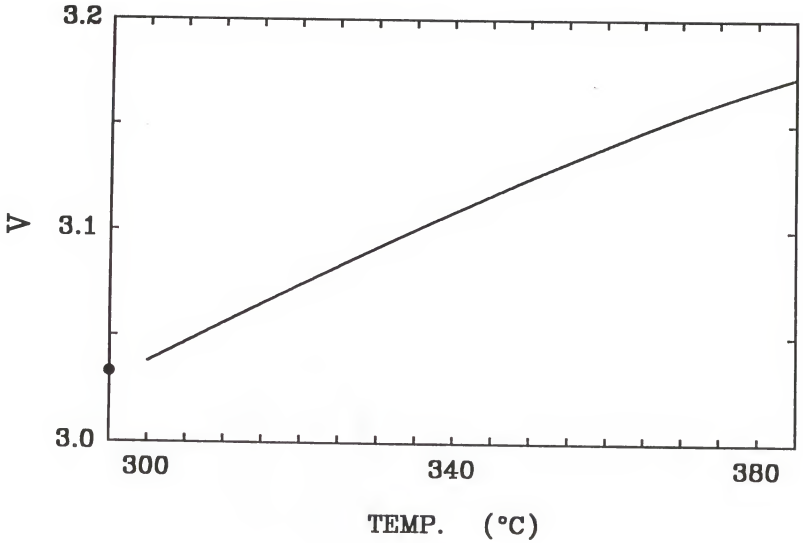

Fig. 5-11. Normalized frequency V vs. the postbaking temperature for the tapered waveguide. The closed circle shows the calculated data before postbaking.

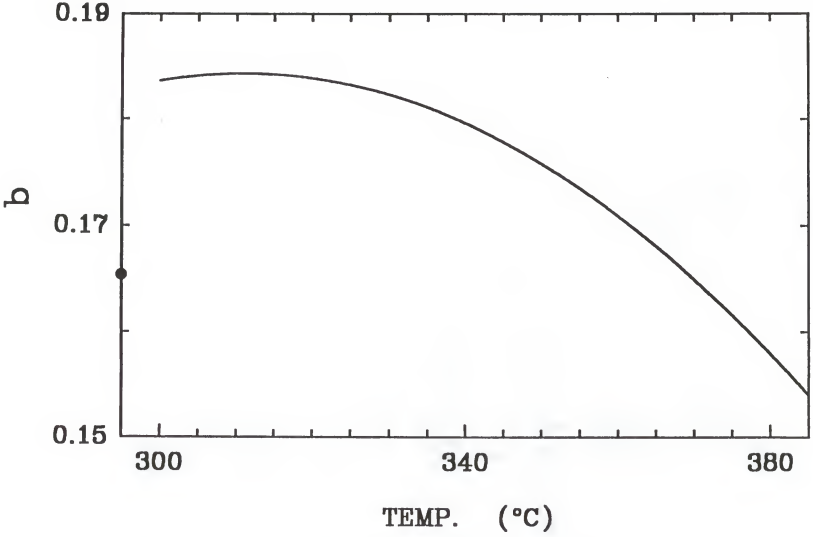

Fig. 5-12. Normalized mode index b vs. the postbaking temperature. The closed circle shows the calculated data before postbaking.

devices *etc.* The horizontal mode size W_h and vertical mode size W_v shown in Fig. 5-13 increase rather rapidly with increasing temperature. The experimental data of Fig. 5-13, denoted by the open squares, were reported elsewhere [Zhen89]. The dark circles represent the simulated modal widths of the channel waveguide prior to postbaking. The taper was sectioned, and the modal width W_h and depth W_v were measured successively at 1 mm intervals over a length of 5 mm where the temperature was raised from 315 to 385°C during postbaking. Figure 5-13 shows that the difference between the numerical simulation and experimental measurement is small. The discrepancy may result from the anisotropic diffusion in the glass and the error in both the numerical calculation and measurements.

5.3. Simulation of Propagation

5.3.1. Beam Propagation Analysis

The index profile of the tapered waveguides is not only a function of x and y as in straight channels but is also a function of z along the propagation direction, which complicates the modeling and increases the computer processing time. To simplify the simulation, it is assumed that its index profile in the lateral or y direction can be converted from a two-dimensional index profile by the effective index method (EIM) to an equivalent 1-D profile and fitted to a gaussian function to simplify the calculation. Although this conversion is not valid for the modes close to cutoff, it may provide us some useful information in designing a taper with minimum radiation loss.

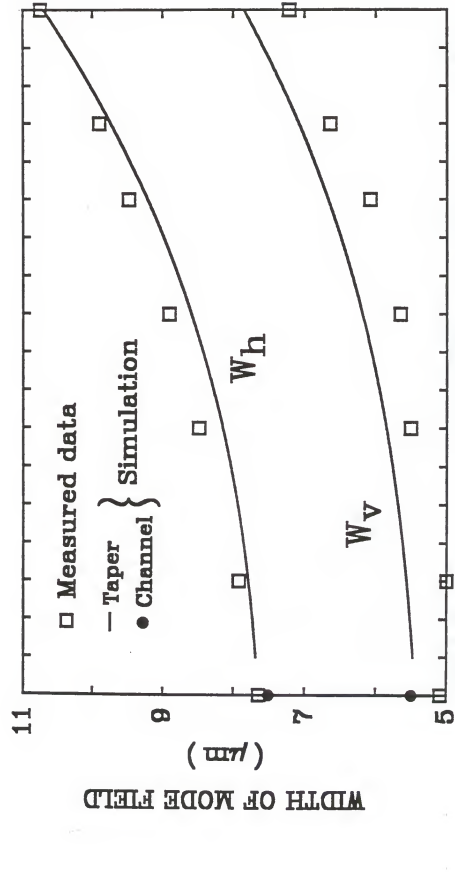

Fig. 5-13. Widths of the mode fields as functions of the postbaking temperature. The solid lines show the simulation results. The open squares denote the data obtained by near field measurement. The closed circle shows the calculated data before postbaking.

After postbaking, the index change profile although broader and weaker, remains gaussian since the initial condition is also gaussian for the case of finite-source diffusion as discussed in chapter 2. The maximum index change Δn_{max} becomes smaller and the half-width W of the index profile at 1/e point in the transverse direction becomes inversely proportional to Δn_{max} due to the constant number of the dopant ions during postbaking. Thus, the index profile can be written as

$$n(y,z) = n_s + \Delta n_{max1} \frac{W_1}{W(z)} \exp\left(\frac{-y^2}{W^2(z)}\right), \qquad (5.2)$$

where n_s is the substrate index, Δn_{max1} is the maximum index change at the beginning of the taper (z=0), W(z) is the half-width of the index profile at the 1/e point, and W_1 is the half-width at input of the taper, *i.e.*, z=0. The width of the index profile can be controlled by varying both the diffusion temperature and the postbaking time as mentioned earlier. We assume that W(z) of the tapered index region ($0 \le z \le L$) can be represented by one of the following functions:

1) linear: $$W(z) = W_1 + (W_2 - W_1)\, z/L \qquad (5.3a)$$

2) quadratic: $$W(z) = \sqrt{W_1^2 + (W_2^2 - W_1^2)\, z/L} \qquad (5.3b)$$

3) raised-sine: $$W(z) = \left[(W_2 + W_1) + (W_2 - W_1) \sin\left[\frac{\pi}{L}\left(z - \frac{L}{2}\right)\right]\right] /2 \qquad (5.3c)$$

where L is the taper length and W_2 is the half-width at the output (z = L).

The simulation of wave propagation in the tapered waveguides is performed by the beam-propagation method. As described earlier, BPM is a unified model for simulating the propagating wave in a graded-index medium. This method can be used to evaluate the magnitude as well as the phase of the wave. However, in the simulation the reflected wave is assumed to be negligible and the field is assumed to vanish at an arbitrary boundary far away from the waveguide region in the transverse direction to avoid the error due to the periodic boundary condition imposed by the fast Fourier transform.

We propagate the field from a straight channel waveguide section of length L_1 (=600 μm) through a tapered transition of length L to another straight section of length L_1. The field launched into the guide is obtained by solving for the eigen-mode of the first section by the finite difference method (FDM) with gaussian index profile. The waveguide is sectioned in the z-direction and the propagating field at the end of each section is calculated using BPM. For evaluating the overlap integral, the mode field at the next section is again calculated using FDM and assuming that the index n(y,z) in the section is invariant in the z-direction and the phase front of the mode field is a plane normal to the z-direction. At the end of each section, we calculate how much power remains in the guided mode by considering the overlap integral η between the mode field and the propagating field for each section along the propagation direction:

$$\eta(z) = \frac{\left| \int_{-\infty}^{\infty} E(y,z)E_0^*(y,z)dy \right|^2}{\int_{-\infty}^{\infty} E_0(y,z)E_0^*(y,z)dy \int_{-\infty}^{\infty} E_1(y,z)E_1^*(y,z)dy}, \qquad (5.4)$$

where E_1 is the initial field at $z = -L_1$, E_0 is the fundamental mode field at the end of a given section z solved by FDM, E is the complex propagating field solved by BPM, and the stars represent the complex conjugate of the fields. This process continues along the z direction till $z = L + L_1$ is reached.

η equals one at the beginning of the input section, *i.e.*, at $z = -L_1$ and decreases due to the radiation in the transition as the wave propagates. A small loss is also encountered at the boundary in the transverse direction where the field is assumed to vanish. The total radiation loss is evaluated from the successive overlap integrals from $z= -L_1$ to $z = L + L_1$.

5.3.2. Simulation Results

Since BPM can track the guided modes as well as the radiation modes, it can be used to simulate abrupt junction transitions, *i.e.*, the length of the taper transition L = 0. The index profile is expressed by Eq. (5.2) with $W_1 = 2.5$ μm at input and $W_2 = 5.0$ μm in the second section of the waveguide. The amplitude of the field along the waveguide for z=0 to L_1 is shown in Fig. 5-14, where the taper length is zero. The mismatch in the mode sizes at the junction (z=0) causes part of the energy of guided wave to be coupled into the radiation

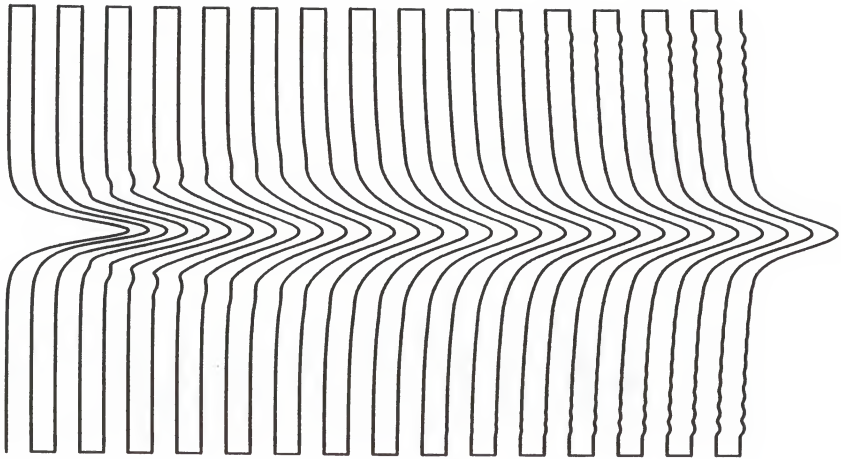

Fig. 5-14. Amplitude of a field propagating through an abrupt junction. The calculation width (vertical) and length (horizontal) are 128 and 600 μm, respectively. The radiation can be clearly seen as side lobes near the main lobe. The ripples shown in the right hand side of this figure are caused by the radiation bouncing back from the boundaries.

mode in the second section as may be seen from the figure. Some ripples of the field appear at the position close to $z = L_1 = 600$ μm indicating that the radiation may bounce back from the boundaries of the calculation. This imposes a limitation on the calculation accuracy. The computation width in this simulation is 128 μm. The width can be increased to avoid the above problem. However, the resolution of the index profile will be reduced if the same number of points is used. The overlap integral η in this case equals 0.9588 equivalent to 0.183 dB loss. Figure 5-15 shows the evolution of the wave propagating in a raised-sine-profile taper with L = 500 μm. The half-width of the index profile increases from 2.5 μm at z = 0 to 5 μm at z = L. The straight section with length of L_1 following the taper is shown in the figure but the preceding straight section ($z < 0$) is ignored. The computation width is the same as Fig. 5-14 and is considerably larger than the mode size of the waveguide. The power loss due to radiation in the taper is small compared to the case in Fig. 5-14 and the radiation field can not be clearly seen from the figure. Figure 5-16 shows the normalized power in the guided mode along the propagation direction for linear (dashed curve) and raised-sine (solid curve) profile. The dotted line represents the half-width of raised-sine-curve index profile and the tapered region is from z=0 to z=500 μm. The linear and parabolic tapered index profile are not shown in the figure. The loss is higher for the linear profile than for the raised-sine profile in the beginning of the taper but it becomes lower at the end since the maximum slope $\partial n(y,z)/\partial z$ is larger for the sine function. The losses are 0.032 dB and 0.056 dB for the linear and raised-sine tapers, respectively, which are much smaller than the loss of abrupt junction.

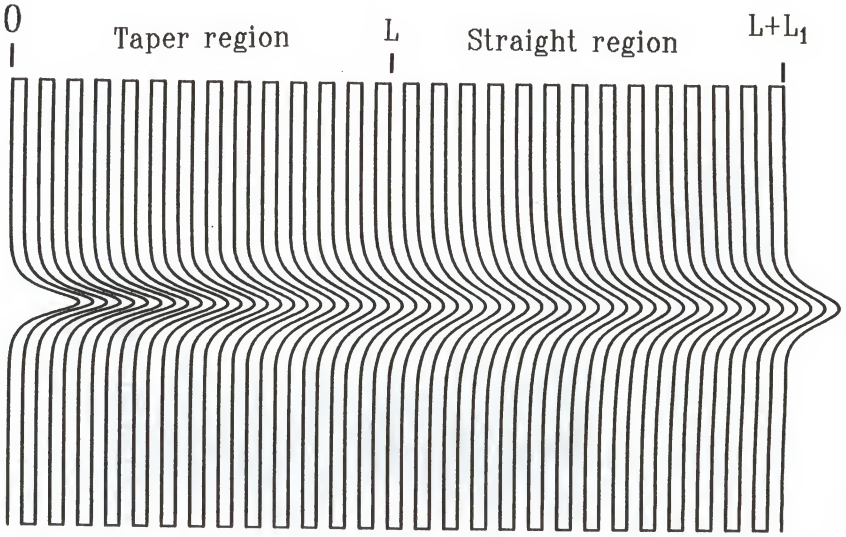

Fig. 5-15. The evolution of the propagating wave in the raised-sine curve taper. The tapered region is between z=0 and L, where L = 500 μm. The length of the straight region is 600 μm.

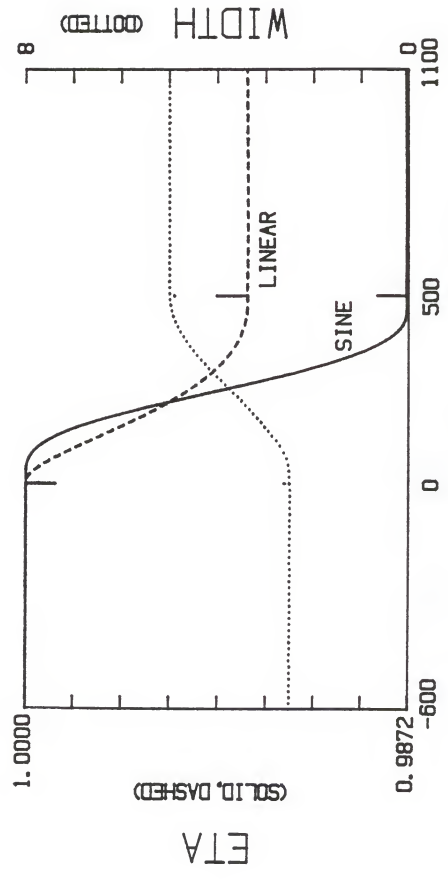

Fig. 5-16. The power in the guided mode along the propagation direction for linear (dashed curve) and raised-sine (solid curve) profile. The dotted line represented the width of raised-sine-curve index profile and the tapered region is from z = 0 to 500 μm.

As a result, tapered transitions always help reduce the mismatch loss. The overlap integral η of the field at z=0 almost equals unity indicating the accuracy of FDM in calculation of the mode field as well as BPM in modeling the wave propagtion since the eigen-mode must remain unchanged and the power should be constant in the straight channel region. Figure 5-17 shows the guided power versus the length of the taper for both the raised-sine (dashed line) and linear (solid line) profiles. The resulting power in the guided mode for a parabolic profile (not shown) is slightly smaller than that for the linear profile. As seen from Fig. 5-17, the loss at the discontinuity of the index gradient in the z-direction between the taper and the input straight channel waveguide becomes dominant as the taper length L increases. As a result, the raised-sine profile suffers less loss than both the linear and parabolic profiles for $L > 1200$ μm. For a raised-sine profile taper longer than 2 mm, the loss is negligible (Fig. 5-17). In the experiments [Zhen89], the radiation loss is smaller than the propagation loss and is below the measurement limit.

5.4. Summary

Channel and tapered waveguides have been simulated in this chapter with the parameters obtained from the planar waveguide modeling. The simulation results are in excellent agreement with the experimental measurements of the mode size as well as index profile width along the taper. The modeling of wave propagation is performed by BPM, which shows that the radiation loss is negligible for a 5 mm long taper.

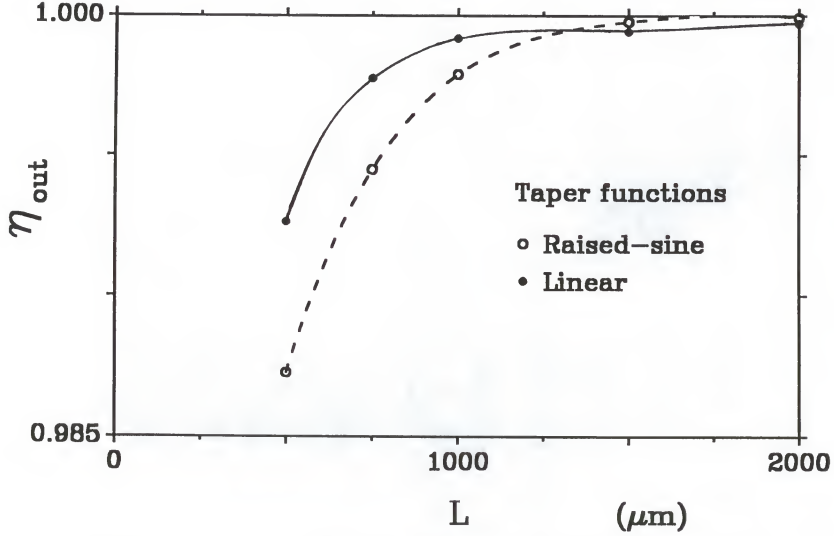

Fig. 5-17. Power output vs. taper length for the linear and raised-sine taper profiles.

CHAPTER 6
DIRECTIONAL COUPLERS AS WAVELENGTH MULTIPLEXERS/DEMULTIPLEXERS

6.1. Introduction

There are several devices which use the directional coupler configuration to perform such roles as optical modulators and switches [Thyl88, Koai86, Koge76], wavelength demultiplexers [Verb88, Suzu89, Chen90b, Chen90e], power dividers [Yip84]. As such directional couplers have very wide applications in the optical communication systems. The guided-wave wavelength division multiplexers/demultiplexers provide opportunities for increasing the transmission capacity of coherent and other fiber-optic systems [Glan90]. The wavelength demultiplexers have been realized by using symmetric directional couplers consisting of two identical straight channel waveguides [Imot87, Suzu89, Chen90e] and asymmetric directional couplers with non-identical guides [Alfe78, Brob86].

In the previous chapter we presented a systematic modeling of index profiles and mode fields for channel and tapered waveguides. In this chapter, we extend these techniques to model symmetric directional couplers in graded-index waveguides as dual wavelength multiplexers/demultiplexers and verify the results by fabricating and characterizing these devices by Ag^+-Na^+ exchange in BK7 glass.

The coupled-mode theory is used for predicting the characteristics of the symmetric directional couplers and the effective

index method is employed to solve the modal properties of both the channel waveguides and the symmetric directional coupler. Modeling results are used to fabricate demultiplexers operating at 1.32/1.56 μm. We achieved a demultiplexer with a propagation loss of 0.15 dB/cm and a total insertion loss of 1.25 dB for a 14.5 mm device with crosstalk of -30 dB and -32 dB at 1.315 and 1.561 μm, respectively. In each case, the modeling results were used to optimize the device performance.

6.2. Coupled-Mode Theory

When two individual waveguides are brought close to each other, the guided modes in the individual waveguides exhibit coupled mode behavior; the propagation characteristics of the coupled-system, *e.g.*, mode field and/or mode index, are altered. When the coupling is "weak", the coupled-mode theory accurately predicts the behavior of the coupled waves as well as the transfer of power between the waveguides along the propagation direction.

The coupled-mode theory was presented by Miller [Mill54] in 1954 for two coupled transmission lines. The theory was applied to optical waveguide to describe guided-wave nonlinear optical interactions, electro-optic switching *etc.* by Yariv [Yari73]. The coupled-mode theory discussed by Miller [Mill54] and Yariv [Yari73] can be applied only to the weakly coupled waveguides *i.e.*, when the separation between the waveguides is relatively large. Suematsu and Kishino [Suem77] treated the case of two strongly coupled waveguides and showed that the degree of power transfer between the waveguides

depends strongly on the coupling strength. As the coupling becomes larger, less power is transferred. Recently, a set of improved or vectorial coupled-mode theories [Marc86a, Chua87a, Chua87b, Haus87a, Stre87a, Stre87b, Vass87, Vass88, Haus89] were reported and experimentally verified [Marc86b]. Most of them are applicable in the case of strong coupling. However, we will consider only the case of weak coupling, since the scalar coupled-mode theory, applicable in this case, is easy to use and gives sufficiently accurate results.

6.2.1. Coupled-Mode Theory

Suppose we have two weakly coupled waveguides. The fields in the waveguides propagating in the z-direction in the composite structure can be expressed as

$$F_i(y, z) = a_i(z)\, f_i(y)\, \exp(-j\beta_i z)\ , \qquad (6.1)$$

where the subscripts i (=1 or 2) represent one of the waveguides; a(z) is the complex amplitude of the field; $f_i(y)$ is the mode field of the waveguide i with the propagation constant β_i and y is the transverse direction. The fields are normalized such that the power carried by each waves are given by $a_i\, a_i^*$ (i=1 or 2), where the superscript * represents the complex conjugate. In the uncoupled case, the guided modes must maintain the same power in the waveguides; a_i's are z-independent constants. Otherwise, the z-dependent amplitudes (a_1 and a_2) obey the following relations [Yari73]:

$$\frac{d a_1}{d z} = -j\kappa_{21} a_2 \exp(-2j\,\delta z)$$

and

$$\frac{d a_2}{d z} = -j\kappa_{12} a_1 \exp(+2j\,\delta z)\,, \tag{6.2}$$

where $\delta = (\beta_2-\beta_1)/2$ and κ_{12} and κ_{21} are the coupling coefficients, given by [Lee86]

$$\kappa_{21} = \frac{\omega}{2}\int_{-\infty}^{\infty} (\sqrt{n(y)} - \sqrt{n_1(y)})\,(f_2 f_1^*)\,dy$$

and

$$\kappa_{12} = \frac{\omega}{2}\int_{-\infty}^{\infty} (\sqrt{n(y)} - \sqrt{n_2(y)})\,(f_1 f_2^*)\,dy\,, \tag{6.3}$$

where ω is the angular frequency, n(y) is the index of the entire (composite) waveguide system and $n_i(y)$ are the index of the uncoupled waveguides. In general, κ_{12} is not equal to κ_{21} [Hard85, Marc86a, Marc86b]. Nevertheless, when the guides are close to synchronism ($\delta \equiv 0$) and/or far apart (weak coupling), the relation $\kappa_{12} = \kappa_{21}$ is reasonably satisfied. For the boundary conditions: $a_1(z=0) = A_0$ and $a_2(z=0) = 0$, the solutions of Eq. (6.2) are given by [Lee86, Koge88]

$$a_1(z) = A_0\left[\cos(Kz) + \frac{j\delta}{K}\sin(Kz)\right]\exp(-j\delta z)$$

$$a_2(z) = A_0\left[\frac{-j\kappa_{12}}{K}\sin(Kz)\right]\exp(+j\delta z)\,, \tag{6.4}$$

where A_0 is a constant, $K = \sqrt{\delta^2+\kappa_{12}\kappa_{21}}$ and $\delta = (\beta_2-\beta_1)/2$. In the case of a coupler with two identical waveguides, $\delta = 0$,

$$\kappa_{12} = \kappa_{21} = \kappa \,, \tag{6.5}$$

and $K = \kappa$. Therefore, the complex amplitudes are given by

$$\begin{aligned} a_1(z) &= A_0 \cos(\kappa z) \\ a_2(z) &= -jA_0 \sin(\kappa z) \,, \end{aligned} \tag{6.6}$$

Notice that the fields in the individual waveguides have a $\pi/2$ phase difference. The normalized powers in the individual waveguides are expressed as

$$\begin{aligned} P_1 &= \frac{a_1 a_1^*}{A_0^2} = \cos^2(\kappa z) \\ P_2 &= \frac{a_2 a_2^*}{A_0^2} = \sin^2(\kappa z) \,. \end{aligned} \tag{6.7}$$

Thus, the power propagating along a symmetric coupler is transferred back and forth sinusoidally between the two waveguides. The normalized power is unity in waveguide 1 and zero in waveguide 2 at $z = 0$ and power transfers completely to waveguide 2 at $z = \pi/(2\kappa)$. The interaction length required to have complete power transfer is defined as the coupling length $l_c = \pi/(2\kappa)$. Equation (6.6) can be rewritten in terms of l_c as

$$\begin{aligned} a_1(z) &= A_0 \cos(\frac{\pi}{2 l_c} z) \\ a_2(z) &= -jA_0 \sin(\frac{\pi}{2 l_c} z) \,. \end{aligned} \tag{6.8}$$

3 dB power divider is achievable for the interaction $L = \frac{l_c}{2}$ or $\frac{\pi}{4\kappa}$. In this case the power is equally split at the output.

Since the individual waveguides are identical, the phase matching condition is always satisfied at all wavelengths for the symmetric directional coupler. However, this does not mean the bandwidth for complete power transfer is infinite. The limitation on bandwidth is imposed by the wavelength-dependent coupling coefficient and coupling length as will be discussed later. As a result, waves of different wavelengths are split at the output of the directional coupler.

6.2.2. Relation between Normal-Modes and Coupled-Modes

Coupled-mode theory solves the coupled system in terms of the eigen-modes of individual waveguides and the coupling coefficients between them. However, it is valid only in the case of weak coupling. On the other hand, the normal-mode approach solves the eigen-modes of the entire waveguide system. Therefore, this approach is applicable for the cases of arbitrary coupling. If the waveguides are weakly coupled, the eigen-solutions of the normal modes can be expressed in terms of that of the coupled-mode and the coupling coefficients.

Consider a symmtric directional coupler consisting of two single-mode waveguides. We define a normal-mode field F^o as a linear combination of the uncoupled mode fields as follows:

$$F^o(y,z) = A_1(z)f_1(y)e^{-j\beta_1 z} + A_2(z)f_2(y)e^{-j\beta_2 z}, \qquad (6.9)$$

where A_1 and A_2 are functions of z. Since F^o is the normal-mode field, it follows the relation

$$F^o(y,z) = Af^o(y)e^{-j\beta^o z}, \qquad (6.10)$$

i.e.,
$$\frac{dF^o}{dz} = -j\beta^o F^o , \tag{6.11}$$

where A is a constant, $f^o(y)$ is the transverse normal-mode field, and β^o is the propagation constant corresponding to that normal mode. Substituting Eq. (6.9) into (6.11), one obtains

$$f_1 \left(\frac{dA_1}{dz} - j\beta A_1 + j\beta^o A_1\right) + f_2 \left(\frac{dA_2}{dz} - j\beta A_2 + j\beta^o A_2\right) = 0 , \tag{6.12}$$

where we have assumed a symmetric directional coupler, *i.e.*, $\beta = \beta_1 = \beta_2$. In the above equation, only f_1 and f_2 are functions of y. Therefore, for nonzero f_1 and f_2, Eq. (6.12) can be written as two separate equations:

$$\begin{aligned} \frac{dA_1}{dz} - j\beta A_1 + j\beta^o A_1 &= 0 \\ \frac{dA_2}{dz} - j\beta A_2 + j\beta^o A_2 &= 0 . \end{aligned} \tag{6.13}$$

Applying the coupled-mode equation Eq. (6.2) for A_1 and A_2 in this case, Eq. (6.13) can be written as

$$\begin{aligned} -j\kappa A_2 - j\beta A_1 + j\beta^o A_1 &= 0 \\ -j\kappa A_1 - j\beta A_2 + j\beta^o A_2 &= 0 \end{aligned}$$

or
$$\begin{aligned} (-\beta + \beta^o) A_1 - \kappa A_2 &= 0 \\ -\kappa A_1 + (-\beta + \beta^o) A_2 &= 0 . \end{aligned} \tag{6.14}$$

For nontrivial solutions for $A_1(z)$ and $A_2(z)$,

$$\begin{vmatrix} -\beta + \beta^o & -\kappa \\ -\kappa & -\beta + \beta^o \end{vmatrix} = 0 , \tag{6.15}$$

i.e.,
$$\beta^o = \beta \pm \kappa , \tag{6.16}$$

which relates the propagation constants of the two normal modes to those of the individual waveguide modes. The propagation constants of the fundamental (even) and the first-higher (odd) normal modes are thus given by

$$\beta^+ = \beta + \kappa \qquad (6.17)$$

and

$$\beta^- = \beta - \kappa \,,$$

respectively. When the separation of the waveguides is large, the coupling is weak and β^+ and β^- are close to the propagation constant of uncoupled mode (β). As the separation decreases, the coupling becomes stronger and, as a result, β^+ increases and β^- decreases. It must be pointed out that Eq. (6.17) is not applicable in the strong coupling case since in this case, the normal mode description given by Eq. (6.9) is not valid. Note that the coupling coefficient $\kappa = (\beta^+ - \beta^-)/2$. For the symmetric directional coupler, Eq. (6.6) can, thus, be expressed as

$$\begin{aligned} a_1(z) &= A_0 \cos\left(\frac{\beta^+ - \beta^-}{2} z\right) \\ a_2(z) &= -jA_0 \sin\left(\frac{\beta^+ - \beta^-}{2} z\right). \end{aligned} \qquad (6.18)$$

The relations between A_1 and A_2 are obtained by substituting Eq. (6.16) into Eq. (6.14) as

$$A_1(z) = A_2(z) \qquad \text{for } \beta^+ = \beta + \kappa, \qquad (6.19)$$

and

$$A_1(z) = -A_2(z) \qquad \text{for } \beta^- = \beta - \kappa \,.$$

Applying Eq. (6.2) again, we have

$$\frac{dA_1}{dz} = -j\kappa A_1 \qquad \text{for } \beta^+$$
$$\frac{dA_1}{dz} = j\kappa A_1 \qquad \text{for } \beta^- , \tag{6.20}$$

which have solutions

$$A_1(z) = A_0 \exp(-j\kappa z) \qquad \text{for } \beta^+$$
$$A_1(z) = A_0 \exp(j\kappa z) \qquad \text{for } \beta^- , \tag{6.21}$$

where A_0 is constant. The normal mode fields for the fundamental and first higher modes are obtained by substituting Eq. (6.21) into Eq. (6.9) as

$$F^+(y,z) = A_0 \left[f_1(y)+f_2(y)\right] e^{-j\beta^+ z} \equiv A_0 f^+(y) e^{-j\beta^+ z} \tag{6.22a}$$

and

$$F^-(y,z) = A_0 \left[f_1(y)-f_2(y)\right] e^{-j\beta^- z} \equiv A_0 f^-(y) e^{-j\beta^- z} , \tag{6.22b}$$

respectively. Equation (6.22a) depicts that the fundamental normal mode field (f^+) of the symmetric directional coupler can be expressed as an in-phase superposition of the two individual mode fields f_1 and f_2 with equal amplitudes. Similarly, Eq. (6.22b) depicts that the first order normal mode field (f^-) is an out of phase superposition of the two individual mode fields.

Figure 6-1 shows a schematic of a directional coupler consisting of two identical straight channel waveguides, where S is the separation between two channel waveguides measured from the center of one waveguide to that of the other and W_M is the width of the mask opening. The mode fields are shown in the figure marked as β, β^+ and β^-, representing the fundamental mode of the individual waveguides,

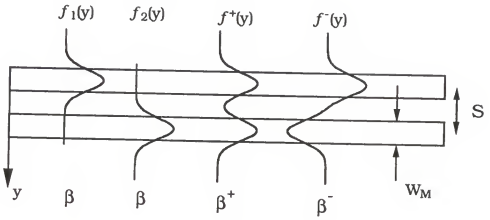

Fig. 6-1. Uncoupled and normal modes of a symmetrical directional coupler. Notations are defined in the text.

and the fundamental and first order mode of the directional coupler, respectively. It is obvious that $f^+(y)$ is the summation of the individual mode fields $f_1(y)$ and $f_2(y)$; $f^-(y)$ is the difference of $f_1(y)$ and $f_2(y)$. Conversely, in the case of weak coupling, the mode fields of the individual waveguides can also be written as a summation or difference of two normal modes of the entire structure by using Eq. (6.22) and (6.10). Substituting '+' or '-' into the superscript 'o' in Eq. (6.10), we obtain $f_1(y) = \frac{A}{2A_0}(f^+(y)+f^-(y))$ and $f_2(y) = \frac{A}{2A_0}(f^+(y)-f^-(y))$. In other words, the wave input from one of the waveguides can be decomposed into two normal modes with equal powers. These two normal modes, having different phase velocities or propagation constants, interfere with each other as they propagate along the directional coupler. If the total energy launched into one of the guides is coupled equally to these two normal modes, the energy transfers to the other channel at a distance where the difference in phases of the two normal modes is $(2m-1)\pi$, where m is a positive integer. If the phase difference is $2m\pi$, the energy shifts back to the original channel. The coupling length l_c is the length required to achieve a relative phase shift π between two normal modes propagating along the directional coupler and is given by $l_c = \pi/(\beta^+-\beta^-) = \pi/(2\kappa)$. Therefore, if the interaction length (L) of the directional coupler equals an odd number of coupling lengths, the superposition of the normal modes yields complete energy transfer . Similarly, power transfer back to the original waveguide occurs when L equals an even number of coupling lengths. We do not consider the case of strong coupling since complete power transfer between the two identical waveguides of the coupler is not possible [Suem77].

6.3. Modeling

In this section we present and discuss the results of the modeling of the index profile, and design considerations for directional coupler as a wavelength demultiplexer. The results are verified by fabrication and characterization of symmetric directional-coupler devices as described later.

6.3.1. Index Profile

It is well known that in graded index waveguides, the modal profile is somewhat insensitive to the index profile [Rama83]. However, the index profile affects the dispersion relation as well as the propagation constant. A knowledge of the index profile prior to the simulation of waveguides is of paramount importance. In the case of silver ion-exchanged waveguides in BK7 glass, the simulation, presented in the last chapter, shows a gaussian-like index profile. Thus, we assume that the index profile of the channel is a semi-infinite gaussian function in the depth direction. The assumption of a gaussian index profile in our model is also applicable to some other cases, for example, K^+-Na^+ exchanged waveguides in soda-lime glass [Mili89].

Since the diffusion is isotropic in the width (horizontal) direction as well as in the depth (vertical) direction, the index profile in the horizontal direction is also assumed to be Gaussian in shape. In the case of channel waveguides, this is especially true if the dimension of the diffused profile in the horizontal direction is much larger than the width of the mask opening. Hence, the contours of equal

concentrations are semicircles. The assumption is reasonable in the case of Ag^+-Na^+ exchange in BK7 [Chen90a] also, as evidenced by the excellent correlation between the theoretical and experimental results presented later. Based on the above assumptions, the equation for the 2-D index profile is given by

$$n(x, y ; \lambda) = n_b(\lambda)+\Delta n_{max} \exp\left(- \frac{x^2+y^2}{W^2}\right), \quad \text{for } x \geq 0 \qquad (6.23)$$

where $x = 0$ represents the surface, λ is the wavelength in vacuum, $n_b(\lambda)$ is the wavelength-dependent substrate index, Δn_{max} is the maximum index change of the guide and W is the half-width of the channel waveguide at the 1/e point. In the simulation, the dispersion or the wavelength-dependent index of the substrate glass is taken into account. However, the maximum index change Δn_{max} is assumed to be constant in the operating wavelength region. This assumption is acceptable as long as no absorption occurs in the wavelength region of interest (1.2-1.6 μm), due to the incorporation of the diffusing ions, thereby causing a resonant behavior of the refractive index.

The directional coupler consists of two identical channel waveguides with separation S, as shown in Fig. 6-1. Therefore, the index profile of this structure is a summation of index profiles of the individual straight channels given by

$$n(x, y ; \lambda) = n_b(\lambda)+\Delta n_{max} \exp\left(- \frac{x^2+(y-S/2)^2}{W^2}\right) + \Delta n_{max} \exp\left(- \frac{x^2+(y+S/2)^2}{W^2}\right). \qquad (6.24)$$

Such a superposition of individual waveguide index profiles has been verified in Ti indiffused $LiNbO_3$ directional coupler [Noda81] and validated the use of the above index profile in the modeling of ion-exchanged directional couplers presented in this chapter.

6.3.2. Numerical Method

The effective index method (EIM) along with the 1-D matrix method are used to solve the mode indices in the modeling of directional couplers. The effective index method and matrix method were described in chapter 3 for graded-index channel waveguides. The effective index method is used to convert a 2-D index profile into its 1-D equivalent index profile, while the matrix method is used to solve mode indices of the equivalent profile. In the case of directional couplers, the same approach can be employed. We first calculate the mode index of the individual channel waveguide and next evaluate the normal mode indices of the directional coupler. As addressed earlier, the mode index of the fundamental normal mode of the coupler is slightly larger than the mode index of the individual waveguides and that of the first order normal mode is slightly smaller. The information obtained from the evaluation of the mode index of the channel is useful to estimate the mode indices of the directional coupler since the initial guess is reasonably close. Therefore, considerable CPU time can be saved in the modeling.

6.3.3. Directional Coupler

The coupling length l_c of the directional coupler equals $\pi/(\beta^+-\beta^-)$ or $0.5\lambda/(N^+-N^-)$, where N^+ and N^- are the normal mode indices of the fundamental and first higher modes of the directional coupler, respectively. The coupling length is evaluated by the normal-mode approach $[l_c=\pi/(\beta^+-\beta^-)]$ instead of the coupled-mode approach $[l_c=\pi/(2\kappa)]$ with κ evaluated by Eq. (6.3) since the latter involves an overlap integral of the individual mode fields which requires more CPU time.

The normalized power outputs P_1 and P_2 defined in Eq. (6.7), assuming power is launched into channel 1 at $z = 0$, can be rewritten in terms of the coupling length as

$$P_1(\lambda) = \cos^2\left(\frac{\pi L}{2l_c(\lambda)}\right)$$

and

$$P_2(\lambda) = \sin^2\left(\frac{\pi L}{2l_c(\lambda)}\right), \qquad (6.25)$$

respectively, where $z = L$ is the interaction length. Note that P_1 and P_2 as well as the coupling length are functions of wavelength since the coupling is wavelength-dependent. If the length L is not exactly equal to $(2m-1)\,l_c$, the power is not quite zero at port 1. This cross power ratio represents the nonzero output from port 1, normalized to P_2. From the above equations, the cross-power ratio in dB can be shown to be

$$10 \log \zeta_1 = 10 \log \frac{P_1}{P_2} = 10 \log\left(\left(\frac{\pi \Delta L}{2 l_c}\right)^2\right), \qquad (6.26)$$

where $\Delta L = L-(2m-1)\,l_c$, is the small deviation from the exact length required to accomplish complete transfer of power. For example, for a

coupling length of 5.4 mm, to achieve a cross power ratio of -30 dB and -40 dB, the fabrication error in the device length must be within ±109 μm and ±34 μm, respectively. Similarly, for L close to an even number of coupling length, the cross power ration at port 2 is

$$10 \log \zeta_2 = 10 \log \frac{P_2}{P_1} = 10 \log \left(\left(\frac{\pi \Delta L}{2 l_c} \right)^2 \right), \qquad (6.27)$$

where $\Delta L = L - 2m\, l_c$. Note that in Eqs. (6.26) and (6.27), although ΔL is the same, the associated L's are different.

The spectral bandwidth at the operating wavelength λ_o, derived from Eq. (6.25) by the perturbation theory, for a given cross power ratio ζ_i (caused by the deviation in wavelength) at port i, is

$$2\,\Delta\lambda = \left| 4\, l_c(\lambda_o) \sqrt{\zeta_i} \Big/ m\pi \left(\frac{dl_c}{d\lambda} \right) \Big|_{\lambda = \lambda_o} \right| \qquad m=1,2,... \quad (6.28)$$

For example, in the specific case considered in the following section, with $\lambda_o = 1.3$ μm, L equals to 5.4 mm (one coupling length), and assuming a reasonable value for the derivative, $\frac{dl_c}{d\lambda} = -0.022$ mm/nm (as seen from Fig. 6-10 described later), the spectral bandwidth for a specified cross power ratio of -20 dB and -30 dB into port 1, must be within 31 nm and 9.9 nm, respectively. A larger bandwidth can be obtained by designing the device with minimum m as well as longer l_c and smaller $\frac{dl_c}{d\lambda}$. However, for a fixed m, the bandwidth at each channel is almost independent of the two center wavelengths of the demultiplexer and increases with increasing separation of the two wavelengths. For asymmetric directional couplers used as wavelength

demultiplexers, the bandwidth required to achieve a given transmission level (-20 or -30 dB) is much smaller [Marc87].

6.3.4. Design of Dual-Wavelength Demultiplexers

As discussed earlier, the coupling length l_c is wavelength-dependent. At longer wavelengths l_c decreases due to stronger coupling between the modal fields. For a given interaction length L, the wavelength-dependent behavior of l_c results in different amounts of power being transferred at different wavelengths to the output ports. As shown in Fig. 6-2, for dual wavelength demultiplexing, we require complete power transfer to port 2 at wavelength λ_1 and to port 1 at wavelength λ_2. In general, the number of coupling lengths in the region of interaction must be an odd number for λ_1 and an even number for λ_2. In other words, it is required that $(2m_1\text{-}1)\, l_c(\lambda_1) = 2m_2\, l_c(\lambda_2)$, where m_1 and m_2 are positive integers.

In designing the demultiplexer, we define a parameter R as the ratio of the normal mode ΔN's at the two operating wavelengths. From the relation in the last section, the ratio, for splitting 1.3 and 1.55 μm, is

$$R \equiv \frac{\Delta N(1.55\ \mu m)}{\Delta N(1.3\ \mu m)} = \frac{1.55\, l_c(1.3\ \mu m)}{1.3\, l_c(1.55\ \mu m)}. \qquad (6.29)$$

Notice that $l_c(1.3\mu m)$ is always greater than $l_c(1.55\mu m)$. Hence, R is larger than 1.19. Many values of R can meet the requirement of a 1.3/1.55 μm wavelength demultiplexer as shown in Table 2, where

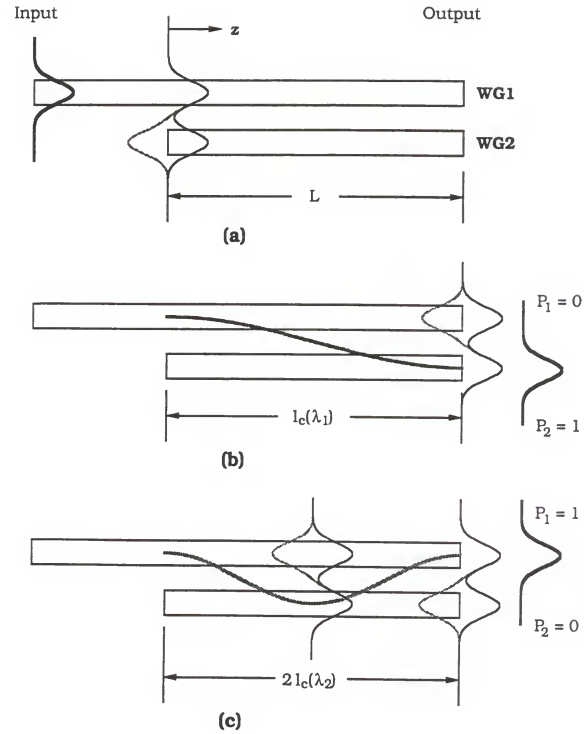

Fig. 6-2. The operating principle of DEMUX. (a) Wave input from WG1 is decomposed into two normal modes. (b) The energy transfers to WG2 for one coupling length at λ_1. (c) The energy transfers back to WG1 for two coupling lengths at λ_2.

Table 2

Ratio of coupling length vs. R

$l_c(1.3\mu m):l_c(1.55\mu m)$	R
2:1*	2.385
3:2	1.788
4:3*	1.590
4:1*	4.769
5:4	1.490
5:2	2.981

* 1.3μm wavelength output at port 2, otherwise at port 1

only six of the many possible pairs are listed. To obtain complete transfer of power in the case of weak coupling, usually l_c (and, hence, L) is rather long; this results in higher propagation loss and is, therefore, not practical. The minimum length of the device operating at 1.3/1.55 μm is achieved when the interaction length L equals one coupling length at 1.3 μm and two coupling lengths at 1.55 μm so that the ratio R equals 2.385.

If R deviates from the optimized value in the fabrication, the performance of the wavelength demultiplexer will be degraded and, thus, the output port 1 or port 2 may have energy at both wavelengths. The crosstalk ratios for port 1 are

$$\chi_1 = \frac{P_1(1.3\,\mu m)}{P_1(1.55\,\mu m)} \tag{6.30}$$

and for port 2

$$\chi_2 = \frac{P_2(1.55\,\mu m)}{P_2(1.3\,\mu m)}\,. \tag{6.31}$$

where P_1 and P_2 are expressed in Eq. (6.25). Predicting by the coupled-mode theory, both χ_1 and χ_2 are zero for perfect demultiplexing at 1.3 and 1.55 μm. However, fabrication error is inevitable, causing the ratio R to depart from the optimized value. Three cases are considered for the estimation of the crosstalk ratio χ in terms of ΔR and ΔL, where it is assumed that $R = R_o+\Delta R$ with ΔR being small compared to the desired $R_o(=2.385)$ and $\Delta L = L - l_{co}(1.3\mu m)$ or $L- 2\, l_{co}(1.55\mu m)$. The subscript 'o' represents the reference values for the demultiplexer in question, with no deviation. The same notation is used in the following discussion of a demultiplexer operating at the wavelength 1.3/1.55 μm. We have

omitted the units of the wavelength, *viz.*, μm, for the sake of convenience.

Case 1: $L = 2\,l_c(1.55) = 2\,l_{co}(1.55)$ and $l_c(1.3) = l_{co}(1.3)+\Delta l_c$, where Δl_c is rather small compared to $l_{co}(1.3)$. In this case, $\chi_2 = 0$ since L equals exactly twice the coupling length at 1.55 μm. However, χ_1 in Eq. (6.30) is not zero and is approximately equal to $P_1(1.3)$. From Eq. (6.25), we find

$$\chi_1 = \cos^2\left(\frac{\pi}{2+\frac{\Delta l_c}{l_c(1.55)}}\right). \tag{6.32}$$

With some mathematical manipulation from Eq. (6.29), the deviation ΔR can be expressed as

$$\Delta R = R_o\frac{\Delta l_c}{l_{co}(1.3)} = R_o\frac{\Delta l_c}{2\,l_{co}(1.55)}. \tag{6.33}$$

From the above two equations eliminating Δl_c, the crosstalk ratio χ_1 is obtained, for small deviation ΔR, in terms of the ratio of $\frac{\Delta R}{R_o}$ as

$$\chi_1 = \frac{\pi^2}{4}\left(\frac{\Delta R}{R_o}\right)^2. \tag{6.34}$$

According to the above equation, the change in R must be kept within ±2% in order to achieve a crosstalk ratio of -30 dB and ±0.64% for -40 dB.

Case 2: $L = l_c(1.3) = l_{co}(1.3)$ and $l_c(1.55) = l_{co}(1.55)+\Delta l_c$, where Δl_c is small compared to $l_{co}(1.55)$. χ_1 is, now, zero for $L = l_c(1.3)$.

Following a similar derivation procedure as used in the previous case, we obtain an expression for χ_2:

$$\chi_2 = \pi^2 \left(\frac{\Delta R}{R_o}\right)^2 . \tag{6.35}$$

The crosstalk is worse by a factor of four since the coupling length for 1.3 μm is twice that for 1.55 μm for the same interaction length thus imposing a stricter requirement on R. In this case, to achieve a crosstalk ratio less than -30 dB and -40 dB, the error in R must be controlled within ±1% and ±0.32%, respectively.

Case 3: $R = R_o$ and $L = l_{co}(1.3)+\Delta L = 2\, l_{co}(1.55)+\Delta L$, where ΔL is a small deviation in the interaction length. With similar derivation procedure, the crosstalks at port 1 and port 2 are

$$\chi_1 = \frac{\pi^2}{4}\left(\frac{\Delta L}{L_o}\right)^2 \tag{6.36}$$

and

$$\chi_2 = \pi^2 \left(\frac{\Delta L}{L_o}\right)^2 , \tag{6.37}$$

respectively, where L_o equals $l_{co}(1.3) = 2l_{co}(1.55)$. Note that the crosstalk in this case is different from the cross power ratio defined in last subsection; the crosstalk is the power ratio at the same output port between two different wavelengths while the cross power ratio is the power ratio at the same wavelength between two ports. Comparison of Eqs. (6.26) ($l_c=L_o$ at 1.3 μm) and (6.27) ($2l_c=L_o$ at 1.55 μm) with Eqs. (6.36) and (6.37) shows that cross power ratio is essentially the same as the crosstalk as

long as the normalized power transferred at a given wavelength approaches unity.

6.3.5. Numerical Results

The fundamental mode index of the channels with mask width $W_M = 3.5$ μm, calculated by the effective index method with two fitting parameters Δn_{max} and W, is shown in Fig. 6-3. For this case, $\Delta n_{max} = 0.0116$ and $W = 4.9$ μm are values that best fit the experimental data of N as well as the measured coupling length, which will be presented in section 6.5. The two open squares denote the measured mode indices of the channel waveguide by the prism coupler technique using the laser diode sources available in our laboratory. The dashed line represents the calculated fundamental mode index as a function of wavelength. The solid line represents the commercial BK7 substrate index. The simulation data agree well with the experimental results for the above mask width. The figure also shows that the mode indices N are much larger than the substrate index and hence the fundamental mode is well-confined in the wavelength range 1.3-1.6 μm.

For different mask opening, W has different values and increases with increasing mask opening while, as expected, Δn_{max} remained essentially unchanged. The single-mode wavelength regime, for $W_M = 3.5$ μm, is from 1200 nm to at least 1600 nm since the fundamental mode cutoff wavelength is larger than our measurement limit (1.6 μm). The horizontal width ($2W \cong 10$ μm) of the waveguide is approximately three times larger than the mask opening W_M, indicating the validity

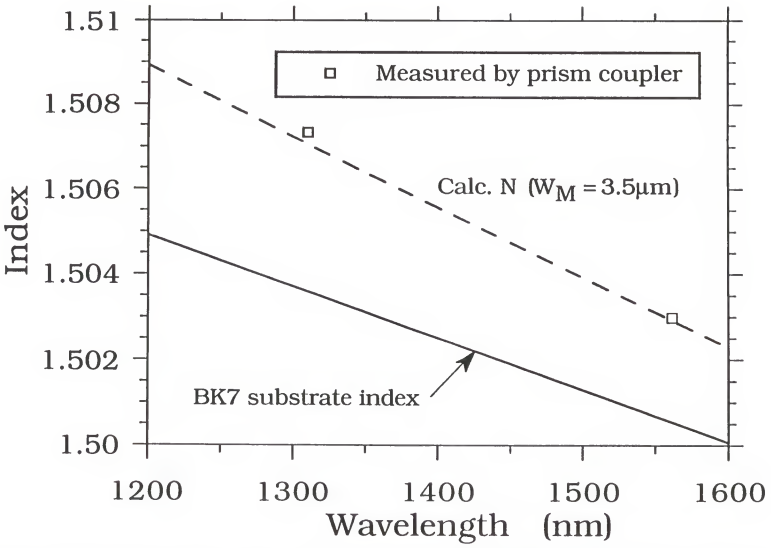

Fig. 6-3. The refractive index as a function of wavelength. The solid line represents BK7 substrate index. The dashed line represents the calculated fundamental mode index of channel waveguide with mask opening of 3.5 μm. The open squares are the measured mode indices of the channel using the prism coupler technique. The waveguide were produced by diffusing for 12 hours at 350°C.

of the assumption of simicircular gaussian index profile. Both Δn_{max} and W (for a given W_M) obtained from the simulation of the channel waveguide are used in the modeling of the directional coupler.

As described earlier, the normal mode indices of the directional coupler are evaluated by the effective index method. It is well known that the method is not very accurate in estimating the mode indices, especially in the region close to cutoff. However, the coupling length, determined by the normal mode approach, is found to be sufficiently accurate since it is evaluated by the difference the two normal mode indices. Hence, R can be evaluated from Eq. (6.29) once the coupling lengths at two operating wavelengths are known. Since the ratio R is critical in determining the performance of the demultiplexer, to arrive at the correct value of R, several device parameters such as the interaction length L, the separation S, the maximum index change Δn_{max} and the waveguide size can be adjusted at will so that the crosstalk may be minimized.

Figure 6-4 shows the ratio R as a function of the half-width (W) of waveguide for different values of S in the range 11.65 to 12.2 μm while Δn_{max} is kept constant at 0.0116. The curves shift downward as the separation S decreases. The horizontal dashed line marked as '1.3/1.55' denotes the value of R=2.385. The intersection points between the horizontal dashed line and the curves represent the exact operating points of the demultiplexer at 1.3/1.55 μm. The bottom curve with S = 11.65 μm has no interaction point, indicating that the two-to-one ratio of the coupling lengths at 1.3/1.55 μm is not attainable. Therefore, in this case, we need to consider cases with R values less than 2.385 (Table 2). Obviously, as the interaction length of

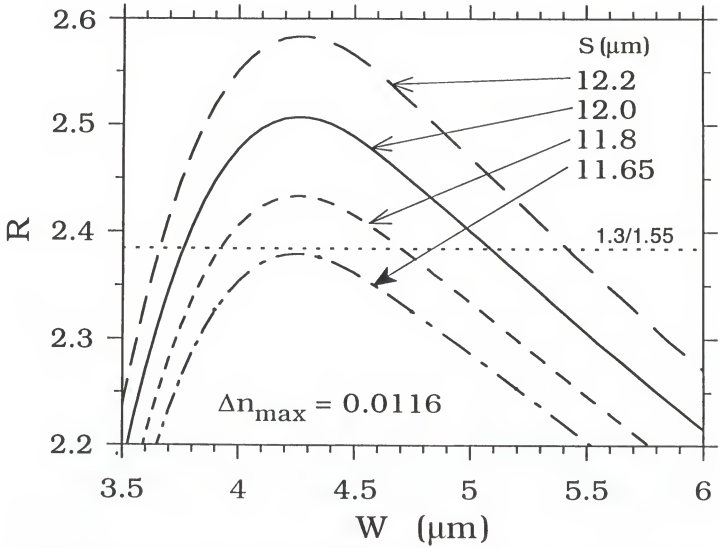

Fig. 6-4. Calculated R as a function of the waveguide half-width W for Δn_{max}=0.0116. The dotted line represents the ratio R equal to 2.385. The behavior of R is illustrated for varying values of the separation S = 12.2 μm (long dashed), 12.0 μm (solid), 11.8 μm (short dashed), and 11.65 μm (dotted-dashed).

the directional coupler becomes longer, the associated insertion loss increases while the spectral bandwidth decreases. For the shortest device, S ≡ 11.65 μm appears to be the lower limit in the case of Δn_{max} = 0.0116. As seen from the figure, for a given S, there are two different intersection points and, therefore, the desired value of R is obtained for two different waveguide sizes. Either intersection point can be chosen as long as the coupling remains weak and the individual channel is single-moded at both wavelengths. For a given Δn_{max}, at small values of W, the mode approaches cutoff and the coupling becomes stronger. With larger values of W, the waveguide may become multimoded. Increasing S shifts the curve upward and the separation between the two intersection points increases. As S increases, the intersection point on the right hand side moves toward the larger width of the waveguide, where the channel may become multimoded at shorter wavelength. On the other hand, the other intersection point shifts at a slower rate to the left and approaches the fundamental mode cutoff at longer wavelength, where the coupling becomes quite strong. The simulation shows that the channel becomes multimoded for the waveguide half-width greater than 5.5 μm at 1.3 μm wavelength with Δn_{max} = 0.0116. In the case of S greater than 12.2 μm, with R = 2.385, the waveguide becomes either multimoded for large width corresponding to the intersection point at right or the coupling becomes stronger for small width on the other side. Hence, the upper limit of S is 12.2 μm. Thus, S must be within a restricted range of 11.65 μm and 12.2 μm for Δn_{max}=0.0116.

The magnitude of the slope in the curve represents the sensitivity of the ratio R to the changes in the waveguide size. As the

magnitude increases, the sensitivity increases, implying that the fabrication tolerance is more restrictive. For S = 12 μm and a 0.05 μm change in half-width W, the relative change in R, *i.e.*, $\Delta R/R_o$, is 1.1% and 0.97% for the intersection points on the left and the right hand side, respectively, corresponding to the crosstalk ratio χ_2 of -29 dB and -30 dB. However, the fabrication tolerances are not so severe, if the intersection point is exactly located at the zero-slope point with S slightly greater than 11.65 μm and W equal to 4.25 μm. In the case of weak coupling, note that the zero-slope point occurs almost at the same width for all values of S within the range indicated, due to the lack of dependence of the characteristics of the channel waveguide on the separation S. Also as seen from Fig. 6-4, the magnitude of the slope at the intersection point is larger on the left hand side than on the right hand side, indicating that the intersection point with large waveguide width is preferable because of the larger fabrication tolerance.

Although for S = 11.65 μm, no intersection with R = 2.385 line occurs, the maximum index change Δn_{max} can be increased so that the curve intersects the horizontal dotted line, as shown in Fig. 6-5. Again, R = 2.385 is satisfied for two waveguide sizes with the curve shifting upward with increasing Δn_{max}. For smaller separation S, Δn_{max} needs to be larger and since the intersection point on the right hand side may cause the guide to become multimoded, the left intersection point with smaller waveguide size should be chosen for high Δn_{max}.

For a given set of fabrication conditions, and under weak coupling conditions, the behavior of the individual channel waveguides

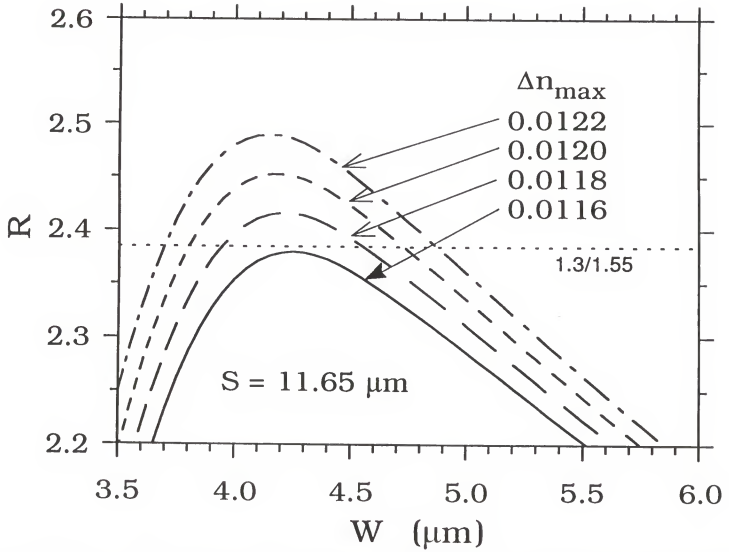

Fig. 6-5. Calculated R as a function of the waveguide half-width W for S=11.65 μm for various values of the maximum index change at surface Δn_{max} = 0.0122 (dotted-dashed), 0.0120 (short dashed), 0.0118 (long dashed), and 0.0116 (solid). The horizontal dotted line represents the ratio R equal to 2.385.

remains almost unaffected with variation in S. The value of S, however, is subject to the restrictions discussed in the previous paragraphs. Consequently, the wavelength range over which the channel guide remains single-moded is the same as the range in which two normal modes exist in the directional coupler. Moreover, the ratio R is almost a linear function of S with its slope approximately equal to 0.35 μm^{-1}, as shown in Fig. 6-6 for W = 4.9 μm. This implies that R is predictable if we first make some trial directional couplers with different gaps and measure the coupling lengths for at least two wavelengths. The nearly linear relationship between R and S is extremely useful in designing dual wavelength demultiplexers.

Figure 6-7 illustrates the coupling length versus wavelength for the separation S = 11.8 μm (long dashed line), 12.0 μm (solid line), and 12.2 μm (short dashed line). The coupling becomes weaker and the coupling length becomes longer as S increases or the wavelength decreases. The required interaction length of the demultiplexer can be determined once the two coupling lengths have been calculated. The numerical simulation provides useful guidelines not only in designing the wavelength demultiplexer but also in yielding the required fabrication conditions so that the device functions efficiently at the two wavelengths, while meeting the specifications.

6.4. Fabrication

The device was fabricated using a procedure similar to that presented in chapter 4. The difference is that an extra step is needed in the photolithography if only the mask with well-isolated channel

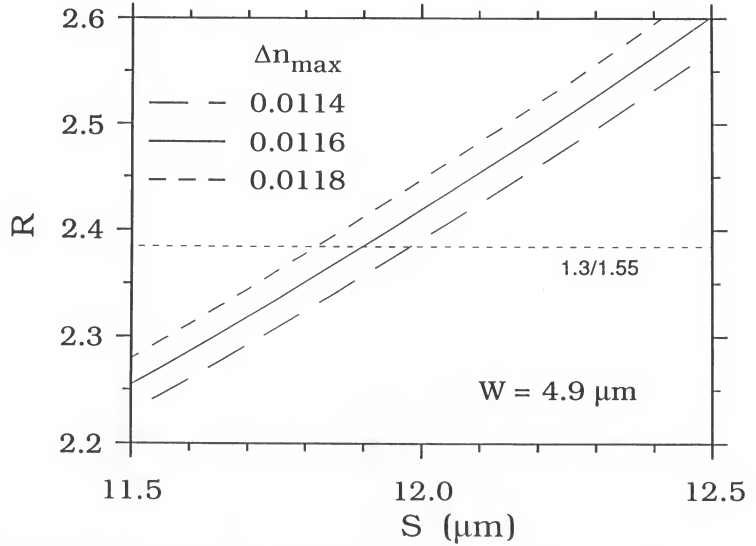

Fig. 6-6. Calculated R versus the separation S for W = 4.9 μm with the maximum index change at surface as parameter – Δn_{max} = 0.0114 (long dashed), 0.0116 (solid), and 0.0118 (short dashed). The dotted line represents the ratio R equal to 2.385.

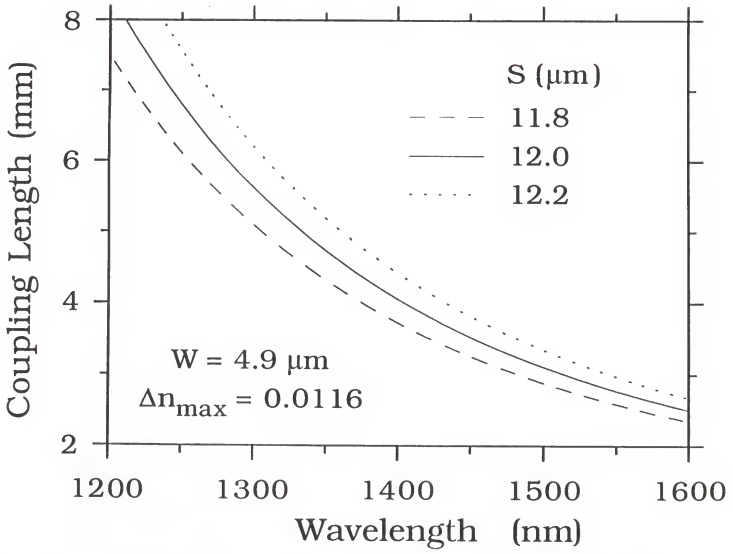

Fig. 6-7. Coupling length l_c (mm) versus wavelength λ (nm). For W = 4.9 μm and $\Delta n_{max} = 0.0116$, the dashed, solid, and dotted curves correspond to S = 11.8, 12.0, and 12.2 μm, respectively.

waveguide patterns is available. The photoresist film on the glass substrate is prepared as described previously. After the exposure to the UV light, the sample is slightly separated from the mask and shifted a distance S (=12 μm) horizontally in the direction normal to the channels. Next, the sample is contacted to the mask again and exposed to the UV light. In the second exposure, part of the sample is blocked so that the channel patterns created by the second exposure are shorter than those generated by the first exposure. Consequently, device patterns as shown in Fig. 6-2 can be fabricated.

The salt bath used is the same as described in chapter 4. The diffusion temperature and time are 350°C and 12 hours, respectively. The resulting channel waveguides support fairly well-guided, single modes at both wavelengths, viz., 1.3 and 1.55 μm for W_M varying from 2.5 to 4.0 μm. For mask openings wider than 4.0 μm, a shorter diffusion time is required to fabricate single-mode channel waveguides. As simulated in the last chapter, the fabrication conditions are critical. As a result, single-mode operation may not always be possible at both operating wavelengths. Moreover, if the diffusion time is too short, the device operates near cutoff at longer wavelengths and may suffer higher insertion loss.

Since the device performs very differently depending on the separation, S must be controlled precisely — typically, to an accuracy better than one tenth of micrometer. As shown in Fig. 6-6, for a variation of 0.1 μm in S, $\Delta R/R_o$ is approximately 1.5%, corresponding to a χ_2 of -27 dB. In the weak coupling regime, the difference in the propagation constants between the two individual channels of the directional coupler must be as close to zero as possible in order to

achieve maximum power transfer. Any imperfections in the fabrication of the channels will certainly degrade the performance of the devices.

6.5. Characterization

In almost all the applications of the directional couplers, the coupling length determines the performance of these devices. Therefore, the characterization of the coupling length is of paramount importance. In this section a novel technique [Chen90c] is presented to determine the coupling lengths of directional couplers as a function of wavelength. The coupling lengths are evaluated from the measured normalized power outputs based on coupled-mode theory by assuming that the symmetric couplers consists of two weakly coupled waveguides. The experimental setup to measure the outputs and the procedure to estimate the coupling length are presented in the following subsections.

6.5.1. Measurement of Spectral Response

As discussed earlier, the outputs P_1 and P_2 are wavelength-dependent. They can be measured by the experimental setup shown in Fig. 6-8. A high-power tungsten lamp is used in the setup as a source for the monochromator. The light from the lamp is focused at the entrance of the monochromator with a slit of ~1 mm opening. The positions of lenses 1 and 2 are adjusted until the output from the monochromator is maximum at the operating wavelength. Hence, a temporary detector is needed at output of the monochromator in building the setup. The output slit of the monochromator is set to be

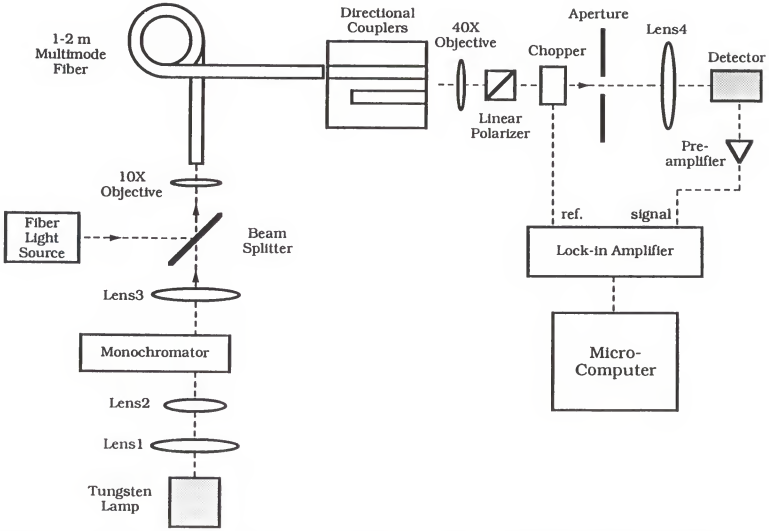

Fig. 6-8. The experimental setup used to measure the spectral response of the directional couplers. The white light source is used for alignment and is removed during the measurement of the spectral response of the devices.

about 100 μm determining the linewidth of the monochromatic light. Lens 3 is used to collimate the output light from the monochromator, and the 10X objective is used to collect the light and launch it into a multimode fiber. Since the waveguide is a single-mode guide, only the fundamental mode can be excited. The light which is not coupled into the fundamental mode radiates away and does not affect the propagation of the wave in the coupler. A fiber light source and the beam spitter between the lens 3 and the objective are used solely for the purpose of aligning the directional coupler and are removed once it is aligned. The light from the monochromator or the fiber light source are butt-coupled to the device through a multimode fiber. The output from the coupler is magnified and focused by a 40X objective and imaged onto a Ge detector by lens 4. A linear polarizer and a chopper are inserted between the objective and an aperture so that a polarized, chopped signal can be obtained. The signal is amplified by a preamplifier and a lock-in amplifier and, then, fed into a computer.

In the alignment, the use of a white light source instead of a visible laser is required since at the visible laser wavelength very little power transfer occurs and only the straight through output is seen. On the other hand, the white light passing through the directional coupler with two channels generates an image with two spots. The near-field output is focused by a 40X objective at the aperture which is used to choose one of the output spots. It is easier to isolate one spot from the other by the aperture only if they are far away from each other, *i.e.*, weakly coupled. In the case of a strongly coupled waveguide system, a bend structure is usually needed to separate the outputs for accurate measurement. The measurement is performed twice for one

coupler, *i.e.*, one for each channel, by varying the wavelength. The normalized power outputs is obtained by dividing the individual channel output by the total power output from both channels.

Since the monochromator output is weak, a chopper and a lock-in amplifier are necessary to measure the signal. In the measurement, the time constant of the lock-in amplifier is set to one second which is considered much longer than the noise period. Since the resolution of the monochromator is about 5 nm in IR, the wavelength scanning of the monochromator should not exceed 5 nm/sec otherwise the signal may be smoothed out and an accurate measurement is not achievable. We arbitrarily choose the scanning speed of 100 nm/min. In this case it takes 4 minutes to scan from 1200 nm to 1600 nm.

Figure 6-9(a) shows a typical normalized outputs (P_2) versus wavelength for the TE mode. The solid and the dashed lines represent the interaction lengths L_1=16.2 mm and L_2=13.1 mm, respectively. The notation 'p' will be discussed in the next subsection. The figure exhibits sinusoid-like curves indicating that complete power transfer can be achieved at certain wavelengths depending on the interaction length. The evaluation of the coupling length from the measured P_2 is presented in following section.

6.5.2. Determination of the Coupling Length

The coupling length l_c can be estimated by measuring the normalized power output P_2 as a function of wavelength at port 2. This is easily seen by rewriting Eq. (6.25) as

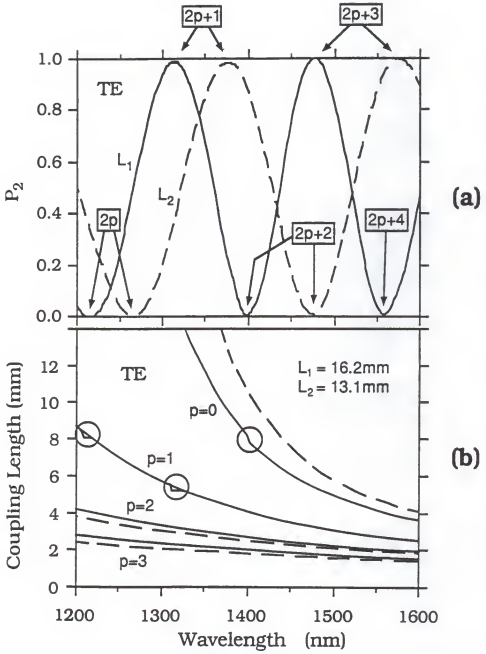

Fig. 6-9. Normalized output P_2 and coupling length vs. wavelength. (a) P_2. (b) Coupling length.

$$l_c(\lambda) = \frac{\pi L/2}{m\pi \pm \sin^{-1}\sqrt{P_2(\lambda)}}, \qquad (6.38)$$

where m is an integer and equals 0, 1, 2,..., *etc.* The selection of the plus or minus sign and m, which are determined by the phase difference of the even and odd modes as well as the number of the cycles of power transfer between the guides, are discussed later. Conventionally, at least two measurements of P_2 for two close interaction lengths for a given λ are required to evaluate l_c. As the period of oscillation increases either with shorter coupling length or with increasing asymmetry as the case may be, the conventional approach will not lead to meaningful results. On the other hand, Eq. (6.38) and the spectral response measurement for different interaction lengths of the same directional coupler may give accurate values of l_c as a function of wavelength. The spectral response technique described here is quite useful in extracting the coupling length.

Figure 6-9(a) shows the normalized power output P_2 as a function of the wavelength. P_2 is maximum whenever the interaction length L (=L_1 or L_2) equals an odd number of coupling lengths. For the purpose of discussion, these peaks are identified as 2p+1, 2p+3, *etc.* at the top of Fig. 6-9(a) for different wavelengths, where p is a non-negative integer. P_2 is zero for the interaction lengths corresponding to an even number of coupling lengths marked as 2p, 2p+2, *etc.* at the bottom of the same figure. The peaks (maxima) with the same number of coupling lengths shift to longer wavelengths for devices with shorter interaction lengths. Furthermore, the periods, *i.e.*, the

wavelength separation between two adjacent peaks increase as the interaction lengths decrease, which implies that the sensitivity to wavelength decreases for shorter directional couplers. This can be easily seen in the case of the wavelength demultiplexer with the shortest interaction length (L=5.4 mm) operating at 1.32 and 1.56 μm [Chen90b]. For such a short device incorporating one coupling length at 1.32 μm and two coupling length at 1.56 μm, it is obvious the output should be somewhat insensitive. The tolerance in terms of wavelength is discussed in detail in section 6.4.

For the same interaction length, the valley (minimum) in Fig. 6-9(a) adjacent to a given peak at the longer wavelength always corresponds to one more coupling length than that at the maximum since the coupling length is shorter at longer wavelength. However, the number of coupling lengths at a given maximum or minimum can not be uniquely determined with only one measurement at a given interaction length; at least two measurement with different interaction lengths are required. We will illustrate the problem for the case shown in Fig. 6-9(a). Equation (6.38) has been used to calculate the coupling length from the measured P_2 for a given interaction length, say $L=L_1$. Since many wavelengths can give rise to the same P_2, it is necessary to keep track of m as well as the sign in the denominator of the right-hand side of Eq. (6.38). Furthermore, we note that the coupling length l_c must be a positive quantity, monotonically decreasing with increasing wavelength. Therefore, l_c is largest for m=0 and the plus sign is chosen. In this case, l_c decreases as P_2 increases from nearly zero at lower wavelength to one. As the wavelength further increases, P_2 will decrease from the peak value

down to the valley, where P_2=0. Since we require that l_c must be continuous and decrease monotonically, m now shall be set to one and the minus sign must be chosen for l_c in the interval between L and L/2. l_c=L when P_2 equals one and decreases to l_c=L/2 when P_2 becomes zero. As indicated in Fig. 6-9(a), the minus sign is always taken for P_2 going from maximum to minimum as the wavelength increases and the plus sign is taken for P_2 going from the valley to the next peak at the longer wavelength. m is always increased by one unit when P_2 reaches the maximum as the wavelength increases. Consequently, m equals 2p+1 in the region between the peaks corresponding to $l_c(\lambda)$=L/(2p+1) and $l_c(\lambda)$=L/(2p+3). Thus, the value of m remains the same between two consecutive peaks and increases by unity at each peak. The sign in Eq. (6.38), on the other hand, is negative as P_2 decreases and is positive as P_2 increases. In this manner, with careful bookkeeping, l_c can be calculated from the measured P_2 by using Eq. (6.38).

Figure 6-9(b) shows the computed coupling lengths from the measured values of P_2 as a function of the wavelength assuming various values for p, viz., p=0, 1, 2, and 3. The solid lines represent the case when the interaction length L=L_1. By repeating the procedure, l_c versus λ is evaluated for the case L=L_2 and is represented by the dashed lines for p=0, 1, 2, and 3. The solid curve coincides with the dashed curve for p=1 indicating the correct value of p since the coupling length must be independent of the interaction length L. The discontinuities occurring at the peaks or the valleys of P_2, highlighted as circles, are introduced by the limited signal-to-noise ratio available in the experiment since an incoherent light source was used. For

asymmetric directional couplers, Eq. (6.25) is not applicable [Chen90c] since the power can not completely transfer to waveguide 2. In this case, the normalized powers in the individual waveguides can be derived from Eq. (6.4) as

$$P_1 = \frac{a_1 a_1^*}{A_0^2} = \cos^2(Kz) + \frac{\delta^2}{K^2}\sin^2(Kz)$$
$$P_2 = \frac{a_2 a_2^*}{A_0^2} = \frac{|\kappa_{12}|^2}{K^2}\sin^2(Kz) \quad , \tag{6.39}$$

where $K = \sqrt{\delta^2 + \kappa_{12}\kappa_{21}}$ and $\delta = (\beta_2 - \beta_1)/2$. δ is zero for the symmetric case and the above equation reduces to Eq. (6.7). When the coupling between the two waveguides becomes stronger, the scalar coupled-mode theory breaks down and Eq. (6.39) is not applicable.

6.6. Experimental Results and Comparison with Modeling

Utilizing the technique described above, we measure the normalized power outputs P_1 and P_2, which are used to evaluate the coupling length l_c as a function of wavelength. Figures 6-10 (a) and (b) show the coupling length versus wavelength for the mask opening W_M = 3.0 μm and 3.5 μm, respectively. The discrete points denote the simulation results and the solid lines represent the coupling lengths calculated from the experimental measurement. As expected, the coupling length for the TE mode is slightly larger than that for the TM mode due to better confinement of the modal field. The reason being, although the waveguide is almost homogeneous and isotropic, the TM mode, experiences a slightly lower propagation constant, has a weaker confinement and hence, a smaller coupling length. Because the

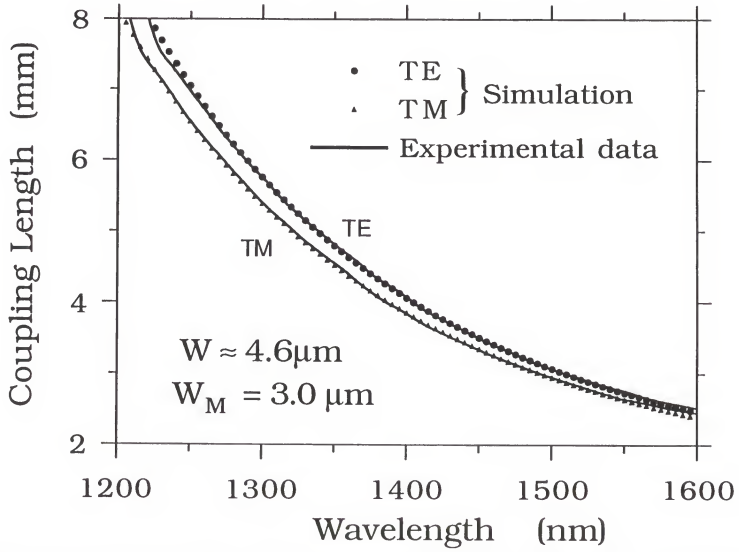

(a)

Fig. 6-10. Estimated and measured coupling length (mm) for TE and TM modes vs. wavelength (nm). The simulation results are represented by discrete points, where (a) $W \approx 4.6$ μm for $W_M = 3.0$ μm. The experimental measurements are represented by the solid lines.

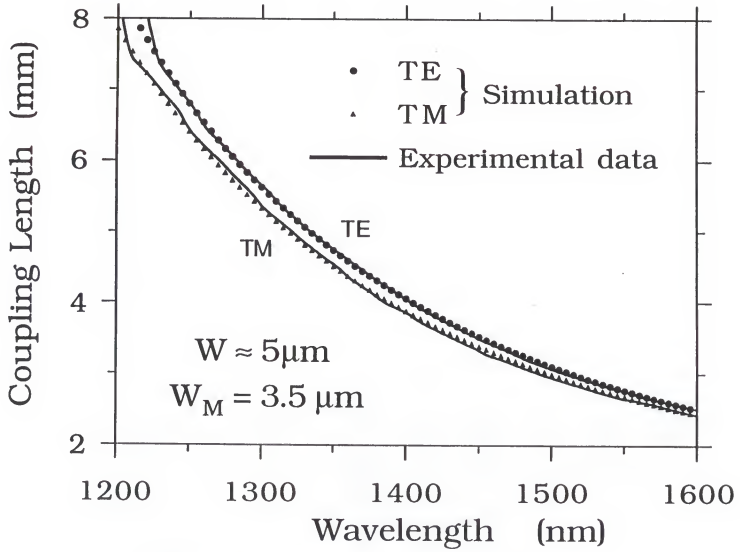

(b)

Fig. 6-10 – continued. (b) $W \approx 5.0$ μm for $W_M = 3.5$ μm.

channel waveguide becomes multimoded around 1.2 μm wavelength, the modeling is inapplicable at wavelengths below 1.2 μm since the directional coupler now has more than two normal modes.

The devices were designed to operate at 1.315/1.561 μm wavelength. For the TE mode, the simulation shows an R equal to 2.352 for the demultiplexer operating at these two wavelengths. The experimental data show that R is equal to 2.378 for the same wavelengths, in the case of W_M=3.5 μm. The coupling lengths for the TE mode are 5.37 mm and 2.68 mm at 1.315 μm and 1.561 μm wavelengths, respectively. However, the device is not optimized for TM mode and the ratio R equals 2.338 for the two wavelengths in our experiment. In the simulation, for the mask openings W_M= 3.0 and 3.5 μm, the waveguide half-width W are 4.58 and 4.97 μm, respectively, and the maximum index change Δn_{max} for TM mode is about $1\text{-}2X10^{-4}$ lower than for TE mode. This is believed to be caused by a small birefringence in the Ag^+-Na^+ exchanged channel waveguide.

Figures 6-11 (a) and (b) show the normalized power output at port 2 as a function of wavelength with L= 5.37 mm for W_M= 3.0 μm and 3.5 μm, respectively. The simulation results are respectively represented by the closed and open circles for the TE and TM modes, and the experimental data are denoted by the solid and dashed lines for the TE and TM modes, respectively. From the experiment, it is seen that both the cross power ratio ζ at 1.561 μm and the crosstalk χ_1 at port 1 are -32 dB. Both the cross power ratio ζ at 1.315 μm and the crosstalk χ_2 at port 2 are -30 dB, which are not as good as those at port 1 because the interaction length L is slightly different from the coupling length l_c(1.3 μm). The curve for the TM mode shifts about

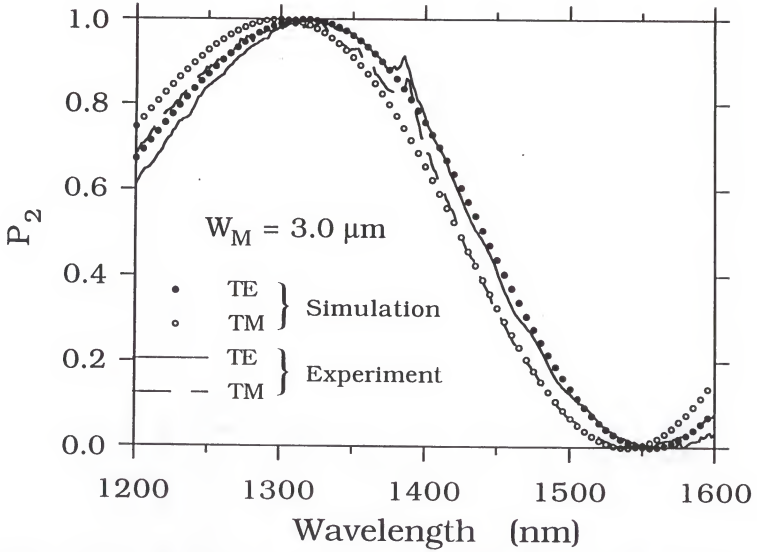

(a)

Fig. 6-11. The normalized power output P_2 at port 2 vs. wavelength (nm) for (a) W_M= 3.0 μm. The simulation results are represented by closed circles (TE mode) and open circles (TM mode) and the experimental measurements by the solid (TE mode) and the dashed (TM mode) lines. The interaction length is 5.37 mm.

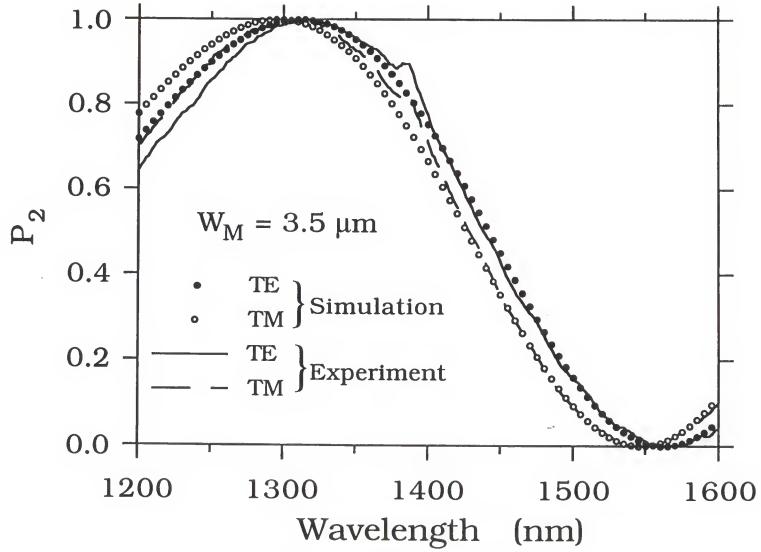

(b)

Fig. 6-11 – continued. (b) W_M= 3.5 μm.

16 nm toward shorter wavelengths compared to that of the TE mode since the TM mode exhibits a shorter coupling length. A small hump at 1.39 μm wavelength is caused by the existence of a water absorption peak in the fiber used in the measurement system. Furthermore, the behavior of the coupling length in Figs. 6-10(a) and (b) and the power output in Figs. 6-11(a) and (b) as functions of wavelength are similar for both cases, *viz.*, W_M= 3.0 μm and 3.5 μm. This indicates that the coupling between the guides of the directional coupler as well as the sizes of modal fields in the channel waveguides are somewhat insensitive to the mask openings in this range. The modeling results are in excellent agreement with the experimental results for both the coupling length and the normalized power output, as illustrated in Figs. 6-10 and 6-11. The devices described above were fabricated and tested to verify the accuracy of the model. We have also achieved a demultiplexer device, where the shortest intersection length (L= 5.37 mm) demultiplxer was optimized to operate at 1.315/1.561 μm, with insertion loss of 1.25 dB for a total device length 14.5 mm and propagation loss of 0.15 dB/cm for the mask opening of 3.5 μm with a cross power ratio and crosstalk of less than -40 dB. Figure 6-12 shows the near-field intensity profile in the horizontal direction (y-axis) at the output with W_M = 3.0 μm, measured by the near-field setup shown in Fig. 4-9. A 1.315 μm wavelength laser diode was used to excite the demultiplexer at the input end. The mask opening regions are indicated by two rectangulars with mark 1 as waveguide 1 and mark 2 as waveguide 2. It is obviously that the energy is confined in the waveguide 2. The cross power ratio ζ at port1 was measured to be less than -40 dB at this wavelength.

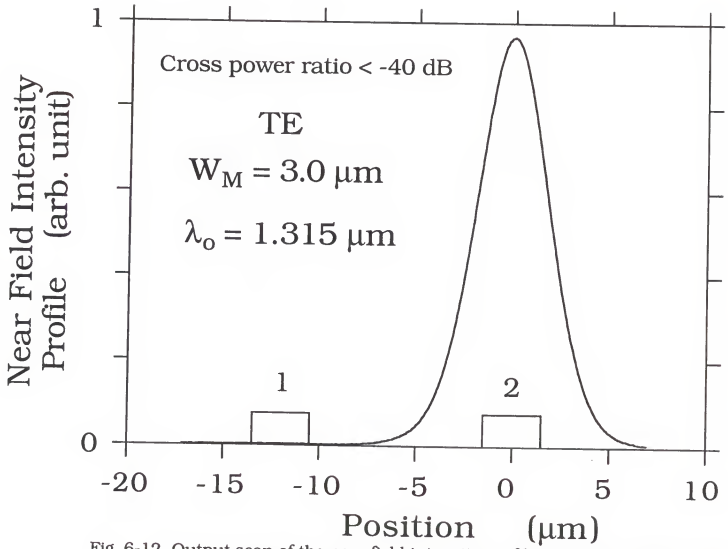

Fig. 6-12. Output scan of the near field intensity profile across the output ports 1 and 2 in the plane of the substrate at 1.315 μm wavelength.

To check the validity of the modeling, devices with L equal to three times of l_c(1.315 μm) and six times of l_c(1.561 μm) were also fabricated. As shown in Fig. 6-13, again the simulation agrees very well with the experimental results for (a) W_M= 3.0 μm and (b) W_M= 3.5 μm. The peaks or maxima correspond to an odd number of coupling lengths with complete power transfer to port 2. The valleys or minima, on the other hand, correspond to an even number of coupling lengths and a complete transfer of power at port 1. As indicated earlier, the fabrication conditions are more critical for these longer devices since the spectral bandwidth $2\Delta\lambda$ corresponding to -20 dB point is smaller than that of the devices shown in the Figs. 6-11(a) and (b). The sensitivity to the polarization also increases, which is undesirable in coherent optical communication applications. In addition, the total insertion loss increases due to the increase in the length of the devices.

6.7. Summary

In this chapter, we have discussed the scalar coupled-mode theory. Although the application of the theory is limited to the case of weak coupling, it is still useful in predicting the power transfer in the directional couplers since the devices are weakly coupled. The numerical analysis was dealt with using the normal-mode approach so that the coupling coefficient can be estimated from the normal mode indices.

A thorough model was presented for the 1.32/1.56 dual wavelength demultiplexer. The modeling was used to predict the

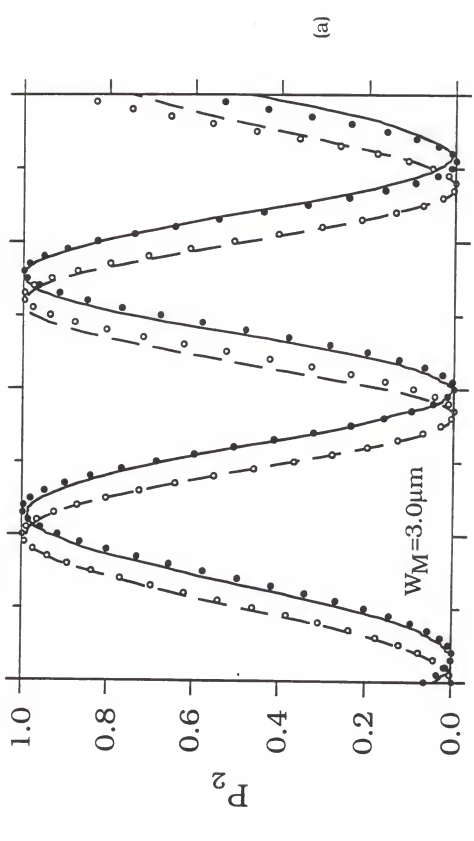

Fig. 6-13. The normalized power output P_2 at port 2 vs. wavelength (nm) for (a) W_M= 3.0 μm. The simulation results are represented by closed circles (TE mode) and open circles (TM mode) and the experimental measurements by the solid (TE mode) and the dashed (TM mode) lines. The interaction length is 16.1 mm.

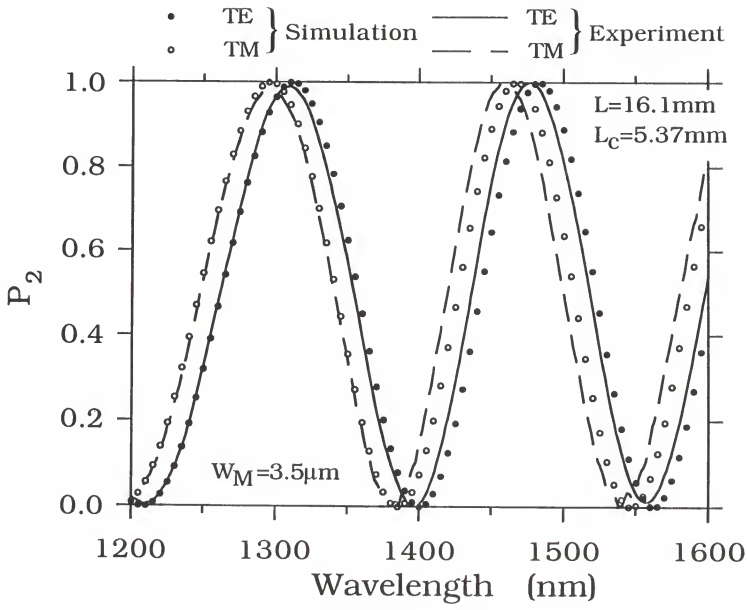

(b)

Fig. 6-13 – continued. (b) W_M= 3.5 μm.

coupling lengths of the devices and the normalized power outputs. The fabrication parameters were optimized by the simulation so that the demultiplxers were successfully fabricated. The crosstalk and cross power ratio were defined in terms of the fabrication deviation ΔL, ΔR or Δl_c. The crosstalk and cross power ratio of the demultiplexers were measured to be less than -30 dB at the operating wavelengths of 1.315 and 1.561 μm. The experimental setup to measure the spectral response and a novel procedure to evaluate the coupling lengths of the directional couplers were also addressed in this chapter.

CHAPTER 7
CONCLUSIONS AND FUTURE WORK

7.1. Conclusions

The objective of this project was to perform a general, systematic, theoretical and experimental study of the ion-exchange process in glass. This research work includes the modeling characterization of 1-D and 2-D diffusion and the resulting graded-index waveguides as well as the application of these waveguides to two practical devices: tapered waveguide transitions and wavelength MUX/DEMUX using symmetrical directional couplers. Excellent agreement of the modeling with the experimental results has been obtained.

The following is a list of accomplishments resulting from this research work:

1. Fabrication of Ag^+-Na^+ exchanged waveguides with mask material consisting of an Al_2O_3 thin film sandwiched between the top aluminum layer and the substrate. Single-mode, low-loss waveguide devices in BK7 glass with propagation loss as low as 0.15 dB/cm were obtained.
2. Numerical solutions of single-step and two-step diffusion with and without an externally applied field by the Green's function method. Conditions to achieve symmetrical, buried waveguides were obtained in the simulation.

3. Determination of the silver self-diffusion coefficient in BK7 glass as a function of temperature by the inverse WKB method from the prism-coupler measurement and comparison to the simulation using the finite difference method.
4. Systematic modeling of planar, channel, and postbaking tapered waveguides. The modeling results are in excellent agreement with experimental measurements of the index and near-field profiles.
5. Modeling of radiation loss of tapered waveguides by the beam propagation method for various taper functions. Lossless tapers are achievable for taper lengths of more than 2 mm.
6. Thorough simulation of symmetrical directional couplers as dual wavelength MUX/DEMUX. The spectral bandwidth, crosstalk, and cross power ratio were derived in terms of the fabrication parameters.
7. Demonstration of a novel technique to determine the coupling lengths of weakly-coupled symmetrical directional couplers as a function of wavelength by the spectral response.
8. Experimental fabrication of 1.32/1.56 μm wavelength MUX/DEMUX with crosstalk and cross power ratio less than -40 dB.

The results obtained in this work demonstrate that ion-exchanged waveguides and devices can be fabricated and modeled to determine the processing parameters a priori for specific device performance. Although most of the work was performed using the silver-sodium cation pair and BK7 glass, the theory and numerical method presented here are adequate to treat other cation pairs and

substrate glasses. In the following sections, we outline the future prospects of the ion-exchange technique and point out some of the research issues which remain to be addressed for future exploitation of the process in designing novel devices.

The scope for future work based on the above conclusions is described in the following. The research to be pursued in the future essentially would have two directions: 1) advanced study of the ion-exchange process, 2) research on the functional devices and integration of waveguide devices. These two topics will be briefly discussed in the following sections. The goal of the research on the ion exchange and the devices is to apply the results to a practical optical communication system.

7.2. Advanced Study on Ion Exchange

Since the ion exchange process is an essential part of modeling of all the ion-exchanged devices, the knowledge gained from the advance study can help set up a more versatile modeling which is applicable to most of cases. The prospective study includes the modeling for other cation pairs, space-charge effect, local field, side diffusion, electromigration, and thorough analysis of 2-D buried waveguides *etc.* They will be discussed in the following subsections.

7.2.1. Other Cation Pairs

Ag^+-Na^+ exchange and the devices using this cation pair have been concentrated in this research work. Other ion pairs, *e.g.*, K^+-Na^+, Tl^+-K^+ *etc.* for different glasses, are considered to be very useful.

Several reports have been published dealing with the case of K^+-Na^+ exchanged waveguides [see reference list in section 2.3]. It is well known that the K^+-Na^+ exchange creates birefringence of the waveguides due to stress-induced index change [Yip85]. This feature can be employed to fabricate polarization-dependent devices such as TE/TM splitters. Besides, the index change is quite small and, therefore, it is useful for fabricating single-mode devices. As a matter of fact, high-performance waveguides fabricated by K^+-Na^+ have been realized in this laboratory [Mili89]. However, a detailed modeling of the 2-D ion exchange in this case still remain to be performed.

Low-loss waveguides fabricated by thallium ion exchange have been demonstrated since 1972 [Izaw72]. Tl^+ has very high polarizability compared to Na^+ or K^+ and, therefore, it produces quite high index change (~0.1) when exchanged with Na^+ or K^+ ions. Furthermore, the loss of the thallium exchanged guides is very small. However, Tl^+ is highly toxic and a good ventilation system is required during the fabrication. Limited results have been reported on this cation system in the past and extensive study still needs to be carried out.

The self-diffusion coefficients for different exchanging ions are different at the same temperature. Novel devices, fabricated by various ion pairs with the small-diffusion-coefficient ions exchanging first at high temperature followed by the second ion exchange at lower temperature, may take advantage of each ion-pair and fulfill the requirements for the realization of new devices. In this case, a systematic study and modeling are necessary for the multi-ion exchanged, guided-wave devices.

7.2.2. Space Charge, Local Field, and Side Diffusion

In chapter 2, the nonlinear diffusion equation was derived from the Fick's law with the assumption of almost negligible space charge density. However, for the case of $\alpha N_A \sim 1$, the space charge may not be omitted. The effect causes steeper index profiles [Neum79]. Therefore, the electric field induced by the space charge must be considered in the modeling so that a more accurate index profile can be predicted.

It is believed [Char80, Walk83b] that if a metallic mask is used, a local field from the mask opening region to the region under the mask can be generated by the electrochemical potential differences between the interface of mask-glass and that of melt-glass. Usually the local field induced by the mask material may speed up the horizontal diffusion and, hence, the side diffusion is larger than the vertical diffusion, resulting in the waveguide width being much larger than the waveguide depth. In this case, the fabrication conditions for single-mode waveguide are more critical, as mentioned in chapter 5. To solve the problem, dielectric mask materials and guard-band openings may be used to help reduce the local field induced by the mask.

Eletromigration has been intensively investigated and reported [Abou79, Coop80, Lili82, Yosh85, Kane85, Kane86, Forr86]. Under an external applied field, the space charge density becomes even larger than the case without the field. Recently, Albert and Lit [Albe90] have demonstrated the modeling of field-assisted ion exchange. However, they assume that the total ion concentrations equal the initial concentration of the host ions, *i.e.*, $C_A + C_B = C_{B0}$, which is not true

when the space charge is not negligible, especially, under an external field. Further study on the space charge effect is needed.

7.2.3. 2-D Buried Waveguides

The buried waveguides are known to be immune to surface roughness and their scattering loss is lower than surface waveguides. In addition, a symmetric, fiber-compatible mode-field profile is achievable. Mode mismatch loss is reduced when the waveguide is embedded into the substrate.

The simulation of 1-D buried waveguides was presented in chapter 3. The buried waveguides are usually obtained by a two-step process.[1] The modeling for the 2-D buried waveguides needs to be performed since it is of paramount importance in designing fiber-compatible modal fields.

7.3. Functional Devices and Integrated System

In this section, some useful passive devices are proposed to achieve special functions in optical communication systems, *e.g.*, coupling to fibers, wide-band MUX/DEMUX, narrow-band filters, *etc.* Furthermore, an integration of these devices is also an important issue to be addressed.

7.3.1. Waveguide Bends

The directional couplers discussed in chapter 6 are constructed by two straight channels without waveguide bends. As a result,

[1] One-step buried waveguides can also be obtained by metallic silver film diffusion with applied field using molten salt bath as the electrodes [Pant87, Gunt88, Zhen88].

difficulties occur in separately coupling into fibers since the diameter of the fiber is about 125 μm, which implies that the separation of the two guides at the output should be at least 125 μm. As shown in Fig. 7-1, waveguide bends can be added at both the input and output ends for coupling purpose. They are necessary for practical applications. However, an analysis of bent waveguides as well as the variation in the power outputs of the coupler with bends was not carried out in this work. The modeling of the bends in practical directional couplers can be simulated by BPM. The loss caused by the bending can also be evaluated by this method. To minimize the radiation loss and to increase the packing density of devices, gradual index tapers along bends with the maximum index change occurring in the shapest region would be helpful in designing smaller radii bends. Mechnisms to incorporate such tapered bends need to be investigated.

7.3.2. Asymmetric Y-Branch

As discussed in chapter 6, a MUX/DEMUX using symmetric directional couplers is sensitive to the variation of the interaction length, as shown in Eq. (6.26), (6.27),(6.36), and (6.37). If ΔL is not zero, then the crosstalk as well as the cross power ratio will deteriorate significantly. An asymmetric Y-branch, considered to be immune to the length variation, is proposed by Negami *et al.* [Nega89] and realized by Goto and Yip [Goto90] using ion exchange technique. The schematic diagram is shown in Figs. 7-2(a) and (b). The two branches have different index profiles. The angle θ of the Y-branch must be small enough (of the order of milli-radians) to satisfy the

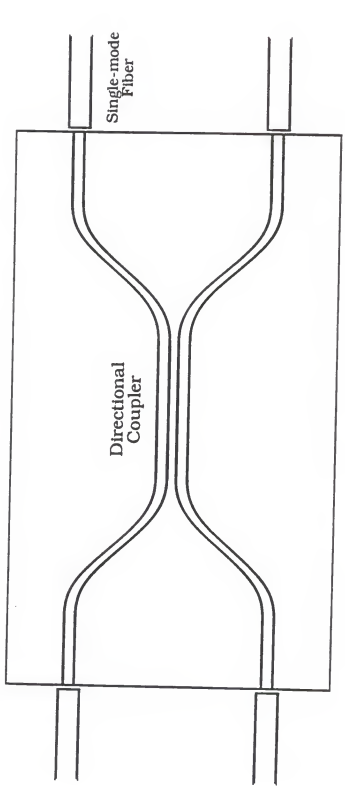

Fig. 7-1. Directional coupler with bends for coupling with fibers.

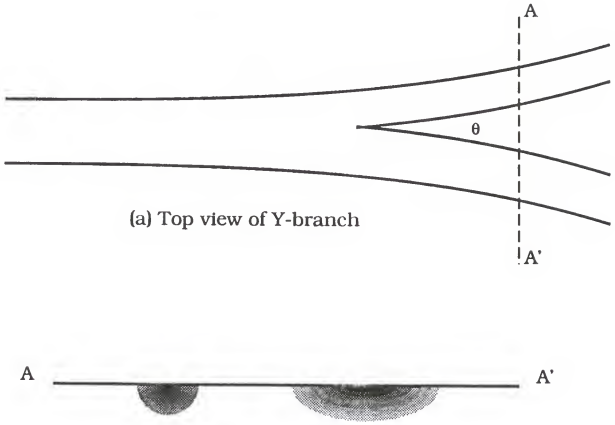

Fig. 7-2. Asymmetrical Y-branch for wide band MUX/DEMUX.

adiabatic condition so that no mode conversion occurs in the device. In the wavelength region longer than the specified wavelength at which the phase matching condition is met, one branch is assumed to have a larger propagation constant than the other so that the fundamental mode of the input guide will travel along this branch. On the other hand, in the shorter wavelength region, if the other branch has a larger propagation constant, then the mode will travel along this branch. Hence, the function of MUX/DEMUX is attainable. In principle, this configuration has a wider bandwidth than the symmetric directional coupler. Although the crosstalk is predicted theoretically to be -20 dB, the reported crosstalk is measured to be between -5 dB and -6 dB, illustrating that some improvements still can be made to obtain better performance. For example, one can utilize both the material as well as waveguide dispersion.

7.3.3. Asymmetric Directional Coupler

As the density of channels in optical communication becomes higher, narrower bandwidth filters for multiplexing and/or demultiplexing the signals in frequency domain are likely to become essential components in the system. The asymmetric directional coupler is designed such that phase matching is satisfied at only one wavelength where the dispersion curves of these two guides intersect. At this wavelength, if the interaction length of the coupler exactly equals an odd number of coupling lengths, then the power can completely transfer to the second waveguide. At the other wavelengths, complete power transfer is not possible since the phase

matching condition is not met. Such a device has been demonstrated in $LiNbO_3$ by Alferness [Alfe78]; the bandwidth of this device is very narrow so that it is suitable for using as MUX/DEMUX in high-density communication system. The realization of this device in ion-exchanged waveguides would be similar to the asymmetric Y-branch. The difference is that the two guides are parallel to each other in this case.

7.3.4. Glass Waveguide Laser and Integrated System

Neodymium doped glass lasers were developed more than two decades ago. However, laser action in ion-exchanged waveguides has been demonstrated in Nd:glass only recently [Sanf90, Aoki90]. Their miniature structure and their potential to integrate with other ion-exchanged, passive devices makes them attractive. Sanford *et al* demonstrated the fabrication by K^+-Na^+ exchange, while Aoki *et al* used metallic silver film. In both cases, external fields are employed. Lasing wavelengths are 1.054 and 1.057 nm, respectively. However, the integration of active and passive devices is yet to be reported.

The integrated system consisting of light sources and passive devices can be applied to not only optical communication but also optical sensing. By using ion exchange in glass, the fabrication of the integrated system is easy and the cost of processing is reduced. Further research work needs to be performed to achieve such an integrated system.

REFERENCES

[Abou79] M. Abou-el-Leil and A. R. Cooper, "Analysis of Field-Assisted Binary Ion Exchange," J. Am. Ceram. Soc., vol.62, pp.390-395, 1979.

[Abou88] M. Abou-el-Leil and F. Leonberger, "Model for Ion Exchanged Waveguides in Glass," J. Am. Ceram. Soc., vol.71, pp.497-502, 1988.

[Albe90] J. Albert and J. W. Y. Lit, "Full Modeling of Field-Assisted Ion Exchange for Graded Index Buried Channel Optical Waveguides," Appl. Opt., vol.29, pp.2798-2804, 1990.

[Alfe78] R. C. Alferness and R. V. Schmidt, "Tunable Optical Waveguide Directional Coupler Filter," Appl. Phys. Lett., vol.33, pp.161-163, 1978.

[Aoki90] H. Aoki, O. Maruyama, and Y. Asahara, "Glass Waveguide Laser," IEEE Photo. Tech. Lett., vol.2, pp.459-460, 1990.

[Baet82] R. Baets and P. E. Lagasse, "Calculation of Radiation Loss in Integrated-Optic Tapers and Y-Junctions," Appl. Opt., vol.21, pp.1972-1978, 1982.

[Beie85] W. Beier and G. H. Frischat, "Transport Mechanisms in Alkali Silicate Glasses," J. Non-Cryst. Solids, vol.73, pp.113-133, 1985.

[Bran86] A. Brandenburg, "Stress in Ion-Exchanged Glass Waveguides," J. Lightwave Tech., vol.LT-4, pp.1580-1593, 1986.

[Brob86] B. Broberg, B. S. Lindgren, M. G. Öberg, and H. Jiang, "A Novel Integrated Optics Wavelength Filter in InGaAsP-InP," J. Lightwave Technol., vol.LT-4, pp.196-203, 1986.

[Burn88a] W. Burns, "Normal Mode Analysis of Waveguide Devices. Part I: Theory," J. Lightwave Tech., vol.LT-6, pp.1051-1057, 1988.

[Burn88b] W. Burns, "Normal Mode Analysis of Waveguide Devices. Part II: Device Output and Crosstalk," J. Lightwave Tech., vol.LT-6, pp.1058-1068, 1988.

[Burn89] W. K. Burns, "Correction to 'Normal Mode Analysis of Waveguide Devices. Part I: Theory' and 'Normal Mode Analysis of Waveguide Devices. Part II: Device Output and Crosstalk'," J. Lightwave Tech., vol.7, p.1425, 1989.

[Char78] G. H. Chartier, P. Jaussaud, A. D. de Oliveira, and O. Parriaux, "Optical Waveguides Fabricated by Electric-Field Controlled Ion Exchange in Glass," Electron. Lett., vol.14, pp.132-134, 1978.

[Char80] G. Chartier, P. Collier, A. Guez, P. Jaussaud, and Y. Won, "Graded-Index Surface or Buried Waveguides by Ion Exchange in Glass," Appl. Opt., vol.19, pp.1092-1095, 1980.

[Char82a] G. H. Chartier, J. L. Coutaz, A. Girod, P. Jaussaud, and O. Parriaux, "Optical Waveguides Made by Ion Exchange in Glass. Application to Two Dimensions Integrated Optical Devices," J. Non-Cryst. Solids, vol.47, pp.259-262, 1982.

[Char82b] G. H. Chartier, V. Neuman, O. Parriaux, and C. W. Pitt, "Low Temperature Ion Substitution in Soda-Lime Glass by Means of an Electric Field," Thin Solid Films, vol.87, pp.285-292, 1982.

[Chen87] H. C. Cheng, R. V. Ramaswamy, and R. Srivastava, "Buried Na^+-Ag^+ Ion-Exchanged Glass Waveguides: Theory and Experiment," GRIN Conf., Reno, NV, 1987, paper TuC2-1.

[Chen88] H. C. Cheng, H. Zhenguang, A. Miliou, R. Srivastava, and R. V. Ramaswamy, "Buried Low-Loss Fiber Compatible Single-Mode Ion-Exchanged Channel Waveguides," IGWO Conf., Santa Fe, NM, 1988, paper MC1.

[Chen89a] H. C. Cheng and R. V. Ramaswamy, "Simulation of the Radiation Loss of Postbaked Ion-Exchanged Thermal Tapers by BPM," MOC/GRIN Conf., Tokyo, Japan, 1989, paper B2.

[Chen89b] H. C. Cheng and R. V. Ramaswamy, "Simulation of Tapered Transitions in Ion-Exchanged Channel Waveguides," OSA Annual Meeting, Orlando, FL, 1989, paper FS4.

[Chen90a] H. C. Cheng and R. V. Ramaswamy, "Simulation of Tapered Transitions in Ion-Exchanged Channel Waveguides," Appl. Opt., vol.29, pp.1150-1156, 1990.

[Chen90b] H. C. Cheng and R. V. Ramaswamy, "A Dual Wavelength (1.32/1.56 μm) Directional Coupler Demultiplexer by Ion Exchange in Glass," IEEE Photonics Technology Letters, vol.2, pp.637-639, 1990.

[Chen90c] H. C. Cheng and R. V. Ramaswamy, "Determination of the Coupling Length in Symmetric Directional Couplers from Spectral Response," IEEE Photonics Technology Letters, vol.2, 1990.

[Chen90d] H. C. Cheng, R. V. Ramaswamy, and R. Srivastava, "Modeling of Directional-Coupler Wavelength-Demultiplexers in GRIN Waveguides Using Normal Modes," IPR Conf., Hilton Head, SC, 1990, paper MD3.

[Chen90e] H. C. Cheng, R. V. Ramaswamy, and R. Srivastava, "1.3-1.55 μm Directional-Coupler Wavelength-Multiplexers/Demultiplexers Using Ion-Exchange in Glass," CLEO Conf., Anaheim, CA, 1990, paper CThI53.

[Chia85] K. S. Chiang, "Construction of Refractive-Index Profiles of Planar Dielectric Waveguides from the Distribution of Effective Indexes," J. Lightwave Tech., vol.LT-3, pp.385-391, 1985.

[Chia86] K. S. Chiang, "Analysis of Optical Fibers by the Effective-Index Method," Appl. Opt., vol.25, pp.348-354, 1986.

[Chlu87] P. Chludzinski, R. V. Ramaswamy, and T. J. Anderson, "Ion Exchange between Soda-Lime-Silicate Glass and Sodium Nitrate-Silver Nitrate Molten Salts," Physics Chem. Glasses, vol.28, pp.169-173, 1987.

[Chua87a] S.-L. Chuang, "A Coupled Mode Formulation by Reciprocity and a Variational Principle," J. Lightwave Tech., vol.LT-5, pp.5-15, 1987.

[Chua87b] S.-L. Chuang, "A Coupled-Mode Theory for Multiwaveguide Systems Satisfying the Reciprocity Theorem and Power Conservation," J. Lightwave Tech., vol.LT-5, pp.174-183, 1987.

[Conn87] J. M. Connors and A. Mahapatra, "High Finesse Ring Resonators Made by Silver Ion Exchange in Glass," J. Lightwave Tech., vol.LT-5, pp.1686-1689, 1987.

[Coop80] A. R. Cooper and M. Abou-el-Leil, "Index Variation from Field-Assisted Ion Exchange," Appl. Opt., vol.19, pp.1087-1091, 1980.

[Cran75] J. Crank, The Mathematics of Diffusion, 2nd ed., Clarendon Press, Oxford, England, 1975.

[Cuch61] T. I. Cucher, "The Problem of Diffusion in an Evaporating Solid Medium," Sov. Phys. Solid State, vol.3, pp.401-404, 1961.

[Cull84] T. J. Cullen and C. D. W. Wilkinson, "Radiation Losses from Single-Mode Optical Y Junctions Formed by Silver-Ion Exchange in Glass," Optics Lett., vol.10, pp.134-136, 1984.

[Cull86] T. J. Cullen, C. N. Ironside, C. T. Seaton, and G. I. Stegeman, "Semiconductor-Doped Glass Ion-Exchanged Waveguides," Appl. Phys. Lett., vol.49, pp.1403-1405, 1986.

[Dani84] P. Danielsen, "Two-Dimensional Propagating Beam Analysis of an Electrooptic Waveguide Modulator," IEEE J. Quan. Electron., vol.QE-20, pp.1093-1097, 1984.

[Day76] D. E. Day, "Mixed Alkali Glasses - Their Properties and Uses," J. Non-Cryst. Solids, vol.21, pp.343-372, 1976.

[Deim90] P. P. Deimel, B. B. Heimhofer, G. Krötz, H. J. Lilienhof, J. Wind, G. Müller, and E. Voges, "Amorphous SiGe:H Photodetectors on Glass Optical Waveguides," IEEE Photo. Tech. Lett., vol.2, pp.499-501, 1990.

[Dore64] R. H. Doremus, "Exchange and Diffusion of Ions in Glass," J. Phys. Chem., vol.68, pp.2212-2218, 1964.

[Dore69] R. H. Doremus, "Ion-Exchange in Glass," Chap.2, J. A. Marinsky (Ed.), Ion-Exchange - A Series of Advances, Vol.2, Marcel Dekker, Inc., New York, 1969.

[Eguc83] R. G. Eguchi, E. A. Maunders, and I. K. Naik, "Fabrication of Low-Loss Waveguides in BK-7 by Ion Exchange," SPIE, vol.408, pp.21-26, 1983.

[Faik83] A. Faik, L. Allen, C. Eicher, A. Gagola, and P. D. Townsend, "Dispersion and Luminescence Measurements of Optical Waveguides," J. Appl. Phys., vol.54, pp.2597-2601, 1983.

[Fede89] M. Federighi, "Beam-Propagation Model of Distributed-Feedback Lasers: Below-Threshold Behavior," J. Appl. Phys., vol.65, pp.2620-2626, 1989.

[Feit78] M. D. Feit and J. A. Fleck, Jr., "Light Propagation in Graded-Index Optical Fibers," Appl. Opt., vol.17, pp.3990-3998, 1978.

[Feit79] M. D. Feit and J. A. Fleck, Jr., "Calculation of Dispersion in Graded-Index Multimode Fibers by a Propagating-Beam Method," Appl. Opt., vol.18, pp.2843-2851, 1979.

[Feit80] M. D. Feit and J. A. Fleck, Jr., "Computation of Mode Properties in Optical Fiber Waveguides by a Propagating Beam Method," Appl. Opt., vol.19, pp.1154-1164, 1980.

[Feit83] M. D. Feit, J. A. Fleck, Jr., and L. McCaughan, "Comparison of Calculated and Measured Performance of Diffused Channel-Waveguide Couplers," J. Opt. Soc. Am., vol.73, pp.1296-1304, 1983.

[Find83] T. Findakly, B. Chen, and D. Booher, "Single-Mode Integrated-Optical Polarizers in $LiNbO_3$ and Glass Waveguides," Optics Lett., vol.8, pp.641-643, 1983.

[Find85] T. Findakly, "Glass Waveguides by Ion Exchange: A Review," Optical Eng., vol.24, pp.244-250, 1985.

[Fine88] G. J. Fine and P. S. Danielson, "Chemical Strengthening by the Ion Exchange of Lithium for Sodium," Phys. Chem. Glasses, vol.29, pp.134-140, 1988.

[Flec76] J. A. Fleck, Jr., J. R. Morris, and M. D. Feit, "Time-Dependent Propagation of High Energy Laser Beams through the Atmosphere," Appl. Phys., vol.10, pp.129-160, 1976.

[Forr86] K. Forrest, S. J. Pagano, and W. Viehmann, "Channel Waveguides in Glass via Silver-Sodium Field-Assisted Ion Exchange," J. Lightwave Tech., vol.LT-4, pp.140-150, 1986.

[Gall76] J. G. Gallagher and R. M. DeLaRue, "Single-Mode Stripe Optical Waveguides Formed by Silver Ion Exchange," Electron. Lett., vol.12, pp.397-398, 1976.

[Garf68] H. M. Garfinkel, "Ion-Exchange Equilibria between Glass and Molten Salts," J. Phys. Chem., vol.72, pp.4175-4181, 1968.

[Gede75a] A. Gedeon, "Formation and Characteristics of Graded-Index Optical Waveguides Buried in Glass," Appl. Phys., vol.6, pp.223-228, 1975.

[Gede75b] A. Gedeon and B. Carnstam, "Radiation Loss in Bends of Diffused Optical Stripe Waveguides," Opt. & Quantum. Electron., vol.7, pp.456-458, 1975.

[Gevo90] S. S. Gevorgyan, "Single-Step Buried Waveguides in Glass by Field-Assisted Copper Ion-Exchange," Electron. Lett., vol.26, pp.38-39, 1990.

[Gial73] T. G. Giallorenzi, E. J. West, R. Kirk, R. Ginther, and R. A. Andrews, "Optical Waveguides Formed by Thermal Migration of Ions in Glass," Appl. Opt., vol.12, pp.1240-1245, 1973.

[Glan90] B. Glance and O. Scaramucci, "Dense FDM Coherent Optical Network with Random Access Provided by Digitally Tuned Transmitters and Receivers," OFC conf., San Francisco, CA, 1990, paper TuE1.

[Gord66] J. P. Gordon, "Optics of General Guiding Media," Bell Syst. Tech. J., vol.45, pp.321-332, 1966.

[Gort86a] J. E. Gortych and D. G. Hall, "Fabrication of Planar Optical Waveguides by K^+ Ion Exchange in BK7 Glass," Optics Lett., vol.11, pp.100-102, 1986.

[Gort86b] J. E. Gortych and D. G. Hall, "Fabrication of planar optical waveguides by K^+-ion exchange in BK7 and pyrex glass," IEEE J. Quantum Electron., vol.QE-22, pp.892-895, 1986.

[Goto90] N. Goto and G. L. Yip, "Y-Branch Wavelength Multi/Demultiplexer for λ = 1.30 and 1.55 μm," Electron. Lett., vol.26, pp.102-103, 1990.

[Gunt88] C. Günther and D. Jestel, "Buried Waveguides Produced by a One-Step Field-Assisted Ag^+ Ion-Exchange in Glass," SPIE, vol.993, Integrated Optical Circuit Engineering VI, pp.2-6, 1988.

[Haus87a] H. A. Haus, W. P. Huang, S. Kawakami, and N. A. Whitaker, "Coupled-Mode Theory of Optical Waveguides," J. Lightwave Tech., vol.LT-5, pp.16-23, 1987.

[Haus87b] H. A. Haus, W.-P. Huang, and N. M. Whitaker, "Optical Waveguide Dispersion Characteristics from the Scalar Wave Equation," J. Lightwave Tech., vol.LT-5, pp.1748-1754, 1987.

[Haus89] H. A. Haus, W. P. Huang, and A. W. Snyder, "Coupled-Mode Formulations," Optics Lett., vol.14, pp.1222-1224, 1989.

[Helf58] F. Helfferich and M. S. Plesset, "Ion Exchange Kinetics. A Nonlinear Diffusion Problem," J. Chem. Phys., vol.28, pp.418-424, 1958.

[Helf62] F. Helfferich, "Ion-Exchange Kinetics. III. Experimental Test of the Theory of Particle-Diffusion Controlled Ion Exchange," J. Phys. Chem., vol.66, pp.39-44, 1962.

[Hock77] G. B. Hocker and W. K. Burns, "Mode Dispersion in Diffused Channel Waveguides by the Effective Index Method," Appl. Opt., vol.16, pp.113-118, 1977.

[Hond84] K. Honda, E. M. Garmire, and K. E. Wilson, "Characteristics of an Integrated Optics Ring Resonator Fabricated in Glass," J. Lightwave Tech., vol.LT-2, pp.714-718, 1984.

[Honk87a] S. Honkanen, A. Tervonen, H. von Bagh, and M. Leppihalme, "Ion Exchange Process for Fabrication of Waveguide Couplers for Fiber Optic Sensor Applications," J. Appl. Phys., vol.61, pp.52-56, 1987.

[Honk87b] S. Honkanen, A. Tervonen, and M. McCourt, "Control of Birefringence in Ion-Exchanged Glass Waveguides," Appl. Opt., vol.26, pp.4710-4711, 1987.

[Honk88] S. Honkanen and A. Tervonen, "Experimental Analysis of Ag^+-Na^+ Exchange in Glass with Ag Film Ion Sources for Planar Optical Waveguide Fabrication," J. Appl. Phys., vol.63, pp.634-639, 1988.

[Houd86] S. N. Houde-Walter and D. T. Moore, "Delta-n Control in GRIN Glass by Additives in AgCl Diffusion Baths," Appl. Opt., vol.25, pp.3373-3378, 1986.

[Hugg40] M. L. Huggins, "The Refractive Index of Silicate Glasses as a Function of Composition," J. Opt. Soc. Am., vol.30, pp.495-504, 1940.

[Hugg43] M. L. Huggins and K.-H. Sun, "Calculation of Density and Optical Constants of a Glass from its Composition in Weight Percentage," J. Am. Ceram. Soc., vol.1, pp.4-11, 1943.

[Huss89] C. P. Hussell, H. C. Cheng, R. Srivastava, R. V. Ramaswamy, and J. L. Jackel, "Single Mode Cross-Coupler 3 dB Power Dividers by Ion-Exchange," MOC/GRIN Conf., Tokyo, Japan, 1989, paper D3.

[Huss90] C. P. Hussell, R. V. Ramaswamy, and R. Srivastava, "Wavelength and Polarization insensitive 3 dB Cross-Coupler Power Dividers by Ion-Exchange in Glass," Appl. Phys. Lett., vol.56, pp.2381-2383, 1990.

[Imai83] M. Imai, N. Haneda, and Y. Ohtsuka, "Losses in Optical Waveguides Formed by Silver-Sodium Ion Exchange," J. Lightwave Tech., vol.LT-1, pp.611-615, 1983.

[Imot87] K. Imoto, H. Sano, and M. Miyazaki, "Guided-Wave Multi/Demultiplexers with High Stopband Rejection," Appl. Opt., vol.26, pp.4214-4219, 1987.

[Isar69] J. O. Isard, "The Mixed Alkali Effect in Glass," J. Non-Cryst. Solids, vol.1, pp.235-261, 1969.

[Izaw72] T. Izawa and H. Nakagome, "Optical Waveguide Formed by Electrically Induced Migration of Ions in Glass Plates," Appl. Phys. Lett., vol.21, pp.584-586, 1972.

[Jain83] H. Jain, N. L. Peterson, and H. L. Downing, "Tracer Diffusion and Electrical Conductivity in Sodium-Cesium Silicate Glasses," J. Non-Cryst. Solids, vol.55, pp.283-300, 1983.

[Jest90] D. Jestel, A. Baus, and E. Voges, "Integrated-Optic Interferometric Microdisplacement Sensor in Glass with Thermo-optic Phase Modulation," Electron. Lett., vol.26, pp.1144-1145, 1990.

[Kacz88] P. Kaczmarski and P. E. Lagasse, "Bidirectional Beam Propagation Method," Electron Lett., vol.24, pp.675-676, 1988.

[Kane85] T. Kaneko, "Theoretical Concentration Profile from a Two-Step Field-Assisted Diffusion Process in Glass," J. Phys. D, vol.18, pp.1597-1607, 1985.

[Kane86] T. Kaneko, "Theoretical Interpretation of a Two-Step Field-Assisted Diffusion Process in Glass," J. Mater. Sci. Lett., vol.5, pp.928-930, 1986.

[Kaps82] C. Kaps and G. Völksch, "On the Interdiffusion of Ag^+ and Na^+ Ions in the Glass $Na_2O{\bullet}2SiO_2$ around the Glass Transition Temperature," J. Non-Cryst. Solids, vol.53, pp.143-153, 1982.

[Kaps84] C. Kaps, "On the Self-Diffusion of Na^+ Ions in the Glass $Na_2O{\bullet}2SiO_2$ around the Glass Transition Temperature," J. Non-Cryst. Solids, vol.65, pp.189-192, 1984.

[Kara79] G. O. Karapetyan, V. Y. Livshits, and G. T. Petrovskii, "Physicochemical Basis of the Formation of a Refractive-Index Gradient in Optical Media Using Ion-Exchange Methods," Sov. J. Glass Phys. & Chem., vol.5, pp.1-21, 1979, trans. from Fiz. Khim. Stekla (USSR), vol.5, pp.3-25, 1979.

[Karr62] G. Karreman and G. Eisenman, "Electrical Potentials and Ionic Fluxes in Ion Exchangers: I. 'n-Type' Non-Ideal Systems with Zero Current," Bull. Math. Biophys., vol.24, pp.413-427, 1962.

[Kirk61] J. G. Kirkwood and J. Oppenheim, Chemical Thermodynamics, McGraw Hill, New York, 1961.

[Koai86] K. T. Koai and P. L. Liu, "Digital and Quasi-Linear Electrooptic Modulators Synthesized from Directional Couplers," IEEE J. Quantum Electron., vol.QE-22, pp.2191-2194, 1986.

[Koge74] H. Kogelnik and V. Ramaswamy, "Scaling Rules for Thin-Film Optical Waveguides," Appl. Opt., vol.13, pp.1857-1862, 1974.

[Koge76] H. Kogelnik and R. V. Schmidt, "Switched Directional Couplers with Alternating $\Delta\beta$," IEEE J. Quantum Electron., vol.QE-12, pp.396-401, 1976.

[Koge88] H. Kogelnik, "Theory of Optical Waveguides," Chap.2, Guided-Wave Optoelectronics, T. Tamir (ed.), Springer-Verlag, Berlin, 1988.

[Kosh85a] M. Koshiba, K. Hayata, and M. Suzuki, "Improved Finite-Element Formulation in Terms of the Magnetic Field Vector for Dielectric Waveguides," IEEE Trans. Microwave Theory Tech., vol.MTT-33, pp.227-233, 1985.

[Kosh85b] M. Koshiba, H. Kumagami, and M. Suzuki, "Finite-Element Solution of Planar Arbitrarily Anistropic Diffused Optical Waveguides," J. Lightwave Tech., vol.LT-3, pp.773-778, 1985.

[Kuma83] A. Kumar, K. Thyagarajan, and A. K. Ghatak, "Analysis of Rectangular-Core Dielectric Waveguides: An Accurate Perturbation Approach," Optics Lett., vol.8, pp.63-65, 1983.

[Lagu84a] R. K. Lagu, S. I. Najafi, and V. Ramaswamy, "*In situ* Measurement of Ionic Concentration during Fabrication of Ion-Exchanged Waveguides," Appl. Opt., vol.23, pp.3925-3930, 1984.

[Lagu84b] R. K. Lagu and V. Ramaswamy, "Fabrication of Single Mode Glass Waveguides by Electrolytic Release of Silver Ions," Appl. Phys. Lett., vol.45, pp.117-118, 1984.

[Lagu86a] R. K. Lagu and R. V. Ramaswamy, "Silver Ion-Exchanged, Buried, Glass Optical Waveguides with Symmetric Index Profile," Appl. Phys. Lett., vol.48, pp.19-20, 1986.

[Lagu86b] R. K. Lagu and R. V. Ramaswamy, "A Variation Finite-Difference Method for Analyzing Channel Waveguides with Arbitrary Index Profiles," IEEE Quan. Electron., vol.QE-22, pp.968-976, 1986.

[Lait57] R. W. Laity, "Fused Salt Concentration Cells with Temperature. Activity Coefficients in the System Silver Nitrate-Sodium Nitrate," J. Am. Chem. Soc., vol.79, pp.1849-1851, 1957.

[Land85] K. A. Landa, G. T. Petrovskii, A. V. Mishin, and S. A. Guminnyi, "Planar Waveguides Obtained in Optical Glasses by Ion-Exchange Diffusion from $TlNO_3$ and KNO_3 Melts," Sov. J. Glass Phys. & Chem., vol.11, pp.340-344, 1985, trans. from Fiz. Khim. Stekla (USSR), vol.11, pp.542-546, 1985.

[Lee86] D. L. Lee, Electromagnetic Principles of Integrated Optics, Chap.8, John Wiley & Sons, New York, 1986.

[Lili82] H.-J. Lilienhof, E. Voges, D. Ritter, and B. Pantschew, "Field-Induced Index Profiles of Multimode Ion-Exchanged Strip Waveguides," IEEE J. Quan. Electron., vol.QE-18, pp.1877-1883, 1982.

[Maba81] N. Mabaya, P. E. Lagasse, and P. Vandenbulcke, "Finite Element Analysis of Optical Waveguides," IEEE Trans. Microwave Theory Tech., vol.MTT-29, pp.600-605, 1981.

[Maha88a] A. Mahapatra and J. M. Connors, "Thermal Tapering of Ion-Exchanged Channel Guides in Glass," Optics Lett., vol.13, pp.169-171, 1988.

[Maha88b] A. Mahapatra and J. M. Connors, "Star Couplers Fabricated in Ion Exchanged Glass Substrates," SPIE, vol.993, pp.169-172, 1988.

[Malk61] R. Sh. Malkovich, "Methods for Calculating the Mobility of Impurity Ions in a Solid," Sov. Phys. Solid State, vol.2, pp.2479-2488, 1961.

[Mar86a] E. A. J. Marcatili, "Improved Coupled-Mode Equations for Dielectric Guides," IEEE J. Quantum Electron., vol.QE-22, pp.988-993, 1986.

[Mar86b] E. A. J. Marcatili, L. L. Buhl, and R. C. Alferness, "Experimental Verification of the Improved Coupled-Mode Equations," Appl. Phys. Lett., vol.49, pp.1692-1693, 1986.

[Marc70] D. Marcuse, "Radiation Losses of Tapered Dielectric Slab Waveguides," Bell Syst. Tech. J., vol.49, pp.273-290, 1970.

[Marc74] D. Marcuse, Theory of Dielectric Optical Waveguides, Chap.3, Academic Press, New York, 1974.

[Marc79] D. Marcuse, D. Gloge, and E. A. J. Marcatili, "Guiding Properties of Fibers," Chap.3, Optical Fiber Telecommunication, S. E. Miller and A. G. Chynoweth (ed.), Academic Press, New York, 1979.

[Marc87] D. Marcuse, "Bandwidth of Forward and Backward Coupling Directional Couplers," J. Lightwave Tecnol., vol.LT-5, pp.1773-1777, 1987.

[Mats73] M. Matsuhara, "Analysis of TEM Modes in Dielectric Waveguides, by a Variational Method," J. Opt. Soc. Am., vol.63, pp.1514-1517, 1973.

[Mcco87] M. McCourt, R. Rimet, and C. Nissim, "Multiplexing Characteristics of K^+ and Ag^+ Ion-Exchanged Directional Couplers," Technical Digest of EFOC/LAN Conf., pp.111-114, Basel, Switzerland, 1987.

[Mcil89] P. W. A. McIlroy, M. S. Stern, and P. C. Kendall, "Fast and Accurate Method for Calculation of Polarised Modes in Semiconductor Rib Waveguides," Electron. Lett., vol.25, pp.1586-1587, 1989.

[Mcil90] P. W. A. McIlroy, M. S. Stern, and P. C. Kendall, "Spectral Index Method for Polarized Modes in Semiconductor Rib Waveguides," J. Lightwave Tech., vol.LT-8, pp.113-116, 1990.

[Mili89] A. Miliou, H. Zhenguang, H. C. Cheng, R. Srivastava, and R. V. Ramaswamy, "Fiber-Compatible K^+-Na^+ Ion-Exchanged Channel Waveguides: Fabrication and Characterization," IEEE J. Quan. Electron., vol.QE-25, pp.1889-1897, 1989.

[Mill54] S. E. Miller, "Coupled Wave Theory and Waveguide Applications," Bell Syst. Tech. J., vol.33, pp.661-719, 1954.

[Mill78] C. A. Millar and R. H. Hutchins, "Manufacturing Tolerances for Silver-Sodium Ion-Exchanged Planar Optical Waveguides," J. Phys. D, vol.11, pp.1567-1576, 1978.

[Mish86] P. K. Mishra and A. Sharma, "Analysis of Single Mode Inhomogeneous Planar Waveguides," J. Lightwave Tech., vol.LT-4, pp.204-211, 1986.

[Naja85] S. I. Najafi, R. V. Ramaswamy, and R. K. Lagu, "An Improved Method for Fabricating Ion-Exchanged Waveguides through Electrolytic Release of Silver Ions," J. Lightwave Tech., vol.LT-3, pp.763-766, 1985.

[Naja86] S. I. Najafi, P. G. Suchoski, Jr., and, R. V. Ramaswamy, "Silver Film-Diffused Glass Waveguides: Diffusion Process and Optical Properties," IEEE Quan. Electron., vol.QE-22, pp.2213-2218, 1986.

[Naja88a] S. I. Najafi, "Glass Directional Coupler Wavelength Filter," Appl. Opt., vol.27, pp.1386-1388, 1988.

[Naja88b] S. I. Najafi, "Optical Behavior of Potassium Ion-Exchanged Glass Waveguides," Appl. Opt., vol.27, pp.3728-3731, 1988.

[Nega89] T. Negami, H. Haga, and S. Yamamoto, "Guided-Wave Optical Wavelength Demultiplexer Using an Asymmetric Y Junction," Appl. Phys. Lett., vol.54, pp.1080-1082, 1989.

[Neum79] V. Neuman, O. Parriaux, and L. M. Walpita, "Double-Alkali Effect: Influence on Index Profile of Ion-Exchanged Waveguides," Electron. Lett., vol.15, pp.704-706, 1979.

[Neye85] A. Neyer, W. Mevenkamp, L. Thylen, and B. Lagerström, "A Beam Propagation Method Analysis of Active and Passive Waveguide Crossings," J. Lightwave Tech., vol.LT-3, pp.635-642, 1985.

[Nyma89] B. M. Nyman and P. R. Prucnal, "The Modified Beam Propagation Method," J. Lightwave Tech., vol.LT-7, pp.931-936, 1989.

[Ohta75] H. Ohta, "The Strengthening of Mixed Alkali Glass by Ion Exchange," Glass Tech., vol.16, pp.25-29, 1975.

[Okos85] T. Okoshi, Planar Circuits—For Microwaves and Lightwaves, Chap.10, Springer-Verlag, Berlin, 1985.

[Pant87] B. G. Pantchev, "One-Step Field-Assisted Ion Exchange for Fabrication of Buried Multimode Optical Strip Waveguides," Electron. Lett., vol.23, pp.188-190, 1987.

[Pitt81] C. W. Pitt, "Thin Film Optical Waveguides Fabricated by Ion-Assisted Techniques," Thin Solid Films, vol.86, pp.137-146, 1981.

[Ples58] M. S. Plesset, F. Helfferich, and J. N. Franklin, "Ion Exchange Kinetics. A Nonlinear Diffusion Problem. II. Particle Diffusion Controlled Exchange of Univalent and Bivalent Ions," J. Chem. Phys., vol.29, pp.1064-1069, 1958.

[Rama74] V. Ramaswamy, "Strip-Loaded Film Waveguide," Bell Syst. Tech. J., vol.53, pp.697-704, 1974.

[Rama83] V. Ramaswamy and R. K. Lagu, "Numerical Field Solution for an Arbitrary Asymmetrical Graded-Index Planar Waveguide," J. Lightwave Tech., vol.LT-1, pp.408-416, 1983.

[Rama86] R. V. Ramaswamy and S. I. Najafi, "Planar, Buried, Ion-Exchanged Glass Waveguides: Diffusion Characteristics," IEEE Quan. Electron., vol.QE-22, pp.883-891, 1986.

[Rama88a] R. V. Ramaswamy, H. C. Cheng, and R. Srivastava, "Process Optimization of Buried Ag^+-Na^+ Ion-Exchanged Waveguides: Theory and Experiment," Appl. Opt., vol.27, pp.1814-1819, 1988.

[Rama88b] R. V. Ramaswamy and R. Srivastava, "Ion-Exchanged Glass Waveguides: A Review," J. Lightwave Tech., vol.LT-6, pp.984-1002, 1988.

[Rama88c] R. V. Ramaswamy and R. Srivastava, "Recent Advances in Ion-Exchanged Optical Waveguides and Components," J. Mod. Opt., vol.35, pp.1049-1067, 1988.

[Rama88d] R. V. Ramaswamy, R. Srivastava, P. Chludzinski, and T. J. Anderson, "Influence of Ag^+-Na^+ Ion-Exchange Equilibrium on Waveguide Index Profiles," IEEE J. Quan. Electron., vol.QE-24, pp.780-786, 1988.

[Ross86] L. Ross, H.-J. Lilienhof, and H. W. Hölscher, "Buried Waveguides for Passive Integrated Optics by Cs^+-Ion-Exchange," SPIE, vol.651, pp.32-34, 1986.

[Ross89] L. Ross, "Integrated Optical Components in Substrate Glasses," Glastech. Ber., vol.62, pp.285-297, 1989.

[Sane78] A. Y. Sane and A. R. Cooper, "Anomalous Stress Profiles in Ion-Exchanged Glass," J. Am. Ceram. Soc., vol.61, pp.359-362, 1978.

[Sanf90] N. A. Sanford, K. J. Malone, and D. R. Larson, "Integrated-Optic Laser Fabricated by Field-Assisted Ion Exchange in Neodymium-Doped Soda-Lime-Silicate Glass," Optics Lett., vol.15, pp.366-368, 1990.

[Sava76] I. Savatinova, "Lightguiding in Ion-Exchanged Glasses," Appl. Phys., vol.11, pp.273-276, 1976.

[Schl90] N. E. Schlotter, J. L. Jackel, P. D. Townsend, and G. L. Baker, "Fabrication of Channel Waveguides in Polydiacetylenes: Composite Diffused Glass/Polymer Structures," Appl. Phys. Lett., vol.1, pp.13-15, 1990.

[Sriv87a] R. Srivastava, C. K. Kao, and R. V. Ramaswamy, "WKB Analysis of Planar Surface Waveguides with Truncated Index Profiles," J. Lightwave Tech., vol.LT-5, pp.1605-1608, 1987.

[Sriv87b] R. Srivastava, R. V. Ramaswamy, H. C. Cheng, and H. Zhenguang, "Fabrication and Characterization of Single-Mode Glass Waveguides," SPIE, Proc. vol.835, pp.288-295, 1987.

[Ster66] K. H. Stern, "Glass-Molten Salt Interactions," Chem. Rev., vol.66, pp.355-372, 1966.

[Ster88a] M. S. Stern, "Semivectorial Polarised Finite Difference Method for Optical Waveguides with Arbitrary Index Profiles," IEE Proc. vol.135, pt.J, pp.56-62, 1988.

[Ster88b] M. S. Stern, "Semivectorial Polarised H Field Solutions for Dielectric Waveguides with Arbitrary Index Profiles," IEE Proc., vol.135, pt.J, pp.333-338, 1988.

[Ster90] M. S. Stern, P. C. Kandall, and P. W. A. McIlroy, "Analysis of the Spectral Index Method for Vector Modes of Rib Waveguides," IEE Proc., vol.137, pt.J, pp.21-26, 1990.

[Stew77] G. Stewart, C. A. Millar, P. J. R. Laybourn, C. D. W. Wilkinson, and R. M. DeLaRue, "Planar Optical Waveguides Formed by Silver-Ion Migration in Glass," IEEE J. Quan. Electron., vol.QE-13, pp.192-200, 1977.

[Stew78] G. Stewart and P. J. R. Laybourn, "Fabrication of Ion-Exchanged Optical Waveguides from Dilute Silver Nitrate Melts," IEEE J. Quan. Electron., vol.QE-14, pp.930-934, 1978.

[Stre87a] W. Streifer, "Coupled Mode Theory," Electron. Lett., vol.23, pp.316-317, 1987.

[Stre87b] W. Streifer, M. Osinski, and A. Hardy, "Reformulation of the Coupled-Mode Theory of Multiwaveguide Systems," J. Lightwave Tech., vol.LT-5, pp.1-4, 1987.

[Such87] P. G. Suchoski, Jr. and R. V. Ramaswamy, "Constant-Width Variable Index Transition for Efficient Ti:$LiNbO_3$ Waveguide-Fiber Coupling," J. Lightwave Technol., vol.LT-5, pp.1246-1251, 1987.

[Suem77] Y. Suematsu and K. Kishino, "Coupling Coefficient in Strongly Coupled Dielectric Waveguides," Radio Sci., vol.12, pp.587-592, 1977.

[Suzu89] S. Suzuki, S. Sekine, K. Shuto, Y. Ueoka, and I. Nishi, "Small-Size Optical Multi/Demultiplexer Using High Δ Composite Glass Waveguide," IOOC Conf., Osaka, Japan, 1989, paper 19D1-5.

[Tami79] T. Tamir, "Beam and Waveguide Couplers," Chap.3, Integrated Optics, T. Tamir (ed.), Springer-Verlag, New York, 1979.

[Terv87] A. Tervonen, S. Honkanen, and M. Leppihalme, "Control of Ion-Exchange Waveguide Profiles with Ag Thin-Film Sources," J. Appl. Phys., vol.62, pp.759-763, 1987.

[Thyl86] L. Thylén, E. M. Wright, G. I. Stegeman, C. T. Seaton, and J. V. Moloney, "Beam-Propagation Method Analysis of a Nonlinear Directional Coupler," Optics Lett., vol.11, pp.739-742, 1986.

[Thyl88] L. Thylén, "Integrated Optics in $LiNbO_3$: Recent Developments in Devices for Telecommunications," J. Lightwave Technol., vol.LT-6, pp.847-861, 1988.

[Tien69] P. K. Tien, R. Ulrich, and R. J. Martin, "Modes of Propagating Light Waves in Thin Deposited Semiconductor Films," Appl. Phys. Lett., vol.14, pp.291-294, 1969.

[Tien70] P. K. Tien and R. Ulrich, "Theory of Prism-Film Coupler and Thin-Film Light Guides," J. Opt. Soc. Am., vol.60, pp.1325-1337, 1970.

[Tsut86] K. Tsutsumi, H. Hirai, and Y. Yuba, "Characteristics of Swelling of Sodium-Potassium Ion-Exchanged Glass Waveguides," Electron. Lett., vol.22, pp.1299-1300, 1986.

[Tsut88] K. Tsutsumi, H. Hirai, and Y. Yuba, "Relation between the Ordinary and Extraordinary Index Profiles of Ion-Exchanged Glass Waveguides," Optics Lett., vol.13, pp.416-418, 1988.

[Ulri70] R. Ulrich, "Theory of the Prism-Film Coupler by Plane-Wave Analysis," J. Opt. Soc. Am., vol.60, pp.1337-1350, 1970.

[Vanr81] J. Van Roey, J. van der Donk, and P. E. Lagasse, "Beam-Propagation Method: Analysis and Assessment," J. Opt. Soc. Am., vol.71, pp.803-810, 1981.

[Vass87] C. Vassallo, "Condensed Formula for Coupling Coefficients between Parallel Dielectric Waveguides," Electron. Lett., vol.23, pp.334-335, 1987.

[Veld88] K. Van de Velde, H. Thienpont, and R. Van Geen, "Extending the Effective Index Method for Arbitrarily Shaped Inhomogeneous Optical Waveguides," J. Lightwave Tech., vol.6, pp.1153-1159, 1988.

[Verb88] B. H. Verbeek, C. H. Henry, N. A. Olsson, K. J. Orlowsky, R. F. Kazarinov, and B. H. Johnson, "Integrated Four-Channel Mach-Zehnder Multi/Demultiplexer Fabricated with Phosphorous Doped SiO_2 Waveguides on Si," J. Lightwave Technol., vol.LT-6, pp.1011-1015, 1988.

[Vilj80] J. Viljanen and M. Leppihalme, "Fabrication of Optical Strip Waveguides with Nearly Circular Cross Section by Silver Ion Migration Technique," J. Appl. Phys., vol.51, pp.3563-3565, 1980.

[Volf88] M. B. Volf, Mathematical Approach to Glass, chap.15,23, Elsevier Science Publishing Co., Inc., New York, 1988, trans. from Czech.

[Walk83a] R. G. Walker and C. D. W. Wilkinson, "Integrated Optical Ring Resonators Made by Silver Ion-Exchange in Glass," Appl. Opt., vol.22, pp.1029-1035, 1983.

[Walk83b] R. G. Walker and C. D. W. Wilkinson, "Integrated Optical Waveguiding Structures Made by Silver Ion-Exchange in Glass. 2: Directional Coupler and Bends," Appl. Opt., vol.22, pp.1929-1936, 1983.

[Walk83c] R. G. Walker, C. D. W. Wilkinson, and J. A. H. Wilkinson, "Integrated Optical Waveguiding Structures Made by Silver Ion-Exchange in Glass. 1: The Propagation Characteristics of Strip Ion-Exchanged Waveguides; a Theoretical and Experimental Investigation," Appl. Opt., vol.22, pp.1923-1928, 1983.

[Walk85] R. G. Walker, "Simple and Accurate Loss Measurement Technique for Semiconductor Optical Waveguides," Electron. Lett., vol.21, pp.581-583, 1985; Erratum, Electron. Lett., vol.21, p.714, 1985.

[Whit76] J. M. White and P. F. Heidrich, "Optical Waveguide Refractive Index Profiles Determined from Measurement of Mode Indices: A Simple Analysis," Appl. Opt., vol.15, pp.151-155, 1976.

[Wilk78] C. D. W. Wilkinson and R. Walker, "The Diffusion Profile of Stripe Optical Waveguides Formed by Ion Exchange," Electron. Lett., vol.14, pp.599-600, 1978.

[Wils76] M. G. F. Wilson, C. W. Pitt, R. Manku, A. D. de Oliveira, and O. Parrioux, "Optical Power Division in a Multimode Waveguide Intersection," Electon. Lett., vol.12, pp.434-435, 1976.

[Won80] Y. H. Won, P. C. Jaussaud, and G. H. Chartier, "Three-Prism Loss Measurements of Optical Waveguides," Appl. Phys. Lett., vol.37, pp.269-271, 1980.

[Yabl86] E. Yablonovitch, T. Gmitter, J. P. Harbison, and R. Bhat, "Extreme Selectivity in the Lift-Off of Epitaxial GaAs Films," Appl. Phys. Lett., vol.51, pp.2222-2224, 1986.

[Yari73] A. Yariv, "Coupled-Mode Theory for Guided-Wave Optics," IEEE J. Quan. Electron., vol.QE-9, pp.919-933, 1973.

[Yeh79] C. Yeh, K. Ha, S. B. Dong, and W. P. Brown, "Single-Mode Optical Waveguides," Appl. Opt., vol.18, pp.1490-1504, 1979.

[Yevi82] D. Yevick and L. Thylén, "Analysis of Grating by the Beam-Propagation Method," J. Opt. Soc. Am., vol.72, pp.1084-1089, 1982.

[Yevi86] D. Yevick, "New Fast Fourier Transform and Finite-Element Approaches to the Calculation of Multiple-Stripe-Geometry Laser Modes," J. Appl. Phys., vol.59, pp.1769-1771, 1986.

[Yevi89a] D. Yevick and M. Glasner, "Analysis of Forward Wide-Angle Light Propagation in Semiconductor Rib Waveguides and Integrated-Optic Structures," Electron. Lett., vol.25, pp.1611-1613, 1989.

[Yevi89b] D. Yevick and B. Hermansson, "New Formulations of the Matrix Beam Propagation Method: Application to Rib Waveguides," IEEE J. Quan. Electron., vol.QE-25, pp.221-229, 1989.

[Yevi89c] D. Yevick, C. Rolland, and B. Hermansson, "Fresnel Equation Studies of Longitudinally Varying Semiconductor Rib Waveguides: Reference Wavevector Dependence," Electron. Lett., vol.25, pp.1254-1256, 1989.

[Yevi90a] D. Yevick and B. Hermansson, "Efficient Beam Propagation Techniques," IEEE J. Quan. Electron., vol.QE-26, pp.109-112, 1990.

[Yevi90b] D. Yevick, C. Rolland, W. Bradyszewski, and B. Hermansson, "Fresnel Studies of Reflected Beams," IEEE Photo. Tech. Lett., vol.2, pp.490-492, 1990.

[Yip84] G. L. Yip and J. Finak, "Directional-Coupler Power Divider by Two-Step K^+-Ion Exchange," Optics Lett., vol.9, pp.423-425, 1984.

[Yip85] G. L. Yip and J. Albert, "Characterization of Planar Optical Waveguides by K^+-Ion Exchange in Glass," Optics Lett., vol.10, pp.151-153, 1985.

[Yosh85] H. Yoshida and T. Kataoka, "Migration of Two Ions during Electrolysis of Glass Waveguide," J. Appl. Phys., vol.58, pp.1739-1743, 1985.

[Zhen88] H. Zhenguang, R. Srivastava, and R. V. Ramaswamy, "Single-Mode Buried Channel Waveguide by Single-Step Electromigration Technique Using Silver Film," Appl. Phys. Lett., vol.53, pp.1681-1683, 1988.

[Zhen89] H. Zhenguang, R. Srivastava, and R. V. Ramaswamy, "Low-Loss Small-Mode Passive Waveguides and Near-Adiabatic Tapers in BK7 Glass," J. Lightwave Tech., vol.LT-7, pp.1590-1595, 1989.

BIOGRAPHICAL SKETCH

Hsing Chien Cheng was born in Taiwan, the Republic of China, in 1960. He received the B.S. degree from the National Taiwan University, Taiwan, in 1982 and the M.E. degree from the University of Florida, Gainesville, in 1986, both in the Department of Electrical Engineering.

Between 1982 and 1984 he taught in the Chinese Naval Engineering School during the military service. In December 1985, he joined the Photonics Research Laboratory at the University of Florida, Gainesville, working on the characterization and analysis of guided-wave devices in glass, fabricated by ion-exchange technique and the systematic modeling of these devices. He is a member of the Optical Society of America.

I certify that I have read this study and that in my opinion it conforms to acceptable standards of scholarly presentation and is fully adequate, in scope and quality, as a dissertation for the degree of Doctor of Philosophy.

Ramu V. Ramaswamy, Chairman
Professor of Electrical Engineering

I certify that I have read this study and that in my opinion it conforms to acceptable standards of scholarly presentation and is fully adequate, in scope and quality, as a dissertation for the degree of Doctor of Philosophy.

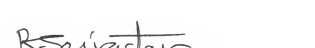

Ramakant Srivastava, Cochairman
Professor of Electrical Engineering

I certify that I have read this study and that in my opinion it conforms to acceptable standards of scholarly presentation and is fully adequate, in scope and quality, as a dissertation for the degree of Doctor of Philosophy.

Peter Zory
Professor of Electrical Engineering

I certify that I have read this study and that in my opinion it conforms to acceptable standards of scholarly presentation and is fully adequate, in scope and quality, as a dissertation for the degree of Doctor of Philosophy.

Utpal Das
Assistant Professor of Electrical Engineering

I certify that I have read this study and that in my opinion it conforms to acceptable standards of scholarly presentation and is fully adequate, in scope and quality, as a dissertation for the degree of Doctor of Philosophy.

Chen-Chi Hsu

Chen-Chi Hsu
Professor of Aerospace Engineering,
Mechanics, and Engineering Science

This dissertation was submitted to the Graduate Faculty of the College of Engineering and to the Graduate School and was accepted as partial fulfillment of the requirements for the degree of Doctor of Philosophy.

May 1991

Hubert T. Bevis

for Winfred M. Phillips
Dean, College of Engineering

Madelyn M. Lockhart
Dean, Graduate School